Spring 2004

Mixing enhancement by dual speed rotating stirrer

Arnaud Goullet
New Jersey Institute of Technology

ABSTRACT

MIXING ENHANCEMENT BY DUAL SPEED ROTATING STIRRER

by
Arnaud Goullet

Stirring is a well-known means of fluid mixing due to the emergence of complex patterns in the flow, even at low Reynolds numbers. In this work, we consider a stirrer rotating along a circular trajectory at constant speed. The fluid flow, considered incompressible, inviscid and two dimensional (in a circular container), is modeled by a point vortex model consisting of a vortex rotating in a circular container at constant angular speed. The mixing problem is addressed by considering the Hamiltonian form of the advection equations formulated in a frame of reference moving with the vortex. The dynamics of passive fluid particles is considered using dynamical systems theory. The bifurcation diagram reveals the presence of degenerate fixed points and homoclinic/heteroclinic orbits, whose nature varies for different parameter values. By considering an initially concentrated set of marker particles and using the various structures of the phase space in the bifurcation diagram, we produce a complex dynamics which, in turn, can generate efficient mixing. The latter is studied using both numerical simulations and physical experiments. A perturbation study for one particular structure for the phase space shows the presence of a transverse homoclinic orbit as well as resonances, or a set of closed trajectories.

MIXING ENHANCEMENT BY DUAL SPEED ROTATING STIRRER

by
Arnaud Goullet

A Dissertation
Submitted to the Faculty of
New Jersey Institute of Technology and
Rutgers, The State University of New Jersey – Newark
in Partial Fulfillment of the Requirements for the Degree of
Doctor of Philosophy in Mathematical Sciences

Department of Mathematical Sciences, NJIT
Department of Mathematics and Computer Science, Rutgers-Newark

May 2004

APPROVAL PAGE

MIXING ENHANCEMENT BY DUAL SPEED ROTATING STIRRER

Arnaud Goullet

Dr. Nadine N. Aubry, Dissertation Advisor — Date
Distinguished Professor and Chair of the Mechanical Engineering Department,
NJIT, Newark NJ

Dr. Denis Blackmore, Committee Member — Date
Professor of Mathematical Sciences, NJIT, Newark NJ

Dr. Lou Kondic, Committee Member — Date
Associate Professor of Mathematics, NJIT, Newark NJ

Dr. Demetrius Papageorgiou, Committee Member — Date
Professor of Mathematical Sciences, NJIT, Newark NJ

Dr. Michael Siegel, Committee Member — Date
Associate Professor of Mathematical Sciences, NJIT, Newark NJ member

BIOGRAPHICAL SKETCH

Author: Arnaud Goullet

Degree: Doctor of Philosophy

Date: May 2004

Undergraduate and Graduate Education:

- Doctor of Philosophy in Applied Mathematics,
  New Jersey Institute of Technology and Rutgers University , Newark, NJ, 2004
- Post-Graduate diploma in Theoretical Physics,
  Centre de Physique Théorique, CNRS , Marseille, France, 2000
- Bachelor of Science and Master in Physics,
  Université GrandMont, Tours, France, 1998-1999

Major: Applied Mathematics

Presentations and Publications:

"Mixing enhancement by dual speed rotating stirrer" presented at the 14th U.S. National Congress of Theoretical and Applied Mechanics at Blacksburg (Virginia) June 2002.

"Mixing enhancement by dual speed rotating stirrer" presented at the APS Division of Fluid Dynamics 55th Annual Meeting at Dallas (Texas) November 2002.

"Chaotic Mixing with a single stirrer" presented at the APS Division of Fluid Dynamics 56th Annual Meeting at East Rutherford (New Jersey) November 2003.

"Microfluidic Mixing Using Time Pulsing" AIMS' Fifth International Conference on Dynamical Systems and Differential Equations. Wednesday June 16 2004-Saturday June 19 2004. Department of Mathematics and Statitics California State Polytechnic University Pomona. (On behalf of Dr. Nadine Aubry, New Jersey Institute of Technology).

To my parents

and sisters Valérie and Maryline.

ACKNOWLEDGMENT

I would like to thank my advisor, Dr. Nadine Aubry, for her support during the past years. It was a great and valuable experience for me to be under her supervision. From the beginning of my stay at NJIT, she helped me more than I could have asked for.

I would like to thank my committee members, Professors D. Blackmore, L. Kondic, D. Papageorgiou and M. Siegel whose very useful comments and suggestions led to significant improvements of my Ph.D. dissertation.

I would like to extend my gratitude to Dr. Ahmed Ould El Moctar, Mr. John Batton and Mr. George barnes without whom the experiments would not have been possible.

I would like to thank Drs. Ricardo Lima and Michel Vittot from the Centre de Physique Theorique, Luminy, Marseille, France. I had my first classes in Dynamical Systems Theory from them while I was studying for my Marster's degree in France. They raised my curiosity and interests in Dynamical Systems Theory and showed me how interesting this field of research can be.

I would also like to thank my fellow graduate students, more specifically, Ahmed, Christina, Jyoti, Lin, Nick, Eliana, and Evros for being such good friends.

Finally, I would like to thank my parents and my sisters, Valérie and Maryline, for their support. My parents always trusted me and most of all they always gave me the freedom of choice in everything.

TABLE OF CONTENTS

TABLE OF CONTENTS
(Continued)

Chapter **Page**

TABLE OF CONTENTS
(Continued)

Chapter **Page**

LIST OF FIGURES

LIST OF FIGURES
(Continued)

Figure **Page**

LIST OF FIGURES
(Continued)

Figure **Page**

CHAPTER 1

INTRODUCTION

The problem of fluid mixing is almost an every day situation, where the most trivial example is the homogeneization of sugar in a cup of coffee.
However even in this simple situation, the turbulence created by the spoon, or stirrer, facilitates the mixing, and the flow is intrinsically complex with swirls and eddies of different sizes. The issue of fluid mixing becomes more challenging when turbulence is absent, or quasi-absent. Such a situation occurs for a fluid with high viscosity, or for small scale problems where the Reynolds number is small. In this case, natural molecular diffusion eventually accomplishes mixing. However, even at micro-scale, mixing by diffusion is by far too slow for industrial applications. For example, at room temperature, the coefficient of diffusion in water is about $10^{-11}m^2/s$, and the time constant for diffusion along a length of $100\mu m$ is $10^3 s \sim 16min.$

Before considering a problem of mixing in a laminar flow, referred to as laminar mixing, there is a need to define what we mean by mixing. Even though the question looks simple, the literature is unfortunately not uniform. Back in the middle of the 20^{th} century, the distinction of two different mechanisms "stirring" and "mixing" is pointed out, involving two different physical processes [13].

Considering a small volume of fluid, or initially localized blob of fluid, "stirring" refers to the mechanical process, or macro-scale dynamics of the flow, which will spread the blob of fluid more uniformly within a container. This spreading is achieved by stretching and deforming the blob. On the other hand, mixing is a small-scale process, based on diffusion across intermaterial surfaces. Stirring facilitates or enhances mixing by "producing" more intermaterial area. However, in some areas of research, e.g. chemical engineering, the word "mixing" is sometimes used without any consideration

of the diffusion phenomenon. There is also a mathematical definition of mixing in dynamical systems theory [26].

In this work, we will use the words "stirring" and "mixing", without any distinction, to mean the spreading of a blob of fluid within some given domain. In our work, this spreading will lead to a more uniform distribution of an initially localized blob and it will be facilitated by an underlying chaotic laminar flow. In particular, We will say that the mixing is "good" if an initially localized blob of dye will spread "everywhere" within the container. However, we notice that the presence of a chaotic flow will not necessarily imply that the spreading will take place everywhere or even in a uniform manner, in contrast with the mathematical definition where mixing implies ergodicity [15],[26].

Experimentally, studies of mixing have been performed using visualization techniques which have allowed one to follow the evolution of a blob of fluorescent dye. The different patterns of the flow are then visible, showing in certain cases very complex dynamics, including the multiple eddy structure of turbulence and the folding/stretching of materials lines typical of chaotic advection in laminar flows [46],[31].

Figure 1.1 Evolution of a Blob of Dye with a Time dependent Laminar Flow [46].

From a theoretical point of view, it has been shown that the Hamiltonian formalism applies to point vortex flows and that chaotic material lines which fold and stretch can be particularly efficient at enhancing mixing. This approach through which a set of ordinary differential equations are solved uses dynamical systems theory to study the structure of the flow.

In this context, it is well known that a one degree of freedom system is incapable of exhibiting chaotic behavior. However, the introduction of time dependency into the Hamiltonian, or system, can lead to a complex dynamics.

A simple two-dimensional model of stirring [1] consists of a point vortex, which stirs a fluid inside a circular container. This model is based on a vortex jumping back and forth between two fixed positions. Not only this system has been shown numerically to exhibit chaotic behavior, but also an explicit construction of a Smale Horseshoe [15], [38], [47] has actually been possible [36]. The term "chaotic advection" then started to be used to characterize the chaotic behavior of material lines in such flows, while the flow itself remains simple and laminar. Experimental, as well as analytical and numerical studies, have been performed on other related problems [16], [36].

For some time, it was thought that the presence of either vorticity or saddle connection (with non-zero circulation) was responsible for the generation of chaotic advection. However, an example based on a pulsed source-sink system with zero circulation everywhere was shown to exhibit chaotic advection as well [20].

Previous studies have revealed the importance of the kinematics of the flow itself for inducing good mixing. Whether the flow is a Stokes flow [3],[12], [37] or a potential flow [1],[21], the key ingredient leading to a chaotic advected particle path is the complexity of the material lines in space and time [30], and not the force balance in the momentum equation [2].

Mixers can be classified in two groups. The first group consists of passive mixers which do not require any external source of energy. For instance, the flow through a channel with some special geometry, like a 3D-serpentine [27] can facilitate mixing. Likewise, straight channels with ribs have also shown some enhancement [41]. In contrast, mixers in the second group require the injection of

an external source of energy. For example, it was shown that a magnetic field used to create vortices act like a stirrer in the fluid [16]. This can be done for a conducting fluid or by adding magnetic particles or beads to the fluid [43]. Our work belongs to the second category. It requires the generation and control of vortices to stir the fluid.

Applications of enhanced mixing via chaotic advection are numerous. Here, We restrict ourselves to the description of two examples only. The first one consists of the generation of manufactured layer composites in material processing [50] through chaotic advection whereby the layers are induced by chaotic (stretching/folding) material lines. Composite materials with thousands of layers have been produced successfully, with a layer thickness as small as 200 nm. The second example is in the area of biology, where it is proposed that the feeding of cells in a cavity can be achieved with a pulsating flow capable of inducing a chaotic dynamics from the breaking of a separatrix [18, 17] (see Figure (1.2)). A fluid with the appropriate nutrients flows above the cavity, acting as a perfusion.

One of the latest developments is a topological approach to determine if the stirring protocol itself implies chaos or mixing without any consideration of the flow itself [14]. Through mapping theory, more precisely a homotopy argument, a criterion for chaos is derived for a circular tank stirred with three stirrers under certain conditions.

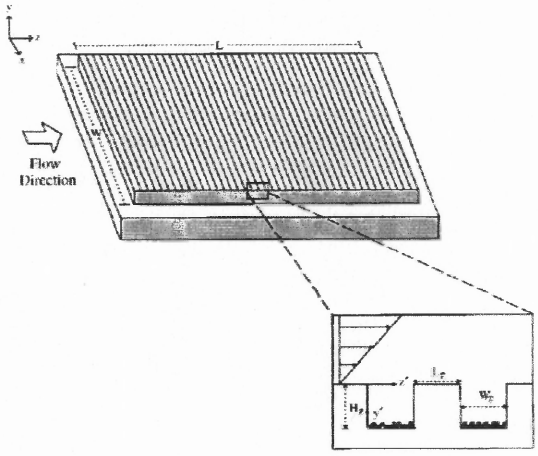

Figure 1.2 feeding of biological cell using chaotic advection.

In this work, we consider a model for stirring the fluid inside a circular container with one vortex only. In the first part of this study, we consider a vortex rotating around the container at a constant angular speed. After a simplification of the Hamiltonian itself in this case, we study the dynamics in phase space and derive the bifurcation diagram. While the dynamics thus generated is simple in nature, we will use this study to derive an alternative scenario capable of creating a dynamics sufficiently complicated to induce chaos. The latter will be shown numerically through the stretching and folding of material lines, but also by constructing a Smale horseshoe in the frame of reference of the vortex. An important characteristic of the proposed protocol is the possibility of mixing not only in the interior of the domain but also in the vicinity of the boundary due to the presence of a heteroclinic orbit there.

In order to explore the validity and relevance of our theoretical results, an experiment will be set up at the macro scale. A comparison between experimental flow visualizations and theoretical predictions will be performed.

Finally, we will add a time perturbation to our system and integrate the perturbed system by using a symplectic scheme.

CHAPTER 2

DESCRIPTION OF THE PROBLEM

2.1 Hamiltonian Formalism

The description of the spreading of a species in a fluid is given by the advection-diffusion equation. A scalar field ϕ, which can be the concentration of the advected quantity satisfies

$$\frac{\partial \phi}{\partial t} + \mathbf{V}.\nabla\phi = D\triangle\phi. \tag{2.1}$$

The equation (2.1) uses the Eulerian representation [6] and the advecting velocity field $\mathbf{V}(\mathbf{x}, t)$ is prescribed. For a small diffusivity constant D or large Péclet number, $Pe = \frac{VL}{D}$ where V and L are velocity and length of the system considered, the advection dominates the dynamics of the flow.

An alternative way to look at the spreading of blob of fluid is the Lagrangian representation of the fluid [23]. We denote by $\mathbf{V}(x, y, z) = (u(x, y, z), v(x, y, z), w(x, y, z))$ and $\mathbf{X}(t) = (x(t), y(t), z(t))$ the velocity and the position respectively of a passive fluid particle. The advection equation becomes

$$\frac{d\mathbf{X}}{dt} = \mathbf{V}_{fluid}. \tag{2.2}$$

A particle is said to be advected, or undergo "passive advection", if it is passive with respect to the flow, i.e. of negligible mass and with no interaction with the fluid (inert), and the particle "adjusts" its velocity to the velocity of the fluid instantaneously, i.e. $\mathbf{V}_{fluid} = \mathbf{V}_{particle}$.

If we know the velocity field, then the study of the fluid can be performed by solving the set of ordinary differential equations given by (2.2), which can exhibit chaotic behavior, or Lagrangian chaos.

In a two-dimensional flow, the assumption of incompressibility, i.e $\nabla.\mathbf{V} = 0$,

allows us to introduce the streamfunction $\Psi(x, y)$ such that

$$\dot{x} = u = \frac{\partial \Psi}{\partial y} \tag{2.3}$$

$$\dot{y} = v = -\frac{\partial \Psi}{\partial x}. \tag{2.4}$$

In the case of a steady flow, the pathlines coincide with streamlines, i.e. the level curves $\Psi(x, y) =$ constant. It is easy to realize that (2.3) and (2.4) define a Hamiltonian problem, where the streamfunction is the Hamiltonian itself and the space variables (x, y) are the canonical variables defining the phase space.

We assume that the flow is created by a set of N point vortices, or a singular distribution of vorticity. A point vortex can be considered as an idealized stirrer. We can then write the vorticity field as :

$$\omega(x, y) = \sum_{i=1}^{N} \Gamma_i \delta(x - x_i)\delta(y - y_i) \tag{2.5}$$

where Γ_i is the circulation, strength of the i^{th} vortex and δ is the Dirac delta function. By taking the curl of the system (2.3)-(2.4), the streamfunction and the vorticity field are related by the following equation:

$$\triangle \Psi = -\omega. \tag{2.6}$$

By solving (2.6), using the Green's function for two-dimensional free space, we obtain

$$\Psi(x, y) = H(x, y) = -\frac{1}{2\pi} \sum_{i=1}^{N} \Gamma_i \log |z - z_i| \tag{2.7}$$

where $z = x + iy$ and $z_i = z_i + iy_i$; the complex notation is used here for convenience. Notice that the Hamiltonian (2.7) is expressed in a fixed frame of reference, denoted by $\mathcal{R}$.

For an autonomous system, i.e. independent of time, the Hamiltonian has one degree of freedom, independently of the number of vortices N and is therefore integrable.

The system can be integrated by quadratures, through action-angle variables, and chaos cannot occur in this system [4], [15].

However, it is known that adding time dependency to such a system can produce chaotic behavior [26]. Here, we introduce the time dependency in the position of the vortex and consider a moving set of vortices $z_i(t)$. Hereafter, we keep in mind that in the mixing problem studied here, the motion is prescribed and not part of the problem; that is, for instance, interacting vortices are not considered. The experimentalist imposes the motion of the vortices and their motion can be seen as a part of the mixing protocol.

In order to study a non-autonomous Hamiltonian, i.e explicitly time dependent, a procedure known as "phase space extension" is used. The idea is to introduce a new pair of canonical variables (τ, E), or add a new degree of freedom to the system to obtain an autonomous Hamiltonian. This is achieved by introducing a new parametrization of time. The details of the procedure, especially the consequences on the different invariants can be found in [4], [26], [42]. It is important to notice that this phase space extension does not give any additional information about the dynamics and the "extended" set of canonical equations used to solve the problem is equivalent to the conventional one. For our problem, we perform the trivial parametrization $\tau = \tau(t) = t$ and define the new Hamiltonian :

$$H(x, y; \tau, E) = -\frac{1}{2\pi} \sum_{i=1}^{N} \Gamma_i \ln |z - z_i(\tau)| + E \tag{2.8}$$

with the following Hamilton equations :

$$\dot{x} = \frac{\partial H}{\partial y} \qquad \dot{\tau} = \frac{\partial H}{\partial E} = 1 \tag{2.9}$$

$$\dot{y} = -\frac{\partial H}{\partial x} \qquad \dot{E} = -\frac{\partial H}{\partial \tau}. \tag{2.10}$$

Here τ plays the role of time, and the equations for (x, y) are actually unchanged. The new variable E, which is the conjugate of τ, is necessary to keep the dimension of the phase space even, which is required by its symplectic structure.

Consequently, the study of a two-dimensional incompressible flow, with N moving point vortices is equivalent to the following problem with the following Hamiltonian

$$H(x, y; \tau, E) = -\frac{1}{2\pi} \sum_{i=1}^{N} \Gamma_i \ln |z - z_i(\tau)| + E \tag{2.11}$$

and its corresponding equations

$$\dot{x} = \frac{\partial H}{\partial y} \qquad \dot{\tau} = \frac{\partial H}{\partial E} = 1 \tag{2.12}$$

$$\dot{y} = -\frac{\partial H}{\partial x} \qquad \dot{E} = -\frac{\partial H}{\partial \tau} \tag{2.13}$$

where "$\dot{}$" denotes the derivative with respect to the real time t. This system has two degrees of freedom and may produce chaotic behavior, depending upon the motion of the vortices.

2.2 Problem Description

We now consider the physical problem of an incompressible fluid within a circular container of radius a. Without loss of generality, we set $a = 1$. The flow is generated by a point vortex, which models the stirrer. The position of the latter, considered fixed for the moment, is given by $z_v = exp(-b + i\alpha)$ (see Figure (2.1)).

By using the method of images and considering the boundary condition $H_{\text{boundary}}(x, y) =$ constant, whereby the container itself is a streamline, the general form of the Hamiltonian is

$$H(x, y) = -\frac{\Gamma}{2\pi} \ln \left| \frac{z - e^{-b+i\alpha}}{z - e^{b+i\alpha}} \right|. \tag{2.14}$$

In this case of a constant vortex, the streamlines or level curves of $\tilde{H}(x, y)$ are non-concentric circles around the vortex (see Figure (2.2)).

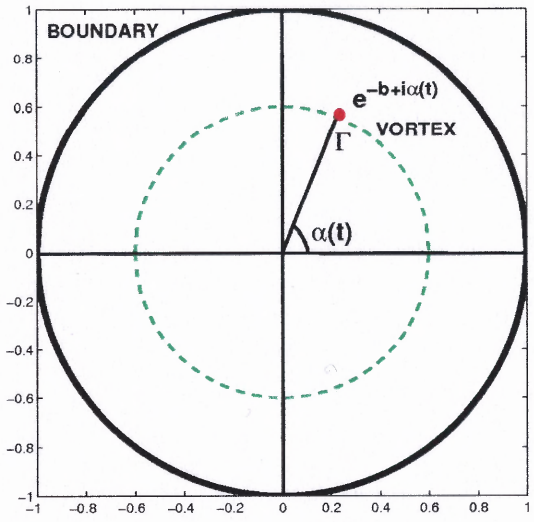

Figure 2.1 Schematic for the problem.

In this simple case, we give the solution $z(t)$ for the motion of a passive particle. We first start with the standard approach based on the fact that $\Psi(x,y) = H(x,y) = const$ along the trajectory. We then use the Hamiltonian formulation to introduce a simple canonical transformation to obtain the action-angle variables.

For the sake of simplicity, since the angle α is irrelevant, we take $\alpha = 0$. The trajectories are given by the level curves of $H(x,y) = cst = B$ where B is the value of the Hamiltonian (or energy) at the initial position $z(t=0)$. Since the trajectories are non-concentric circles, we look for a solution of the form (see Figure (2.3)):

$$z(t) = z_c + \rho e^{i\phi(t)}. \tag{2.15}$$

After calculation, we obtain

$$z_c = \frac{\sinh(\frac{2\pi B}{\Gamma} - b)}{\sinh(\frac{2\pi B}{\Gamma})} \tag{2.16}$$

$$\rho = \frac{\sinh(b)}{\sinh(\frac{2\pi B}{\Gamma})} \tag{2.17}$$

which implies that the center of the circle depends on B, or the initial condition. For $B = \frac{\Gamma b}{2\pi}$, we have $z_c = 0$ and $\rho = 1$; this is for an initial condition on the boundary,

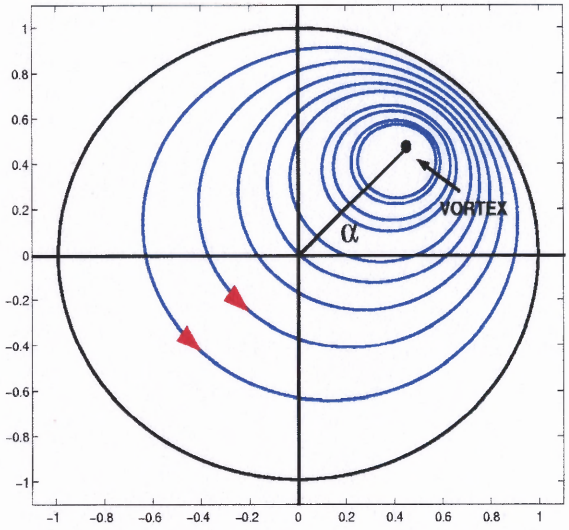

Figure 2.2 Streamlines for a fixed vortex.

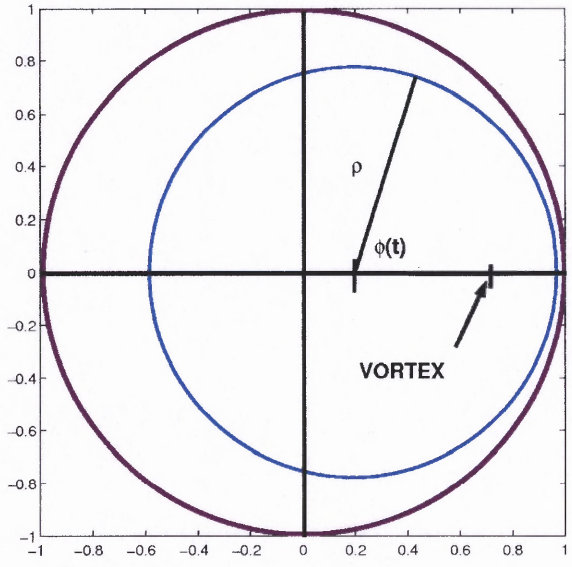

Figure 2.3 Schematic for the case of a fixed vortex

where the energy of the system, or value of the Hamiltonian, is $H_{\text{boundary}} = B = \frac{\Gamma b}{2\pi}$. For $B \to \infty$, we have $z_c \to e^{-b}$ and $\rho \to 0$; this corresponds to an initial condition closer and closer to the vortex. In this case, the energy (Hamiltonian) tends to infinity due to the logarithmic singularity, and $\phi(t)$ satisfies the following equation :

$$\phi(t) - \frac{\sin(\phi(t))}{\cosh(\frac{2\pi B}{\Gamma})} = t\frac{\sinh^3(\frac{2\pi B}{\Gamma})}{\cosh(\frac{2\pi B}{\Gamma})\sinh^2(b)} \tag{2.18}$$

with $\phi(0) = 0$. This equation is known in celestial mechanics, from Kepler's problem $u - e\sin(u) = \tau$, where e is the eccentricity. A solution can be written explicitly in terms of Bessel functions of the first kind [45] :

$$u(\tau) = \tau + 2\sum_{n=1}^{\infty} J_n(n.e)\frac{\sin(n\tau)}{n}. \tag{2.19}$$

The infinite sum is known as Kapteyn's series which is rapidly convergent for $e < 1$ and still convergent for $e = 1$. We now adopt the Hamiltonian approach and show that it is possible to study the same problem in a very simple way.

The problem has one degree of freedom, and is consequently integrable. It is well known that special variables, the action-angle variables (A, θ), can be found such that the Hamiltonian depends only on the action A. We thus look for a transformation $(x, y) \rightarrow (A, \theta)$ satisfying :

$$dx \wedge dy = dA \wedge d\theta \tag{2.20}$$

where x, y, A, θ are functions of B, ϕ, which are the previously defined intermediate variables that are not canonical. After expanding the wedge product and using the fact that $x = x_c + \rho\cos(\phi), y = y_c + \rho\sin(\phi)$

$$\begin{aligned}
(\frac{\partial x}{\partial B}dB + \frac{\partial x}{\partial \phi}d\phi) \wedge (\frac{\partial y}{\partial B}dB + \frac{\partial y}{\partial \phi}d\phi) =& (\frac{\partial A}{\partial B}dB + \frac{\partial A}{\partial \phi}d\phi) \wedge (\frac{\partial \theta}{\partial B}dB + \frac{\partial \theta}{\partial \phi}d\phi) \\
(\frac{\partial x}{\partial B}\frac{\partial y}{\partial \phi} - \frac{\partial x}{\partial B}\frac{\partial y}{\partial B})dB \wedge d\phi =& (\frac{\partial A}{\partial B}\frac{\partial \theta}{\partial \phi} - \frac{\partial A}{\partial \phi}\frac{\partial \theta}{\partial B})dB \wedge d\phi \\
\frac{\sinh^2(b)}{\sinh^3(\frac{2\pi B}{\Gamma})}(\cos(\phi) - \cosh(\frac{2\pi B}{\Gamma})) =& \frac{\partial A}{\partial B}\frac{\partial \theta}{\partial \phi} - \frac{\partial A}{\partial \phi}\frac{\partial \theta}{\partial B}.
\end{aligned}$$

We choose A independent of ϕ, and take

$$A(B, \phi) = \frac{1}{2}\left(\frac{\sinh(b)}{\sinh(\frac{2\pi B}{\Gamma})}\right)^2 \tag{2.21}$$

$$\theta(B, \phi) = \phi - \frac{\sin(\phi)}{\cosh(\frac{2\pi B}{\Gamma})}. \tag{2.22}$$

The equation (2.21) can be inverted :

$$B = \frac{\Gamma}{2\pi} \log\left(\frac{\sinh(b)}{\sqrt{2A}} + \sqrt{\frac{\sinh^2(b)}{2A} + 1}\right) \tag{2.23}$$

Consequently,

$$H(A,\theta) = \frac{\Gamma}{2\pi} \log\left(\frac{\sinh(b)}{\sqrt{2A}} + \sqrt{\frac{\sinh^2(b)}{2A} + 1}\right). \tag{2.24}$$

Notice that this Hamiltonian is valid for a fixed vortex only. The Hamiltonian equations then become trivial:

$$\dot{A} = \frac{\partial H}{\partial \theta} = 0 \Rightarrow A = cst \tag{2.25}$$

$$\dot{\theta} = -\frac{\partial H}{\partial A} = \omega(A) \Rightarrow \theta = \omega(A)t \tag{2.26}$$

with $\omega(A) = \frac{\Gamma}{2\pi} \frac{\sinh(b)}{2A\sqrt{2A+\sinh^2(b)}}$. A refers to the parametrization of the circles, $A \in [0; 1/2]$; $A = 1/2$ on the boundary (unit circle), and $H(1/2, \theta) = \frac{\Gamma b}{2\pi}$ and $A = 0$ on the vortex, $H(0, \theta) = \infty$. The energy values are consistent with the ones previously found.

In summary, the problem of the fixed vortex is trivial. In this case, a solution can be explicitly written as an infinite sum of Bessel functions of the first kind (first approach). By using a second (Hamiltonian) approach, the Hamiltonian itself can be simplified through the action-angle variables, which leads to a very simple solution. It is worth mentioning, however, that this simplification has a cost: the canonical transformation used to obtain the action-angle variables can be difficult to find. In any case, it is easy to show that the case of a fixed vortex leads to very simple trajectories and that in this situation the flow is not chaotic.

We now consider the physical problem in which a stirrer rotates within the fluid domain along a circle concentric with the circular container. For this, we introduce the azimuthal motion of the vortex through the time dependence of the angle $\alpha \rightarrow \alpha(t)$, which makes the Hamiltonian time dependent. In order to account for this time

dependency, we extend the phase space as before and write the new Hamiltonian in the form

$$\tilde{H}(x,y;\tau,E) = -\frac{\Gamma}{2\pi}\ln\left|\frac{z-e^{-b+i\alpha(\tau)}}{z-e^{b+i\alpha(\tau)}}\right| + E \tag{2.27}$$

with the corresponding Hamilton equations

$$\dot{x} = \frac{\partial\tilde{H}}{\partial y}\ ,\dot{y} = -\frac{\partial\tilde{H}}{\partial x}\ ;\ \dot{\tau} = \frac{\partial\tilde{H}}{\partial E} = 1\ ,\dot{E} = -\frac{\partial\tilde{H}}{\partial\tau}. \tag{2.28}$$

For the sake of simplicity, it is useful to study the flow dynamics in the frame of reference of the vortex, denoted hereafter by $\mathcal{R}_v$. For this, we introduce the change of variables $(x,y;\tau,E) \rightarrow (X,Y;\tau,F)$ defined by the rotation $Z(\tau) = X + iY = z(\tau)e^{-i\alpha(\tau)}$. The relation between the old and new canonical variables needs to satisfy (see Appendix A)

$$dx\wedge dy + d\tau\wedge dE = dX\wedge dY + d\tau\wedge dF \tag{2.29}$$

where X,Y,F are functions of (x,y,τ). Looking for a solution such that $F = E + f(x,y,\tau)$ and expanding the wedge products, we compute that

$$\begin{aligned}
dX\wedge dY + d\tau\wedge dF =& (\frac{\partial X}{\partial x}dx + \frac{\partial X}{\partial y}dy + \frac{\partial X}{\partial\tau}d\tau)\wedge(\frac{\partial Y}{\partial x}dx + \frac{\partial Y}{\partial y}dy + \frac{\partial Y}{\partial\tau}d\tau)\\
&+ d\tau\wedge(dE + \frac{\partial f}{\partial x}dx + \frac{\partial f}{\partial y}dy + \frac{\partial f}{\partial\tau}d\tau)\\
=& (\frac{\partial X}{\partial x}\frac{\partial Y}{\partial y} - \frac{\partial X}{\partial y}\frac{\partial Y}{\partial x})dx\wedge dy + (\frac{\partial X}{\partial x}\frac{\partial Y}{\partial\tau} - \frac{\partial X}{\partial\tau}\frac{\partial Y}{\partial x})dx\wedge d\tau +\\
&(\frac{\partial X}{\partial y}\frac{\partial Y}{\partial\tau} - \frac{\partial X}{\partial\tau}\frac{\partial Y}{\partial y})dy\wedge d\tau + d\tau\wedge dE + \frac{\partial f}{\partial x}d\tau\wedge dx\\
&+ \frac{\partial f}{\partial y}d\tau\wedge dy
\end{aligned}$$

with $X = x\cos(\alpha(\tau)) + y\sin(\alpha(\tau))$, $Y = y\cos(\alpha(\tau)) - x\sin(\alpha(\tau))$. After some simplification, equation (2.29) becomes :

$$dx\wedge dy + d\tau\wedge dE = dx\wedge dy + d\tau\wedge dE - (\frac{\partial\alpha}{\partial\tau}x + \frac{\partial f}{\partial x})dx\wedge d\tau - (\frac{\partial\alpha}{\partial\tau}y + \frac{\partial f}{\partial y})dy\wedge d\tau$$

leading to the following scalar partial differential equations for the function $f(x, y, \tau)$.

$$\frac{\partial f}{\partial x} = -\frac{\partial \alpha(\tau)}{\partial \tau} x \tag{2.30}$$

$$\frac{\partial f}{\partial y} = -\frac{\partial \alpha(\tau)}{\partial \tau} y. \tag{2.31}$$

Integrating equations (2.30) and (2.31) leads to the following expression for $f(x, y)$

$$f(x, y) = -\frac{1}{2}\frac{\partial \alpha(\tau)}{\partial \tau}(x^2 + y^2) = -\frac{1}{2}\frac{\partial \alpha(\tau)}{\partial \tau}|z|^2 = -\frac{1}{2}\frac{\partial \alpha(\tau)}{\partial \tau}|Z|^2. \tag{2.32}$$

It follows that, in the moving frame of reference $\mathfrak{R}_v$, the new Hamiltonian takes the form

$$H(X, Y; \tau, F) = -\frac{\Gamma}{2\pi} \ln \left| \frac{Z - e^{-b}}{Z - e^{b}} \right| + \frac{1}{2}\frac{\partial \alpha(\tau)}{\partial \tau}|Z|^2 + F \tag{2.33}$$

with the Hamiltonian equations

$$\dot{X} = \frac{\partial H}{\partial Y}, \dot{Y} = -\frac{\partial H}{\partial X}\ ;\ \dot{\tau} = \frac{\partial H}{\partial F} = 1\ , \dot{F} = -\frac{\partial H}{\partial \tau}. \tag{2.34}$$

So far, we have not made any assumption on $\alpha(t)$. In the following section, we consider the simplest time dependency which allows us to make a complete analysis of the phase space.

2.3 Hamiltonian for a Vortex Rotating at Uniform Speed

Since the first derivative of $\alpha(t)$ appears in (2.33), we take the particular case of a vortex rotating along a circular trajectory within the container at constant angular velocity. In this case, the time dependency of the angle α reduces to $\alpha(t) = \omega t$, where ω is a constant corresponding to the rotational vortex speed. This implies that the "time" dependent term in the Hamiltonian (2.33) expressed in the moving frame of reference becomes a constant, thus allowing us to recover an autonomous system.

We have

$$H(X,Y;\tau,F) = -\frac{\Gamma}{2\pi}\ln\left|\frac{Z-e^{-b}}{Z-e^{b}}\right| + \frac{\omega}{2}|Z|^2 + F. \tag{2.35}$$

After introducing the dimensionless time variable $\bar{t} = t/\omega$, the Hamilton equations take the form

$$\dot{X} = Y\left(1 + \frac{1}{\beta}\frac{2\sinh(b)(X-\cosh(b))}{\left(\left(X-e^{-b}\right)^2+Y^2\right)\left(\left(X-e^{b}\right)^2+Y^2\right)}\right) \tag{2.36}$$

$$\dot{Y} = -X + \frac{1}{\beta}\frac{\sinh(b)\left(Y^2-\left(X-e^{-b}\right)\left(X-e^{b}\right)\right)}{\left(\left(X-e^{-b}\right)^2+Y^2\right)\left(\left(X-e^{b}\right)^2+Y^2\right)} \tag{2.37}$$

$$\dot{\tau} = \omega \tag{2.38}$$

$$\dot{F} = 0 \tag{2.39}$$

where " $\dot{}$ " denotes $d/d\bar{t}$, and $\beta = \frac{\omega\pi}{\Gamma}$ is a dimensionless parameter which is the ratio of two rotational speeds. One can clearly see, in this case, that the phase space is composed of two independent subspaces (X,Y) and (τ,F) and that the system is integrable since it consists of two integrable (of one degree of freedom) and independent subspaces. In the subspace (τ,F), in which we refer to the "action" F and "angle" τ variables, the dynamics is trivial. It is possible, at least theoretically, to find the action-angle variables in the subspace (X,Y); unfortunately, they have not been found and we restrict our study to the subspace (X,Y). Even though the full problem depends on three parameters (b,Γ,ω), the subspace (X,Y) reduces to a two parameter problem (b,β). This implies that if we consider two different experiments with the same $\beta = \frac{\omega\pi}{\Gamma}$, the structure of the flow in the subspace (X,Y) will be the same, but the dynamics will evolve faster or slower according to the value of ω in each experiment, i.e $\dot{\tau} = \omega$.

A complete analysis of the dynamics in the latter subspace (X,Y) fully describes the flow in the physical plane within the container. In order to carry out such an

analysis, we examine the fixed points $Z^* = X^* + iY^*$ of the system, together with their stability properties. As we will see in the next section, the number and nature of the fixed points depends on the particular location in the parameter space (b, β). This leads to a bifurcation diagram where the dynamics differs in various regions of the $b\beta$-plane.

Hereafter, the position of the vortex in the rotating frame of reference, centered at $(0,0)$, is denoted by $(X_v, 0) = (e^{-b}, 0)$. In addition, we restrict the study of the dynamics in the subspace (X, Y) to the unit disk, corresponding to the physical fluid domain.

CHAPTER 3

PHASE SPACE ANALYSIS

For an incompressible flow created by a uniformly rotating vortex, the system of equations describing the motion of a passive particle within the unit disk are

$$\dot{X} = Y\left(1+\frac{1}{\beta}\frac{2\sinh(b)(X-\cosh(b))}{\left(\left(X-e^{-b}\right)^2+Y^2\right)\left(\left(X-e^{b}\right)^2+Y^2\right)}\right) \tag{3.1}$$

$$\dot{Y} = -X+\frac{1}{\beta}\frac{\sinh(b)\left(Y^2-\left(X-e^{-b}\right)\left(X-e^{b}\right)\right)}{\left(\left(X-e^{-b}\right)^2+Y^2\right)\left(\left(X-e^{b}\right)^2+Y^2\right)}. \tag{3.2}$$

3.1 Fixed Points

In this section, we concentrate on finding the fixed points $Z^* = X^* + iY^*$ of the Hamiltonian equations (3.1), (3.2); that is, locations in the container where fluid particles are at rest in the moving frame of reference $\mathcal{R}_v$. Notice that such fixed points correspond to limit cycles in the fixed frame of reference $\mathcal{R}$, corresponding to fluid particles traveling along circular trajectories with angular velocity ω for a fixed observer. Fixed points (X^*, Y^*) for an observer traveling with the vortex are obtained by setting $\dot{X}$ and $\dot{Y}$ equations (3.1),(3.2) to zero, that is

$$Y^*\left(1+\frac{1}{\beta}\frac{2\sinh(b)(X^*-\cosh(b))}{\left(\left(X^*-e^{-b}\right)^2+Y^{*2}\right)\left(\left(X^*-e^{b}\right)^2+Y^{*2}\right)}\right) = 0 \tag{3.3}$$

$$-X^*+\frac{1}{\beta}\frac{\sinh(b)\left(Y^{*2}-\left(X^*-e^{-b}\right)\left(X^*-e^{b}\right)\right)}{\left(\left(X^*-e^{-b}\right)^2+Y^{*2}\right)\left(\left(X^*-e^{b}\right)^2+Y^{*2}\right)} = 0. \tag{3.4}$$

Looking for solutions of the system of algebraic equations (3.3),(3.4), we first concentrate on the family of fixed points located on the X-axis, i.e. such that $Y^* = 0$, which systematically satisfy (3.3). Equation (3.4) immediately leads to the following condition for such fixed points:

$$f(X^*) = X^*(X^*-e^{-b})(X^*-e^{b})+\frac{1}{\beta}\sinh(b) = 0. \tag{3.5}$$

This third degree polynomial has in general three roots. However, the particular values of the two parameters b and β determine the number and type of roots, and consequently the structure of the phase space. The position of the local maxima and minima of the cubic polynomial are independent of β :

$$\text{local maxima :} \quad X_c^* = \tfrac{1}{3}(2\cosh(b) - \sqrt{2\cosh(2b) - 1}) \in (-1, X_v) \tag{3.6}$$

$$\text{local minima :} \quad \bar{X}_c = \tfrac{1}{3}(2\cosh(b) + \sqrt{2\cosh(2b) - 1}) > 1. \tag{3.7}$$

For the case of three real roots, i.e. $f(X_c^*) > 0$ and $f(\bar{X}_c) < 0$, one root will be located at $X^* > \bar{X}_c > 1$ outside the domain $[-1, 1]$. Consequently there will be at most 2 roots on the interval $[-1, 1]$.

A degenerate root (double root) located at X_c^* can be found for a particular value of β :

$$\beta_c = \beta_c(b) \quad = -\frac{\sinh(b)}{X_c^* - 2\cosh(b)X_c^{*2} + X_c^{*3}} < 0. \tag{3.8}$$

Remark: Varying the values of β is equivalent to shifting the cubic polynomial $f(X^*)$ up and down .

For values of β such that $\beta < \beta_c$, we have two simple roots ($f(X_c^*) > 0$), one in the interval $[0, X_c]$ and the other one in $[X_c, X_v]$. For $\beta_c < \beta < 0$, there is no fixed point on $[-1, 1]$.

For $\beta > 0$, we can substitute $X^* = \pm 1$ into (3.5), i.e. the fixed points on the boundary, and find a relation between β and b :

$$\text{For } X^* = +1 \Rightarrow \beta_{+1} = \frac{1}{2}\coth(\frac{b}{2}) > 0 \tag{3.9}$$

$$\text{For } X^* = -1 \Rightarrow \beta_{-1} = \frac{1}{2}\tanh(\frac{b}{2}) > 0. \tag{3.10}$$

For $\beta < \beta_{-1}$, we have no roots on $[-1, 1]$. For $\beta \geq \beta_{-1}$, we have only one root on $[-1, 1]$ starting at $X^* = -1$ and moving to the right as β increases. Then for $\beta = \beta_{+1}$,

a second root appears at $X^* = +1$. Therefore, for $\beta > \beta_{+1}$, we have two simple roots in $[-1, 1]$.

A second family of fixed points exists on the unit circle, i.e $Z^* = e^{i\theta}$. By performing a change of variables into polar coordinates and noticing that the circle is an invariant curve, the equation $\dot{\theta} = 0$ leads to

$$\cos(\theta) = \left(\cosh(b) - \frac{\sinh(b)}{2\beta}\right) \quad \text{valid for} \quad \beta_{-1} < \beta < \beta_{+1} \tag{3.11}$$

where θ is the angle with respect to the X-axis. Consequently, in the range $\beta \in (\beta_{-1}, \beta_{+1})$, we have two fixed points on the boundary located symmetrically with respect to the X-axis.

Remark: The relation (3.5) is not valid for the particular parameter value $\beta = 0$. However, in this case, we have a fixed vortex, i.e $\omega = 0$, and therefore there exists no fixed point within the fluid domain.

In summary, we have in the fluid domain within the unit circle

- one fixed point
  double root : $(X_c^*, 0)$ for $\beta = \beta_c$
  simple root : $(-1, 0)$ for $\beta = \beta_{-1}$
- two fixed points (simple roots)
  $X_1^* \in [X_v, +1]$ and $X_2^* \in [-1, X_c^*]$ for $\beta \geq \beta_{+1}$
  $X_1^* \in [-1, X_c^*]$ and $X_2^* \in [X_c^*, X_v]$ for $\beta < \beta_c$.
- one fixed point (simple root) $(X^*, 0)$ where $X^* \in (-1, X_c^*)$ and two symmetrical fixed points on the boundary at $Z^* = e^{i\theta}$ where θ is determined by Equation (3.11) for $\beta_{-1} < \beta < \beta_{+1}$.

The relations between β and b, (3.8),(3.9) and (3.10), correspond to three distinct curves in the (b, β) -plane (see Figure (3.1)), defining four distinct regions with their own phase space dynamics.

We will return to the description of this bifurcation diagram after studying the stability of the fixed points and the bifurcations.

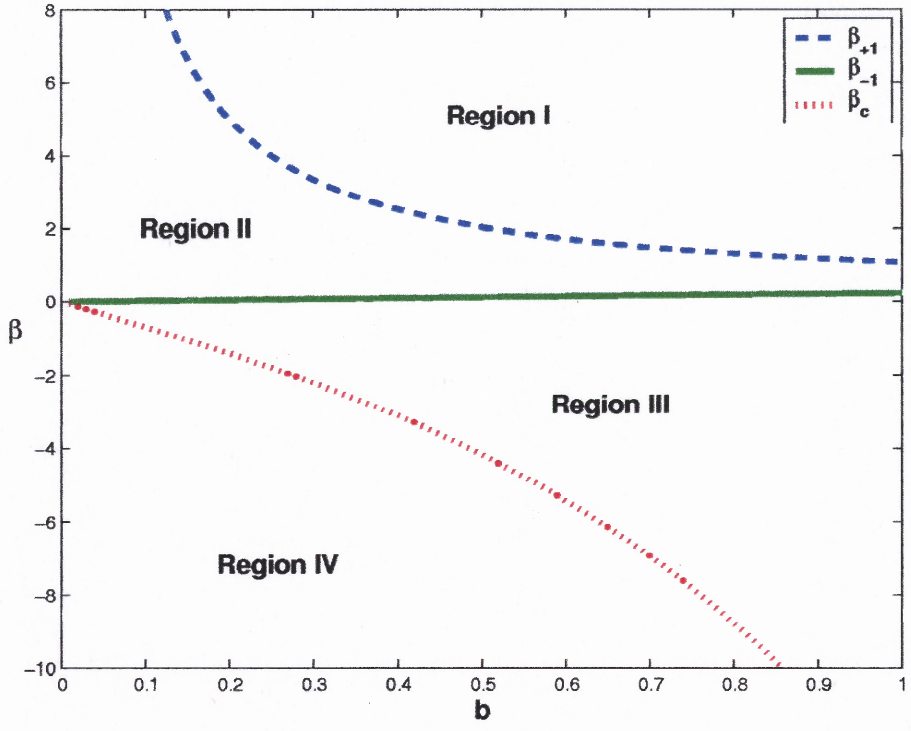

Figure 3.1 Bifurcation diagram in the parameter space (b, β)

3.2 Stability of the Non-Degenerate Fixed Points

In this section, we study the stability of the fixed points, $Z^* = X^* + iY^*$, determined previously. The following calculations were performed using the mathematical software *Mathematica* [28]. By considering the dynamics in a neighborhood of the fixed point, i.e. $Z^* + \xi$, where ξ is a perturbation in the complex plane, the problem is reduced to the following linear system

$$\dot{\xi} = J\xi \tag{3.12}$$

where J is the Jacobian matrix that, for a Hamiltonian problem, can be written as

$$J = \begin{pmatrix} \frac{\partial^2 H}{\partial x \partial y} & \frac{\partial^2 H}{\partial y^2} \\ -\frac{\partial^2 H}{\partial x^2} & -\frac{\partial^2 H}{\partial y \partial x} \end{pmatrix} = \begin{pmatrix} J_{11} & J_{12} \\ J_{21} & J_{22} \end{pmatrix} \text{ with } J_{11} = -J_{22}. \tag{3.13}$$

From Equations (3.1)-(3.2), we can show the following relation between the off-diagonal elements of the Jacobian matrix

$$J_{12} = J_{21} + 2. \tag{3.14}$$

By considering the eigenvalues of the Jacobian matrix at the various fixed points, in the case where the latter are hyperbolic (i.e. with no eigenvalues with zero real part), we can determine locally the dynamics of the solution near the fixed points and understand the local structure of the streamlines inside the container.

3.2.1 Stability of Fixed Points on the X-axis

By substituting $Y^* = 0$ into Equation (3.13), the Jacobian matrix can be reduced to:

$$J = \begin{pmatrix} 0 & J_{12}(X^*(b,\beta),b,\beta) \\ J_{12}(X^*(b,\beta),b,\beta) - 2 & 0 \end{pmatrix} \tag{3.15}$$

where

$$J_{12}(X^*(b,\beta),b,\beta) = 1 + \frac{2\sinh(b)(X^* - \cosh(b))}{\beta(X^* - e^b)^2(X^* - e^{-b})^2}. \tag{3.16}$$

In this case, $X^*(b,\beta)$ is a solution of Equation (3.5), explicitly given in Appendix A.

The eigenvalues of the Jacobian matrix can then be fully determined by using (3.5) to obtain

$$\lambda^2 = \frac{(X^{*2} - 1)(3X^{*2} - 4X^*\cosh(b) + 1)}{(X^* - e^b)^2(X^* - e^{-b})^2} \tag{3.17}$$

which is formally a function of the dimensionless parameters b and β only, since X^* is itself a function of these two parameters.

By considering the sign of the numerator of Equation (3.17), we can show that the right-hand side (rhs) of equation (3.17) is negative on the segment $[-1, X_c^*]$, so the fixed points are elliptic, or centers, on this interval and positive on the segment

$(X_c^*, X_v) \cup (X_v, +1)$, so the fixed points are hyperbolic, or saddle points, on this interval. In general, the above elliptic points have a two-dimensional center eigenspace, while the saddle points have a one-dimensional stable eigenspace and a one-dimensional unstable eigenspace.

From equation (3.17), we find three cases for which the Jacobian matrix has a double zero eigenvalue. These degenerate cases correspond to specific fixed points in the phase plane. More precisely, those located at

- $(-1, 0)$ for $\beta = \beta_{-1} = \frac{1}{2}\tanh(\frac{b}{2})$
- $(X_c, 0)$ for $\beta = \beta_c$
- $(+1, 0)$ for $\beta = \beta_{+1} = \frac{1}{2}\coth(\frac{b}{2})$

Since for these fixed points the eigenvalues have zero real part, we cannot linearize the system as $\dot{\xi} = J\xi$ (Hartman-Grobman theorem). Another approach such as that using Normal Forms is needed in order to determine the flow locally around these fixed points as well as their bifurcations, if any (see Section 3.3).

3.2.2 Stability of Fixed Points On the Boundary

The second family of fixed points on the boundary for the particular interval $\beta_{-1} < \beta < \beta_{+1}$ are two fixed points located symmetrically to one another with respect to the X-axis and moving along the boundary as β varies. Their position is given by

$$\cos(\theta) = \left(\cosh(b) - \frac{\sinh(b)}{2\beta}\right) \quad \text{valid for} \quad \beta_{-1} < \beta < \beta_{+1} \tag{3.18}$$

where θ is the angle with respect to the X-axis.

The corresponding eigenvalues are λ_{1c} and λ_{2c} given as

$$\lambda_{1c,2c}^2 = -4\left(\beta - \frac{1}{2}\coth\left(\frac{b}{2}\right)\right)\left(\beta - \frac{1}{2}\tanh\left(\frac{b}{2}\right)\right). \tag{3.19}$$

On the β interval considered here, the right hand side of Equation (3.19) is always positive. Consequently, on the boundary, the fixed points are all saddle points.

The boundary, i.e. the unit circle, is an invariant curve in our system defining one stable and unstable manifold of these saddle points and connecting the two saddle points to one another through a heteroclinic orbit. Another heteroclinic orbit is found numerically inside the container (see Figure 3.7).

3.3 Bifurcation Analysis, Normal Form

In this section, we study in detail the degenerate fixed points, i.e with double zero eigenvalues, and their bifurcations. This case is known as Takens-Bogdanov bifurcation, named after two mathematicians who studied it independently in the 70's [9], [44]. The degeneracy of these fixed points can lead to different bifurcation scenarios, but the fact that our system is Hamiltonian prevents certain bifurcations from occurring. As we will see below, this constraint will allow us to identify the right bifurcation from the different possibilities. In Appendix (B.2), we give some details on the normal form approach, as well as the notation that we are going to use below.

3.3.1 Degenerate Fixed Points on the Boundary

The study of both fixed points can be carried out simultaneously since they involve the same Jacobian and lead to the same normal form. We will point out the differences when necessary, especially in the bifurcation diagram.

The two degenerate fixed points are located at $(-1, 0)$ with $\beta = \beta_{-1}$ and at $(0, +1)$ for $\beta = \beta_{+1}$. Their Jacobian reduces to

$$A = \begin{pmatrix} 0 & 0 \\ -2 & 0 \end{pmatrix} \tag{3.20}$$

We introduce new spatial variables (u, v) with $u = X + 1$, $v = Y$ (resp. $u = X - 1$, $v = Y$), and a new time $t' = 2t$ to normalize the Jacobian. We can formally write

the system (3.1)-(3.2) as

$$\begin{pmatrix} \dot{u} \\ \dot{v} \end{pmatrix} = \begin{pmatrix} 0 & 0 \\ -1 & 0 \end{pmatrix} \begin{pmatrix} u \\ v \end{pmatrix} + \begin{pmatrix} \sum \alpha_k u^i v^j \\ \sum \beta_k u^i v^j \end{pmatrix} \tag{3.21}$$

where α_k, β_k are the coefficients of the Taylor expansion of the right-hand side of the system of ODEs starting from the second order.

In order to put the Jacobian into its Jordan form, we introduce the linear transformation : $P = \begin{pmatrix} 0 & -1 \\ 1 & 0 \end{pmatrix}$ and its inverse $P^{-1} = \begin{pmatrix} 0 & 1 \\ -1 & 0 \end{pmatrix}$. We first make the following change of variables: $u \to -\eta$ and $v \to \xi$, i.e. $\begin{pmatrix} u \\ v \end{pmatrix} = P \begin{pmatrix} \xi \\ \eta \end{pmatrix}$.

Hence, we can write

$$\frac{d}{dt} P \begin{pmatrix} \xi \\ \eta \end{pmatrix} = AP \begin{pmatrix} \xi \\ \eta \end{pmatrix} + \begin{pmatrix} \sum \alpha_k (-\eta)^i \xi^j \\ \sum \beta_k (-\eta)^i \xi^j \end{pmatrix}. \tag{3.22}$$

We then multiply on the left by P^{-1}

$$\frac{d}{dt} \begin{pmatrix} \xi \\ \eta \end{pmatrix} = P^{-1}AP \begin{pmatrix} \xi \\ \eta \end{pmatrix} + P^{-1} \begin{pmatrix} \sum \alpha_k (-\eta)^i \xi^j \\ \sum \beta_k (-\eta)^i \xi^j \end{pmatrix} \tag{3.23}$$

with $P^{-1}AP = J = \begin{pmatrix} 0 & 1 \\ 0 & 0 \end{pmatrix}$.

$$\frac{d}{dt} \begin{pmatrix} \xi \\ \eta \end{pmatrix} = \begin{pmatrix} 0 & 1 \\ 0 & 0 \end{pmatrix} \begin{pmatrix} \xi \\ \eta \end{pmatrix} + P^{-1} \begin{pmatrix} \sum \alpha_k (-\eta)^i \xi^j \\ \sum \beta_k (-\eta)^i \xi^j \end{pmatrix}. \tag{3.24}$$

In the right hand side, the second term at the quadratic order reduces to

$$f_2 = \begin{pmatrix} d\xi^2 \\ -d\xi\eta \end{pmatrix} \tag{3.25}$$

where we have

$$d = \frac{1+2\cosh(b)}{1+\cosh(b)} > 1 \text{ at } (-1,0) \tag{3.26}$$

$$d = \frac{1-2\cosh(b)}{2\cosh^2(\frac{b}{2}))} < 0 \text{ at } (+1,0). \tag{3.27}$$

We choose here the basis $\mathbb{G}_2 : (2p_1 + p_5)$ and p_4.

Consequently, the resonant term is

$$f_2^R = \begin{pmatrix} d\xi^2 \\ -d\xi\eta \end{pmatrix}. \tag{3.28}$$

In this case, the normal form is actually equivalent to a Taylor expansion since we kept all the terms in f_2 due to the choice of the basis for $\mathbb{G}_2$. If we make another choice such as that described in Appendix (B.2), then the right bifurcation is more difficult to obtain and we have to go to higher order terms in the normal form and the unfolding. Consequently, it becomes harder to find a simpler form of the equation than derive a regular Taylor expansion. Here is an example of the difference between a generic normal form, and a universal (or versal) unfolding and a normal form adapted to the problem. Since, the normal form is not unique, we choose the simplest one and do not follow Appendix B which is more interesting from mathematical viewpoint. It follows that the normal form up to the cubic order is given by

$$\begin{aligned} \dot{\xi} &= \eta + d\xi^2 \\ \dot{\eta} &= -d\xi\eta \end{aligned} \tag{3.29}$$

where d is defined by (3.26). We unfold this system as follows.

$$\begin{aligned} \dot{\xi} &= \mu_1 + \eta + d\xi^2 \\ \dot{\eta} &= \mu_2\eta - d\xi\eta. \end{aligned} \tag{3.30}$$

Studying this unfolded system allows us to know which bifurcations can occur in our problem. From now on, we need to distinguish between the two fixed points although

results for the second fixed point can be directly drawn from the analysis of the first one and symmetry considerations. We study the possible bifurcations in the space of parameters (μ_1, μ_2).

The nullclines of the system (3.30), i.e. $\dot{\xi} = 0$ and $\dot{\eta} = 0$, are

$$\eta = -d\xi^2 - \mu_1 \tag{3.31}$$

$$\eta = 0 \tag{3.32}$$

$$\mu_2 - d\xi = 0. \tag{3.33}$$

The different intersections of these nullclines will determine the fixed points.

Fixed point at (-1,0) We recall that, in this case, we can write $d = \frac{1+2\cosh(b)}{1+\cosh(b)} > 1$.

First Case : if $\mu_1 < 0$, from (3.31) and (3.32) we have two fixed points A and B located at $(\sqrt{-\mu_1/d}, 0)$ and $(-\sqrt{-\mu_1/d}, 0)$, respectively. From (3.31) and (3.33), we have a third fixed point C located at $\xi = \mu_2/d$ and $\eta = -\mu_2^2/d - \mu_1$. The eigenvalues for the three fixed points are

- Point A :

$$\lambda_1 = 2d\sqrt{\frac{-\mu_1}{d}} > 0 \tag{3.34}$$

$$\lambda_2 = \mu_2 - d\sqrt{\frac{-\mu_1}{d}} \tag{3.35}$$

Point A is a saddle point or a source if $\mu_2 > \sqrt{-\mu_1 d}$.

- Point B :

$$\lambda_1 = -2d\sqrt{\frac{-\mu_1}{d}} < 0 \tag{3.36}$$

$$\lambda_2 = \mu_2 + d\sqrt{\frac{-\mu_1}{d}} \tag{3.37}$$

Point B is a saddle point or a sink if $\mu_2 < -\sqrt{-\mu_1 d}$.

- Point C :

$$\lambda_1 = \mu_2 - \sqrt{2\mu_2^2 + \mu_1 d} \tag{3.38}$$

$$\lambda_2 = \mu_2 + \sqrt{2\mu_2^2 + \mu_1 d} \tag{3.39}$$

- $\mu_2 < 0$
  $-2\mu_2^2/d < \mu_1 < 0$, Saddle point
  $\mu_1 < -2\mu_2^2/d < 0$, Stable Focus
- $\mu_2 = 0$, Center
- $\mu_2 > 0$
  $-2\mu_2^2/d < \mu_1 < 0$, Saddle point
  $\mu_1 < -2\mu_2^2/d < 0$, Unstable Focus

Second Case : if $\mu_1 > 0$, from (3.31) and (3.33), we only have one fixed point, which is a saddle point. In (3.2), we give the complete bifurcation diagram in the parameter space (μ_1, μ_2). The bifurcation we have in our system is the merging of two saddle points with an elliptic point, i.e. a branch $\mu_2 = 0$ starting with $\mu_1 < 0$ and increasing it to get a degenerate fixed point.

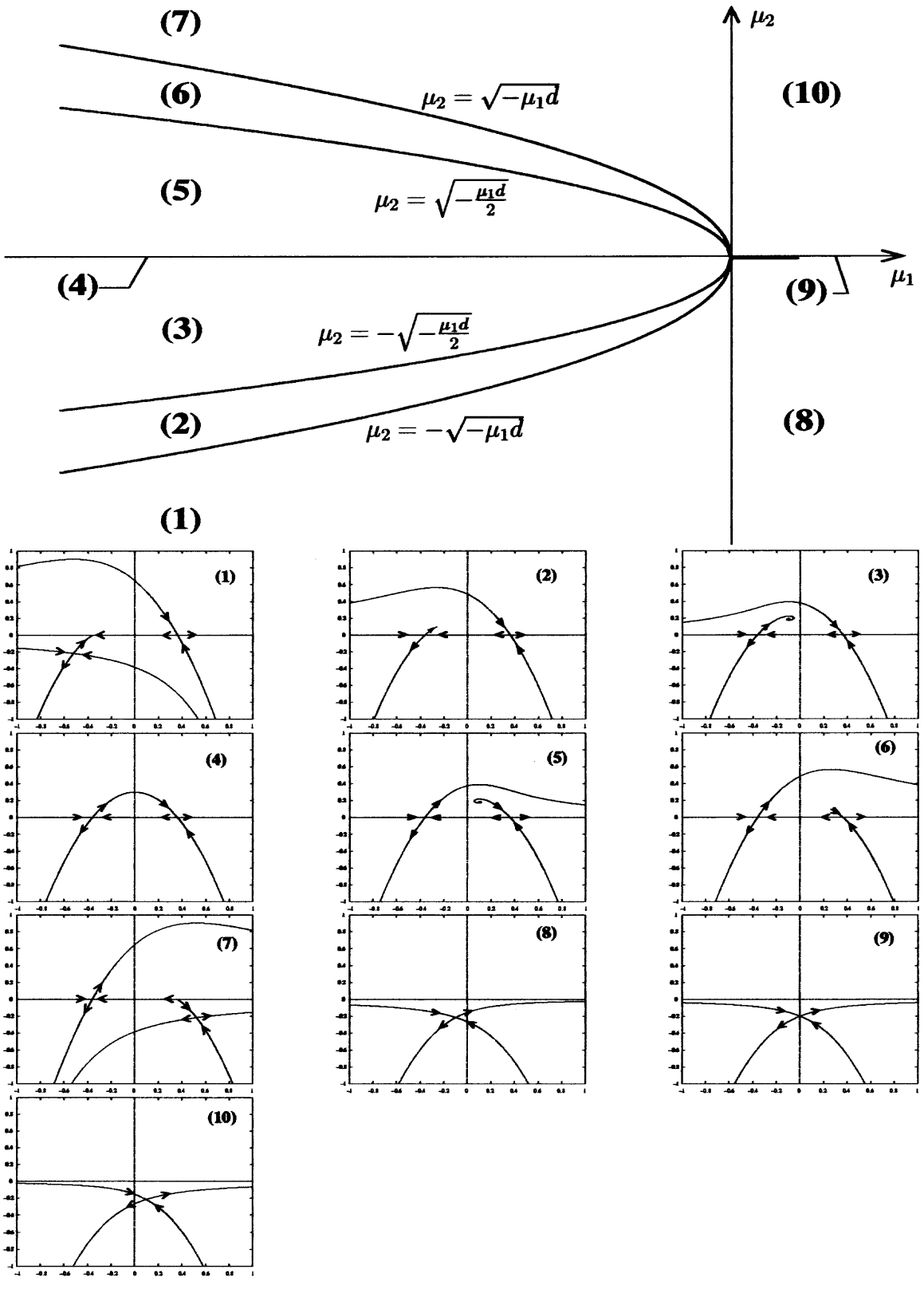

Figure 3.2 Bifurcation diagram for the normal form (3.30) at the degenerate fixed point (-1,0).

Fixed point at (+1,0) We recall that, in this case, we have $d = \frac{1-2\cosh(b)}{2\cosh^2(\frac{b}{2}))} < 0$.

First Case : if $\mu_1 < 0$, from (3.32) and (3.33), we have only one saddle fixed point located at $\xi = \mu_2/d$ and $\eta = -\mu_2/d - \mu_1$.

Second Case : if $\mu_1 > 0$

we have two fixed points A and B located at $\mu_1 = \sqrt{-\mu_1/d}$ and $\mu_1 = -\sqrt{-\mu_1/d}$, respectively. From (3.31) and (3.33), we have a third fixed point C located at $\xi = \mu_2/d$ and $\eta = -\mu_2^2/d - \mu_1$. Eigenvalues for the three fixed points:

- Point A:

$$\lambda_1 = 2d\sqrt{\frac{-\mu_1}{d}} < 0 \tag{3.40}$$

$$\lambda_2 = \mu_2 - d\sqrt{\frac{-\mu_1}{d}} \tag{3.41}$$

Point A is a saddle point or a sink if $\mu_2 < \sqrt{-\mu_1 d}$.

- Point B:

$$\lambda_1 = -2d\sqrt{\frac{-\mu_1}{d}} > 0 \tag{3.42}$$

$$\lambda_2 = \mu_2 + d\sqrt{\frac{-\mu_1}{d}} \tag{3.43}$$

Point B is a saddle point or a source if $\mu_2 > \sqrt{-\mu_1 d}$.

- Point C:

$$\lambda_1 = \mu_2 - \sqrt{2\mu_2^2 + \mu_1 d} \tag{3.44}$$

$$\lambda_2 = \mu_2 + \sqrt{2\mu_2^2 + \mu_1 d} \tag{3.45}$$

. $\mu_2 < 0$
  $-2\mu_2^2/d < \mu_1 < 0$, Saddle point
  $\mu_1 < -2\mu_2^2/d < 0$, Stable Focus
. $\mu_2 = 0$, center
. $\mu_2 > 0$
  $-2\mu_2^2/d < \mu_1 < 0$, Saddle point
  $\mu_1 < -2\mu_2^2/d < 0$, Unstable Focus

Figure (3.3) gives the complete bifurcation diagram in the parameter space (μ_1, μ_2).

The bifurcation we have in our system is the merging of two saddle points with an elliptic point, i.e. branch $\mu_2 = 0$, starting with $\mu_1 < 0$ and increasing it to get a degenerate fixed point.

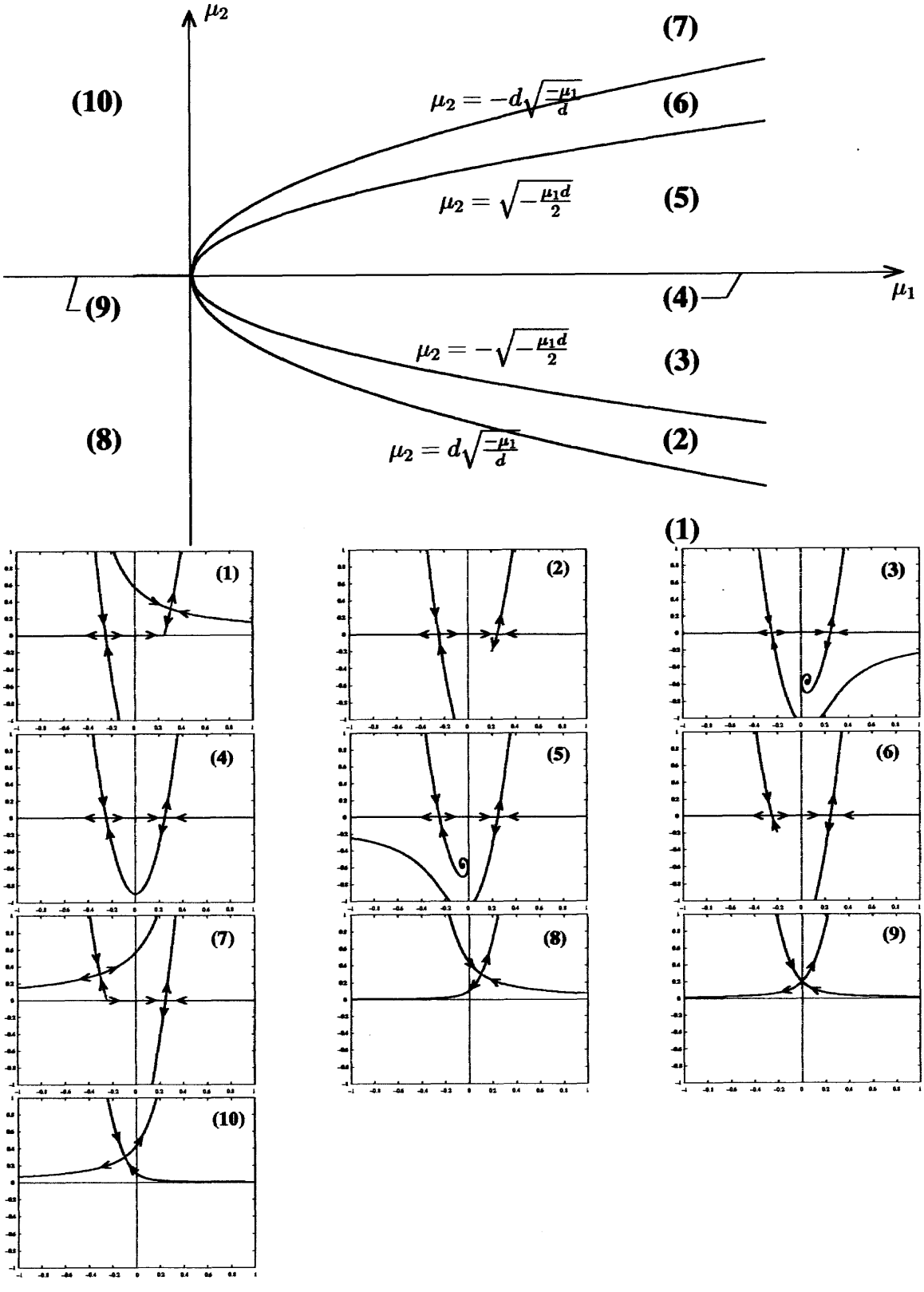

Figure 3.3 Bifurcation diagram for the normal form (3.30) at the degenerate fixed point (+1,0).

3.3.2 Degenerate Fixed Point Inside the Container

Finally, we have a degenerate case at $X^* = X_c^*$ for the particular parameter value $\beta = \beta_c$. This fixed point has the following Jacobian matrix

$$J_c = \begin{pmatrix} 0 & 2 \\ 0 & 0 \end{pmatrix} \tag{3.46}$$

In order to understand the dynamics around the latter fixed point $X^* = X_c^*$, we introduce two new variables (u, v) with $u = X - X_c^*$, $v = y$ and a new time $t' = 2t$.

A degenerate fixed point at $(X_c, 0)$ occurs for some particular value of β. More precisely, we can write

$$X_c = \frac{2\cosh(b) - \sqrt{-1 + 2\cosh(2b)}}{3} \tag{3.47}$$

$$\beta_c = -\frac{\sinh(b)}{X_c(1 + X_c^2 - 2\cosh(b)X_c)}. \tag{3.48}$$

The quadratic order of the Taylor expansion reads

$$f_2 = \begin{pmatrix} ((-2 + \cosh(2b))\sqrt{-1 + 2\cosh(2b)} + \cosh(3b))\frac{uv}{\sinh^2(b)} \\ (-(-2 + \cosh(2b))\sqrt{-1 + 2\cosh(2b)} - \cosh(3b))\frac{u^2+v^2}{2\sinh^2(b)} \end{pmatrix}. \tag{3.49}$$

To simplify the formulas, we define d as

$$d = \frac{(-2 + \cosh(2b))\sqrt{-1 + 2\cosh(2b)} + \cosh(3b)}{2\sinh^2(b)} > 0 \quad , b \in [0, \infty). \tag{3.50}$$

It follows that

$$f_2 = \begin{pmatrix} 2duv \\ -d(u^2 + v^2) \end{pmatrix}. \tag{3.51}$$

The resonant term (Guckenheimer and Holmes [15]) is

$$f_2^R = \begin{pmatrix} 0 \\ -du^2 \end{pmatrix} \tag{3.52}$$

and the normal form at the order $O(u^3)$ is given by :

$$\dot{u} = v \tag{3.53}$$

$$\dot{v} = -du^2. \tag{3.54}$$

The description of the different bifurcations that can occur is now achieved by using the generic unfolding (see Appendix B.2) :

$$\begin{aligned} \dot{u} &= v \\ \dot{v} &= \mu_1 + \mu_2 v - du^2. \end{aligned} \tag{3.55}$$

From this new system, we have two fixed points for $v = 0$, located at

$$u_1 = \sqrt{\frac{\mu_1}{d}} \tag{3.56}$$

$$u_2 = -\sqrt{\frac{\mu_1}{d}}. \tag{3.57}$$

We consider $\mu_1 > 0$ to restrict ourselves to the case of a real solution. Our new Jacobian is given by

$$J = \begin{pmatrix} 0 & 1 \\ -2du_{1,2} & \mu_2 \end{pmatrix}. \tag{3.58}$$

At $(u_1, 0)$, the eigenvalues can be written as

$$\lambda_1^{\pm} = \frac{1}{2}\left(\mu_2 \pm \sqrt{-8\sqrt{\mu_1 d} + \mu_2^2}\right). \tag{3.59}$$

The eigenvalue can be imaginary if $\mu_2^2 \leq 8\sqrt{\mu_1 d}$ and the fixed point will be a stable (unstable) focus for $\mu_2 < 0$ ($\mu_2 > 0$). At $(u_2, 0)$, the eigenvalues are

$$\lambda_2^{\pm} = \frac{1}{2}\left(\mu_2 \pm \sqrt{8\sqrt{\mu_1 d} + \mu_2^2}\right). \tag{3.60}$$

In this case, $\lambda_2^{\pm}$ is real for $\lambda_2^{+} > 0$ and $\lambda_2^{-} < 0$. Consequently $(u_2, 0)$ will always be a saddle point.

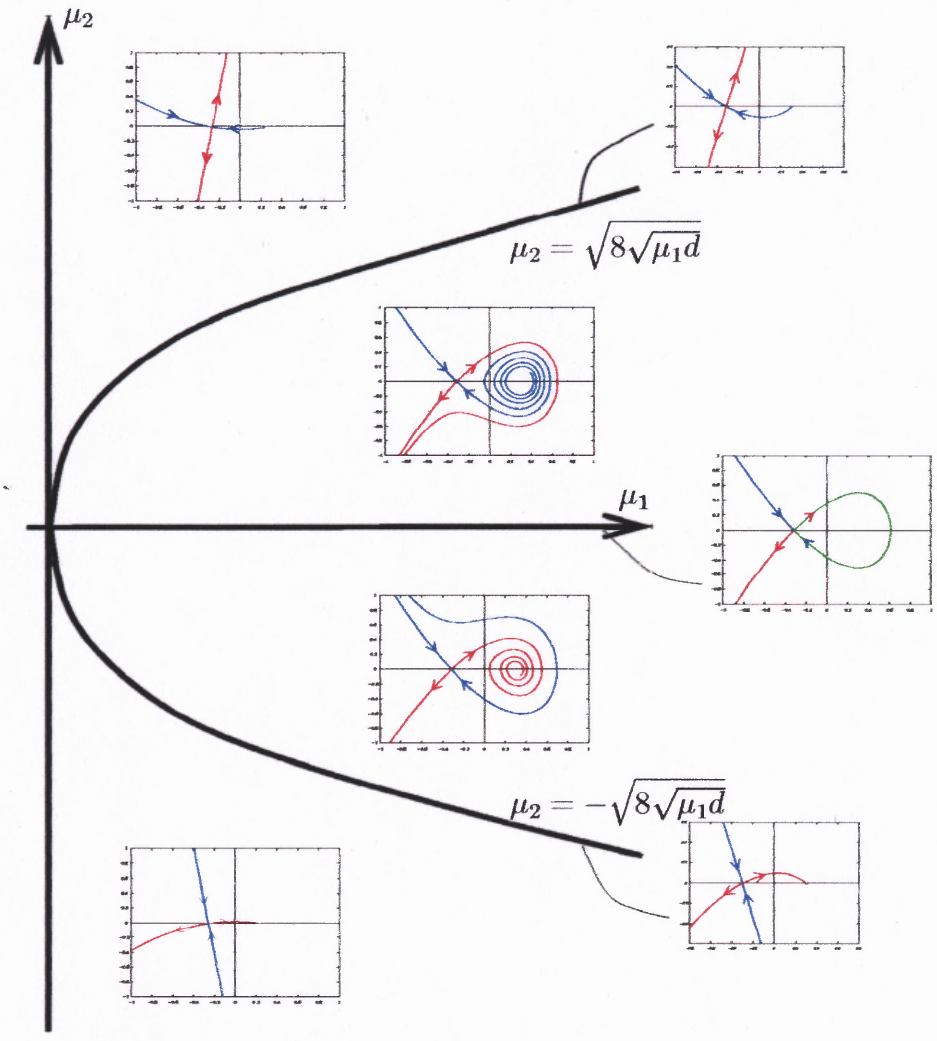

Figure 3.4 Bifurcation diagram for the normal form (3.55).

Due to the fact that our system is Hamiltonian, we cannot have stable (or unstable) foci, sinks or sources. It follows that we end up with only the branch $\mu_1 > 0$ and $\mu_2 = 0$, corresponding to a saddle loop-node bifurcation.

3.4 Bifurcation Diagram for a Uniformly Rotating Vortex

We now describe the dynamics in the four different regions of the phase space, which we refer to regions I-IV, respectively. The different figures are given for a positive Γ, i.e. a counterclockwise circulation. For $\Gamma < 0$, we have the same structure but the direction of the flow is reversed.

We start from Region I and decrease the parameter β, going through all the dynamics of the various regions and the bifurcations occurring in between two different regions.

Region I, defined by $\beta > \beta_{+1}$ (see Figure (3.5)), contains two fixed points, an elliptic point and a saddle point in the interior of the fluid domain. The saddle point has a one-dimensional stable manifold and a one-dimensional unstable manifold. A homoclinic orbit consisting of a small loop around the vortex and a large loop quasi-parallel to the boundary is connected to the saddle point. Small periodic orbits surround the vortex while large periodic orbits surround the elliptic point, located in between the boundary and the large loop. The fluid domain is divided into three sub-regions. As β decreases, the saddle point approaches the boundary, and the small

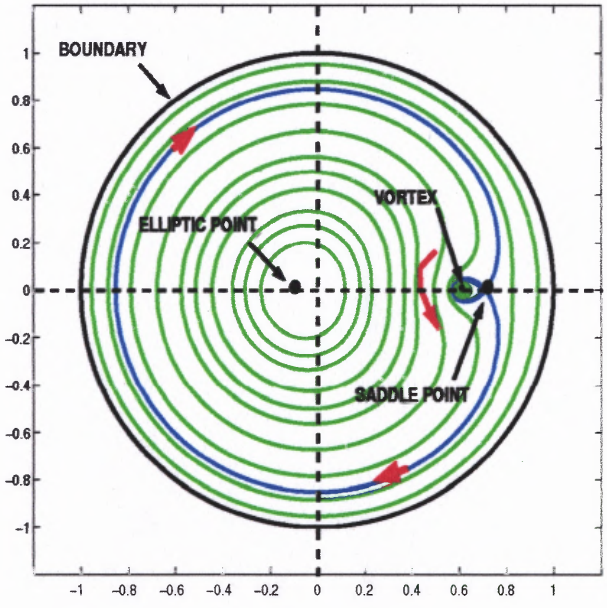

Figure 3.5 Phase space dynamics in REGION I.

loop of the homoclinic orbit becomes larger while the large loop moves closer to the circular boundary of the domain.

When β reaches the particular value $\beta = \beta_{+1}$ (see Figure (3.6)), the saddle point becomes degenerate, located on the boundary at $X = 1, Y = 0$, and the large loop of the homoclinic orbit coincides with the boundary.

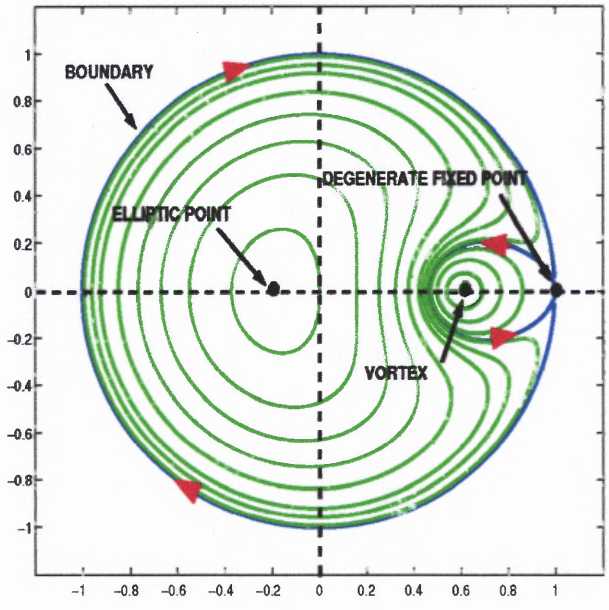

Figure 3.6 Phase space for transition from REGION I to REGION II.

As β decreases, such that $\beta_{-1} < \beta < \beta_{+1}$ (see Figure (3.7)), the degenerate fixed point splits into two saddle points, which start moving away from the location $X = 1, Y = 0$ in opposite directions as β varies, while remaining on the boundary, symmetrically located with respect to the horizontal axis $Y = 0$. The saddle points have a one-dimensional unstable manifold and a one-dimensional stable manifold. In this region, the fluid domain is divided into two subdomains separated by an interior separatrix. This is an interesting phenomenon which looks quite promising for improving fluid mixing in the vicinity of the boundary. Meanwhile, the elliptic point is pushed to the left by the heteroclinic orbit.

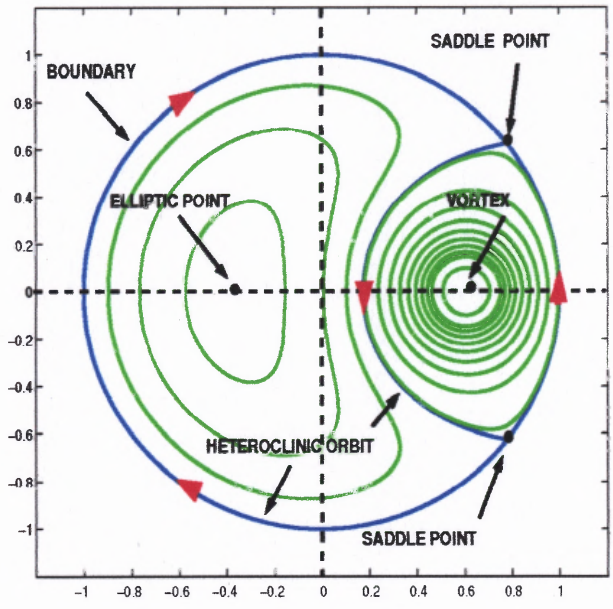

Figure 3.7 Phase space dynamics in REGION II.

When β reaches the value $\beta = \beta_{-1}$ (see Figure (3.8)), the two saddle points and the elliptic point meet each other at the location $(X = -1, Y = 0)$ to become a single degenerate fixed point.

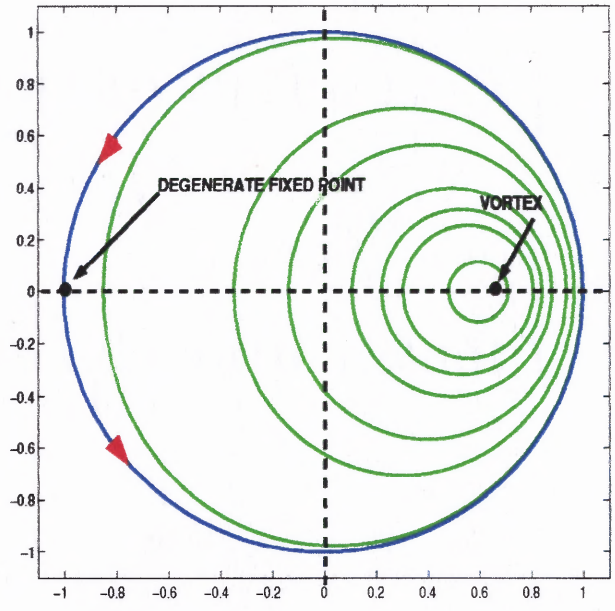

Figure 3.8 Phase space for the transition REGION II-REGION III.

The boundary is now a homoclinic cycle and the streamlines are periodic orbits around

the vortex. The fluid domain is no longer divided into two regions. When β is smaller than β_{-1} but remains larger than β_c (see Figure (3.9)), the saddle point on the boundary has disappeared and all streamlines, including the boundary, are periodic orbits encircling the vortex. When β takes the value $\beta = \beta_c$ (see Figure (3.10)),

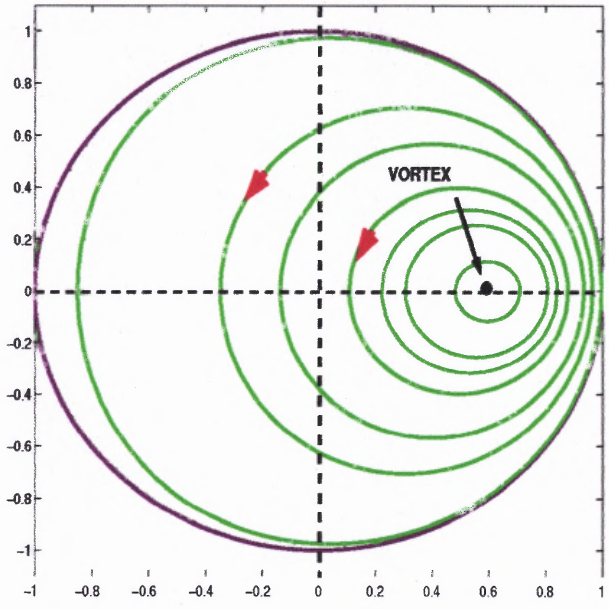

Figure 3.9 Phase space dynamics in REGION III.

a degenerate fixed point located at $(X_c^*, 0)$ appears. A homoclinic orbit connected to the fixed point separates the fluid into two regions in the vicinity of the vortex located inside the homoclinic orbit, and the remainder of the domain. Finally, when $\beta < \beta_c$ (see Figure (3.11)), an elliptic fixed point appears and the saddle point loses its degeneracy (Takens-Bogdanov bifurcation, Node-Saddle loop), so that its stable and unstable manifolds are now two-dimensional, leading to a classical figure eight homoclinic cycle. The fluid domain is then divided into three regions; two regions are located within the two loops of the homoclinic cycle, and a region outside.

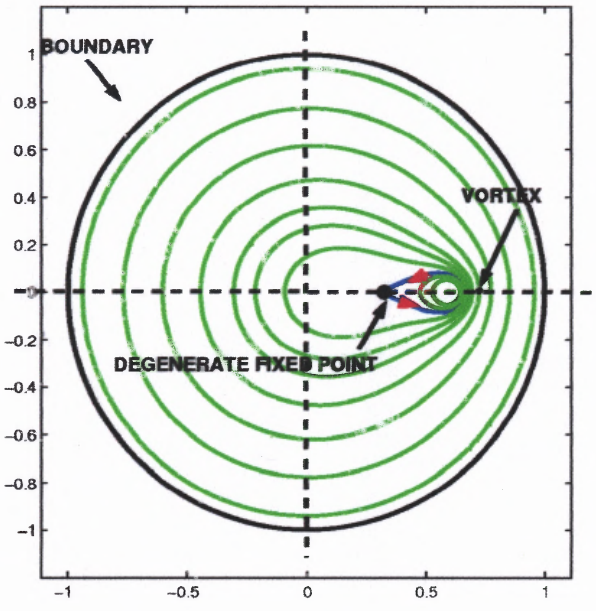

Figure 3.10 Phase space for transition REGION III-REGION IV.

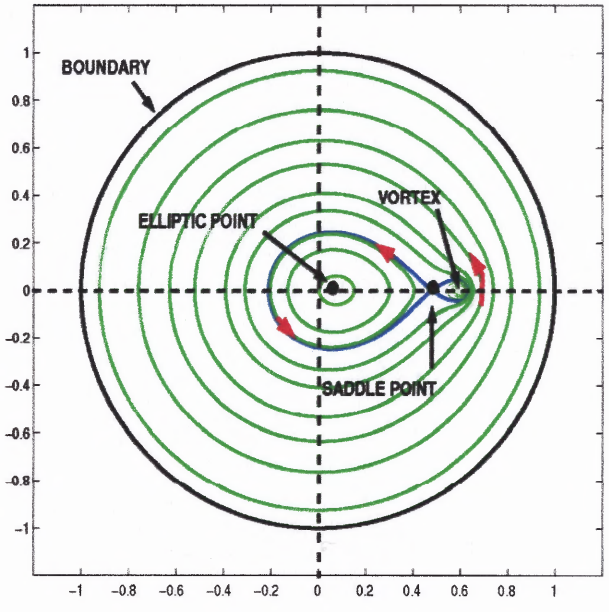

Figure 3.11 Phase space dynamics in REGION IV.

It is interesting to notice that a fixed point in $\mathcal{R}_v$ corresponds in $\mathcal{R}$ to a circular streamline centered at the origin with a period identical to that of the vortex $T_v = 2\pi/\omega$. Let us consider a closed streamline in $\mathcal{R}_v$ with period T.

In $\mathcal{R}$, we have

- If $T/T_v \in \mathbb{Q}$, then the streamline is closed in the region Ω
- If $T/T_v \notin \mathbb{Q}$, then the streamline is dense in some region Ω

where $\mathbb{Q}$ is the set of rational numbers and Ω, the region defined by $\{z; \forall t,\ d_{min} < |z(t)| < d_{max}\}$, (see Figure (3.12)) with

$$d_{min} = \min_{t\in[0,T]} |z(t)| \quad \& \quad d_{max} = \max_{t\in[0,T]} |z(t)| \tag{3.61}$$

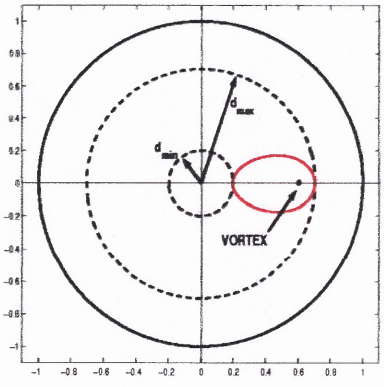

Figure 3.12 Frame of reference of the vortex $\mathcal{R}_v$.

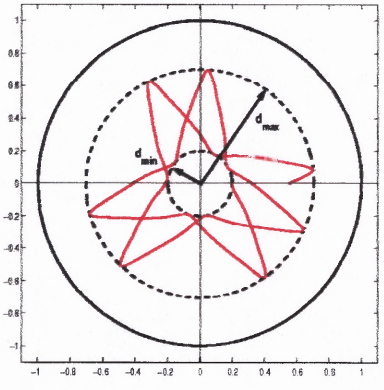

Figure 3.13 Fixed frame of reference $\mathcal{R}$.

CHAPTER 4

NUMERICAL SIMULATION

In order to illustrate the mixing and its enhancement by a dual speed rotating vortex, we numerically integrate the nonlinear system (2.36)-(2.37) by using the software *Matlab* [29]. A Runge-Kutta numerical scheme is used to integrate the Hamiltonian equations. We first check the accuracy of the numerical scheme by checking the invariant or constant of motion for different initial conditions, and also by comparing the theoretical eigenvalues of saddle points in our system with those obtained numerically. We then give a numerical simulation of the mixing with a dual speed vortex.

4.1 Vortex Rotating at Uniform Speed

The numerical scheme adopted here is the Runge-Kutta method using 7th order formulas, with an order $O(h^8)$ accuracy due to a local interpolation. This is not implemented by default in *Matlab*, but can be found for example in reference [49]. The function implemented by default, 4th order Runge-Kutta (ODE45), is not used because it lacks the necessary accuracy for some invariants. We would also like to point out that the Runge-Kutta scheme is not a symplectic integrator and consequently it does not preserve the symplectic structure (volume preserving) of the phase space, which may cause problems for very long time simulations. However, for the different simulations presented in this chapter, the 8th order Runge-Kutta was sufficiently accurate for the running time considered.

We recall that the Hamiltonian, $H(X, Y, \tau, F)$, is always a constant of motion. Consequently, we can check the accuracy of our numerical scheme by comparing the Hamiltonian along the trajectory computed numerically and its theoretical value, which is determined by the initial condition solely. From theoretical considerations, we know that for a constant angular speed the four-dimensional phase space is actually

comprised of two independent subspaces. The Hamiltonian is independent of τ, and we take $F = cst = 0$ for convenience. We thus have along a trajectory:

$$H(X,Y) = -\frac{\Gamma}{2\pi}\log\left(\frac{(X-e^{-b})^2+Y^2}{(X-e^{b})^2+Y^2}\right) + \frac{\omega}{2}(X^2+Y^2) = H(X_{init},Y_{init}). \quad (4.1)$$

We define the maximum of the relative error as

$$error = \max_{\text{along trajectory}}\left|\frac{H(X,Y)-H(X_{init},Y_{init})}{H(X_{init},Y_{init})}\right| \quad (4.2)$$

and take the initial condition on the X-axis $[-1:+1]$ with a spatial step $dx = 0.1$. Avoiding the neighborhood of the vortex (since the vortex is a singular point), that is $(e^{-b}-dx, e^{-b}+dx)$), we compute the error for the different regions of the bifurcation diagram versus the initial condition on the X-axis (see Figure (4.1)). The maximum of the relative error is found to be about 10^{-11}.

4.2 Stability of the Fixed Points

To check numerically the stability of the hyperbolic fixed points, or eigenvalue along the stable or unstable manifold, we use the following standard approach. We integrate numerically (2.36) - (2.37), starting with an initial condition in a neighborhood of a saddle point Z^*, and plot the distance $d(t) = |Z(t) - Z^*|$ versus time on a semilog scale (Figure (4.2)). For a saddle point, we expect the distance to behave like $\xi_0 e^{\lambda t}$ where ξ_0 is the initial perturbation, i.e. $|\xi_0| = 10^{-12}$ and λ denotes the positive (negative) eigenvalue along the unstable (stable) eigenspace. The perturbation was found numerically to grow exponentially, with exponents very close to the eigenvalues given by the relation (3.19). We perform a curve fitting on the semilog plot for small $d(t)$ numerical values, typically $10^{-9} < d(t) < 10^{-6}$; the slope of the fitting curve gives us the numerical eigenvalue of the saddle point. For $\beta \in [-8,8]$, we present the error in the eigenvalue of the saddle points for the regions I,II,IV (Figure (4.3)).

The numerical results are in good agreement (error of the order 10^{-5}) with the theoretical predictions (3.17).

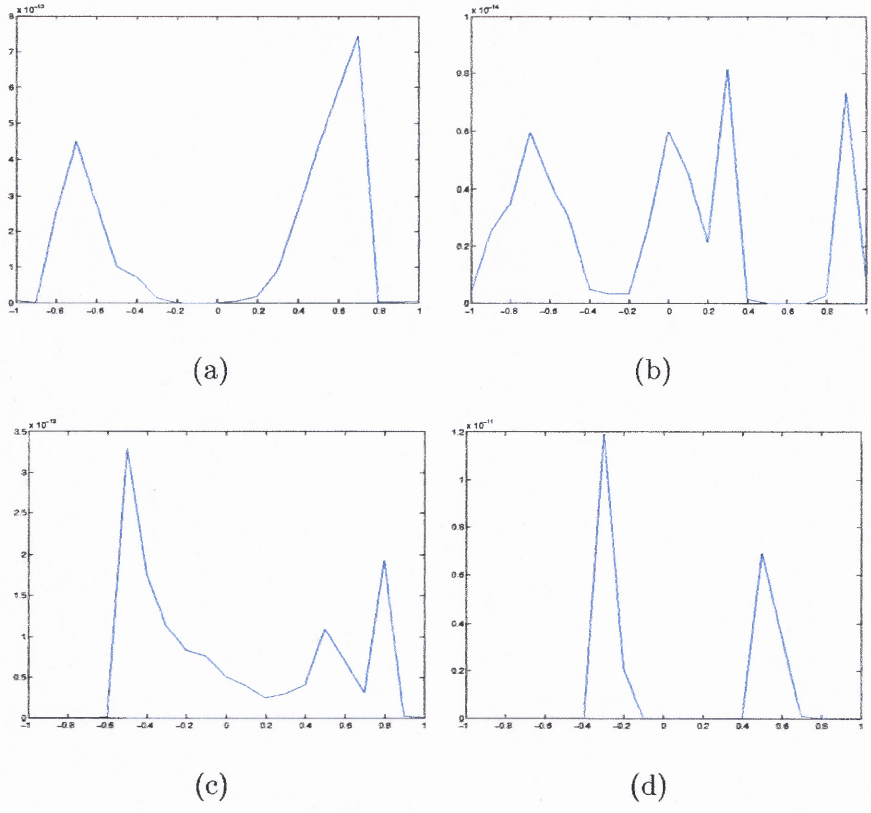

Figure 4.1 Relative error of the Hamiltonian along numerical trajectories versus initial condition on the X-axis for the regions I, II, III, IV (resp. (a), (b), (c), (d))

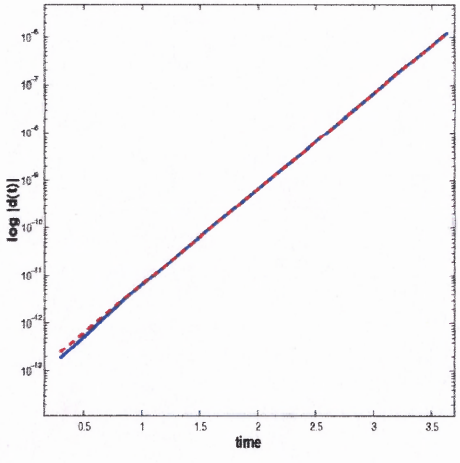

Figure 4.2 dashed line fitting curve, solid line numerical data

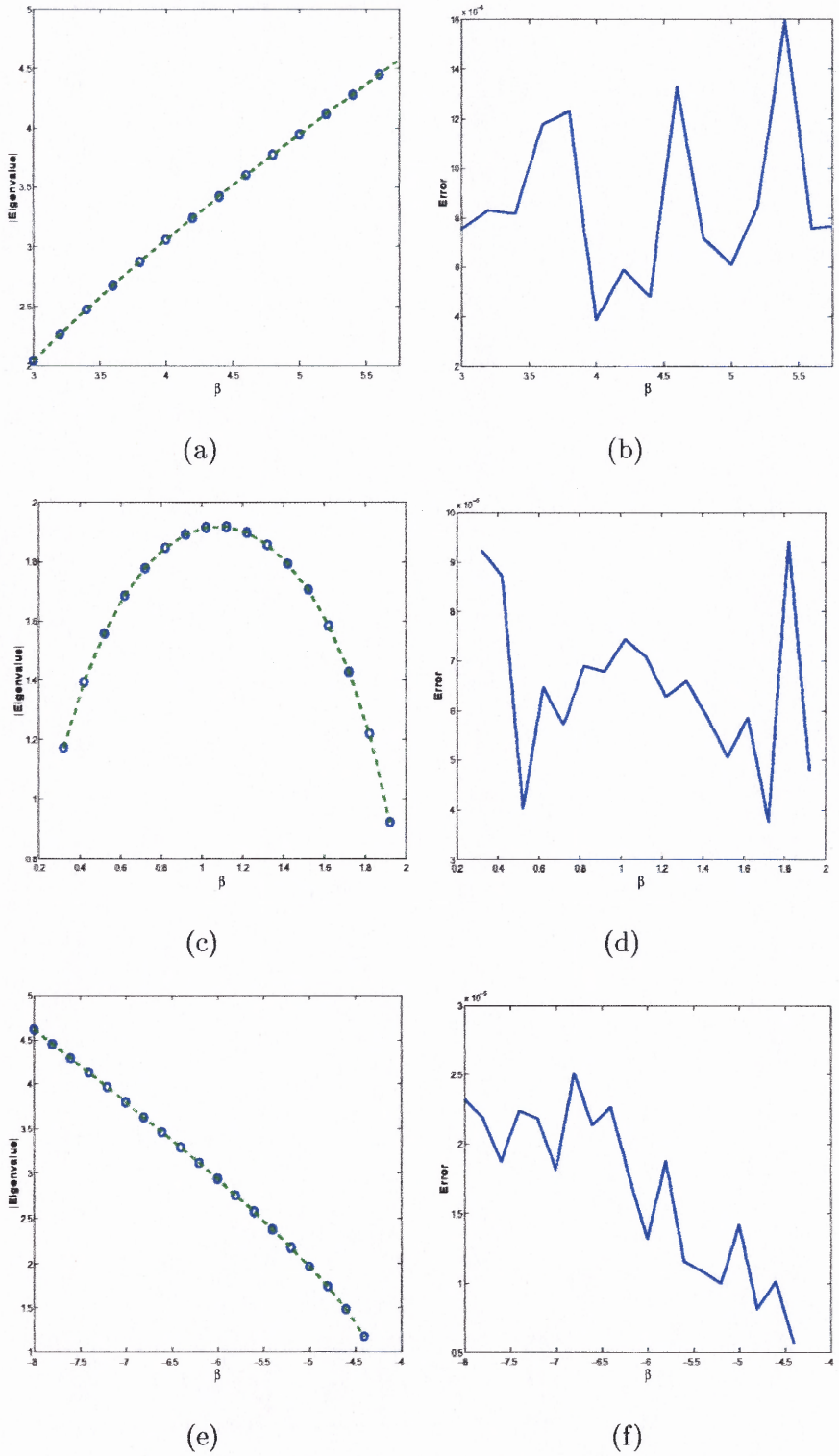

Figure 4.3 (a), (c), (e) "o" Numerical value, "−−" Theoretical value of the eigenvalues of the saddle point for Regions I, II, IV respectively. (b), (d), (f) Numerical Error for Regions I, II, IV, respectively

We now address following up the stable and unstable manifolds of the saddle points. The latter, connected through homoclinic (heteroclinic) orbits, are computed from the Hamiltonian itself. That is, for each position Z_s^* of the saddle point, we compute the value of the Hamiltonian and plot the corresponding level curves, including the homoclinic (heteroclinic) orbit.

Figure (4.4) displays the result of a numerical simulation in Region II showing the evolution of an initial blob containing about 2000 points. One can clearly observe that the blob stretches, forming a spiral between two specific streamlines. The blob cannot spread everywhere within the container, particularly beyond the two streamlines. This phenomenon, leading to poor mixing, takes place in all the regions of the phase space.

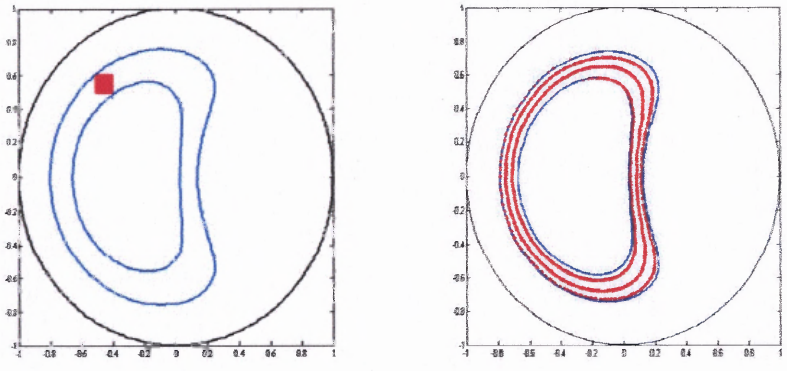

(a) (b)

Figure 4.4 Evolution in time of a blob.

Consequently, a single speed rotating vortex creates a stretch but not a folding of the material lines. In this case, the spreading, limited by the structure of the flow itself and the initial condition, remains confined in between streamlines of the flow.

CHAPTER 5

DUAL SPEED VORTEX AND CHAOS

H. Aref [1] introduced a vortex jumping back and forth between two fixed positions in a circular container and proved the existence of a chaotic regime for the dynamics. We now replace the space discontinuity in [1] by a discontinuity in time in the rotational velocity of the vortex in the container. Notice that changing the spinning speed of the vortex would have the same effect in terms of the dimensionless parameter $\beta = \frac{\omega\pi}{\Gamma}$.

5.1 Dual Speed Rotating Vortex

We thus introduce a dual speed rotating vortex by switching periodically the angular velocity (see Figure(5.1)).

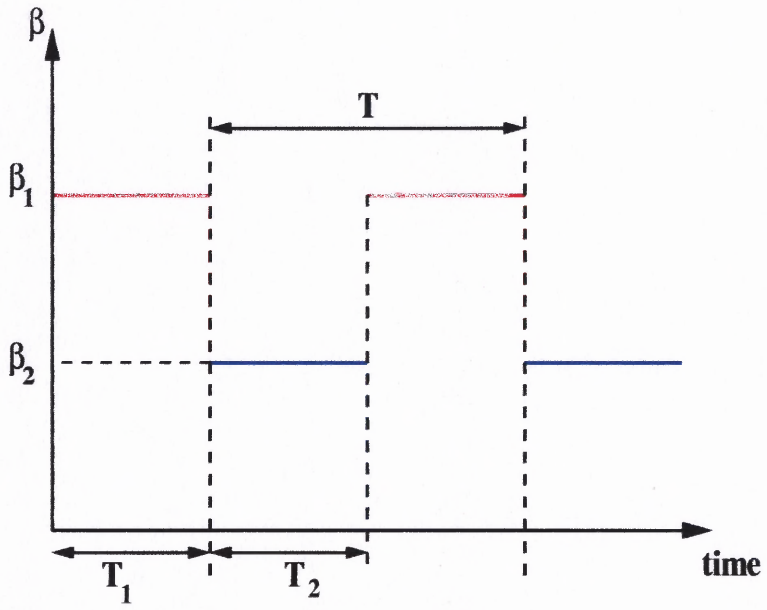

Figure 5.1 Dual Speed

In terms of the dynamics, we seek to create chaotic dynamics by using two different parameters (β_1, β_2), which may result in two sets of transverse streamlines. For example, we create an alternative clockwise and counterclockwise vortex motion at the same or different speeds, or alternate slow speeds and high speeds in the same

angular direction in a periodic fashion.

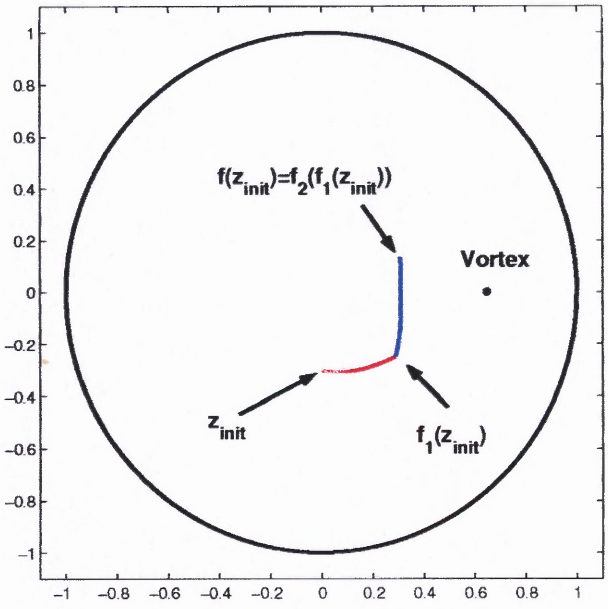

Figure 5.2 Schematic of the mapping f for a dual speed rotating vortex

From Figure (5.2), we can see that by considering two sets of transverse streamlines, the trajectory of a passive particle will experience a significant change in direction, a "90 degrees" turn, and the smoothness of the trajectory will be typically $\mathcal{C}^1$. We observe that the dynamics of the fluid generated by a dual speed rotating vortex can be described as the composition of two mappings, f_1 and f_2, corresponding to (β_1, T_1) and (β_2, T_2), respectively. The resulting mapping can thus be written as $f = f_2 \circ f_1$. In the next section, we will construct explicitly an invariant set of the mapping f. From a dynamical viewpoint, it seems promising to take two speeds from two distinct regions of the dynamics out of the four regions previously described. For this purpose, Region II seems particularly interesting as it presents an opportunity to increase fluid mixing close to the boundary due to the heteroclinic orbit coinciding with the boundary of the domain. This orbit connecting one point on the contour to its symmetric image on the opposite side of the boundary in a direction transverse to the contour allows us to exchange fluid close to the boundary with fluid inside the

container, relatively far away from the boundary. It is expected that such an exchange will facilitate mixing.

5.2 Numerical Simulation of the Dual Speed

We now consider the dual speed vortex with the following parameters:

$$\beta_1 = -5\,,\; T_1 = 1 \tag{5.1}$$

$$\beta_2 = 1\,,\; T_2 = 0.9. \tag{5.2}$$

The initial condition for the mixing problem is a marked square blob of fluid consisting of approximately 6000 points, all concentrated within a small area of size 1% of the container. The aim of our simulation is to study the spreading of the fluid blob after a certain number of periods nT.

Mixing is studied by imposing two different velocities of the vortex, as we previously described. Particularly, the parameter β_1 is chosen to be $\beta_1 = -5$, corresponding to the dynamics in Regions IV, and β_2 was given the value $\beta_2 = 1$, corresponding to the dynamics of region III. Notice that we chose $T_1 \neq T_2$ in order for the vortex to describe a full circular trajectory. That is, the vortex is going back and forth, although, on average, it is still rotating counter-clockwise. This example results in a quasi-uniform mixing inside the entire container, as shown in Figure (5.3).

One can clearly observe that mixing is due to the folding and stretching of the marked blob of fluid within the container. In particular, we notice that after a few iterations, some marked fluid reaches the vicinity of the boundary.

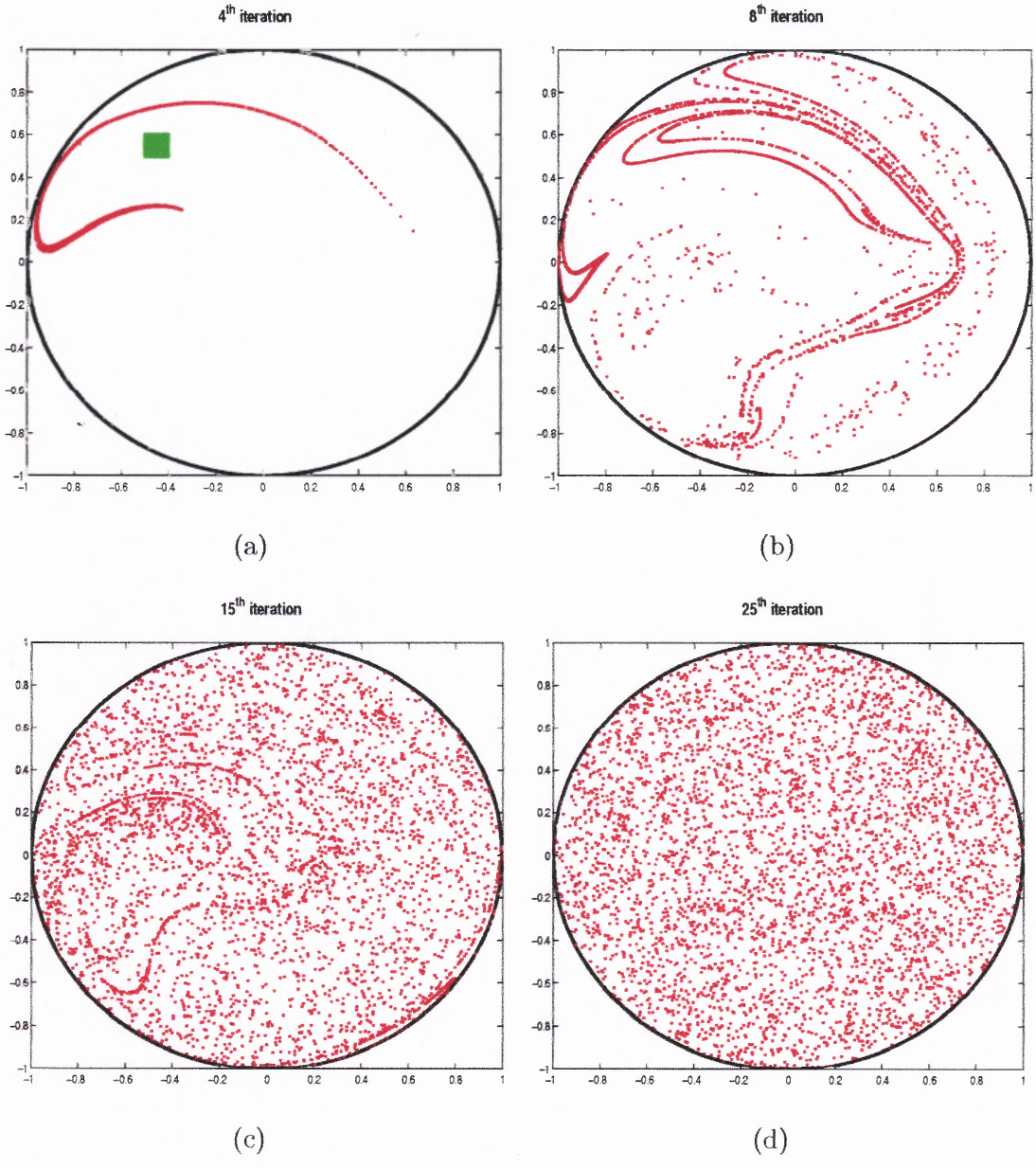

Figure 5.3 (a) Green: Initial Blob; Red: 4^{th} iterations; (b) 8^{th} iterations; (c) 15^{th} iterations; (d) 25^{th} iterations

5.3 Smale Horseshoe Construction

In order to show that chaotic advection is present in our system, we describe the construction of a Smale Horseshoe [15], [47] in the frame of reference of the vortex.

For this, we consider a small region, $\mathcal{D}_1$, in the container and seek its invariant points Λ, that is the set of points which, through the dynamics, return to this region

$\mathcal{D}_1$ after a certain number of iterations. It is well known that the existence of such a closed and compact set for which each of its points is an accumulation point, referred to as Cantor set or hyperbolic invariant set [15], [47] implies that the dynamics is chaotic, that is sensitive to the initial condition (see Appendix C).

In our search for a Cantor set, we first observe that the dynamics of the fluid generated by a dual speed rotating vortex can be described as the composition of two mappings, f_1 and f_2, corresponding to (β_1, T_1) and (β_2, T_2), respectively. The resulting mapping can thus be written as $f = f_2 \circ f_1$, with T being the difference between the two periods T_1 and T_2.

For any dynamics corresponding to a value β_i, the streamlines in the frame of reference of the vortex are closed. Each streamline has thus a period associated with it. Any initial marked blob of fluid in between two streamlines stretches into a spiral, while remaining confined within the space between the streamlines (see Figure (4.4)).

In order to construct the horseshoe, we choose an initial blob of fluid delimited by four streamlines, two streamlines whose periods are shifted by some time T_1, corresponding to a velocity parameter (β_1 and a period difference T_1), and two streamlines corresponding to (β_2, T_2) (see Figure (5.4)). The intersection of the two domains define two small regions $\mathcal{D}_1$ and $\mathcal{D}_2$. Notice that the four corners of $\mathcal{D}_1$ and $\mathcal{D}_2$ are fixed points for the mapping f.

We now follow the dynamics of one of these regions, $\mathcal{D}_1$. For this, we consider the image of $\mathcal{D}_1$ by f_1; as previously discussed, this image is a spiral between the first set of streamlines. In search of the invariant hyperbolic set, we retain the intersection of this spiral with $\mathcal{D}_1$ and $\mathcal{D}_2$ only and define $S_1 = f_1(\mathcal{D}_1) \cap \mathcal{D}_1$ and $S_2 = f_1(\mathcal{D}_1) \cap \mathcal{D}_2$, as shown in Figure (5.5).

The next step consists in applying the mapping f_2 to S_1 and S_2 and, once again, we retain the intersection with $\mathcal{D}_1$, see Figure (5.6). At this point, it is easy to realize

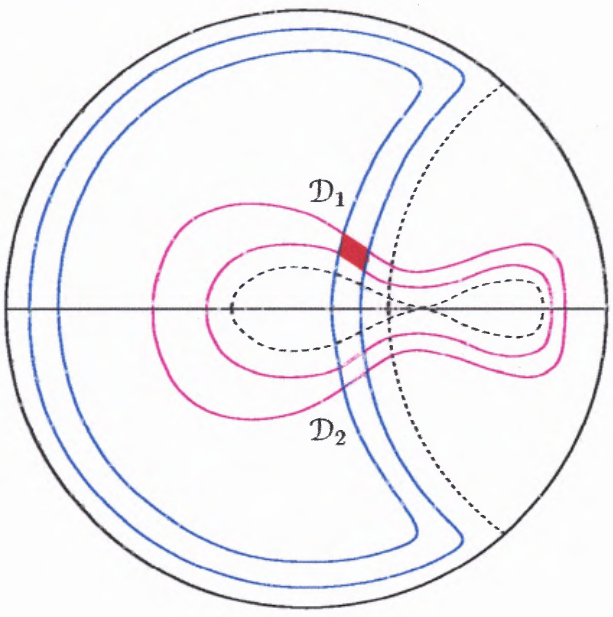

Figure 5.4 Initial domain $\mathcal{D}_1$ for the construction of the horseshoe

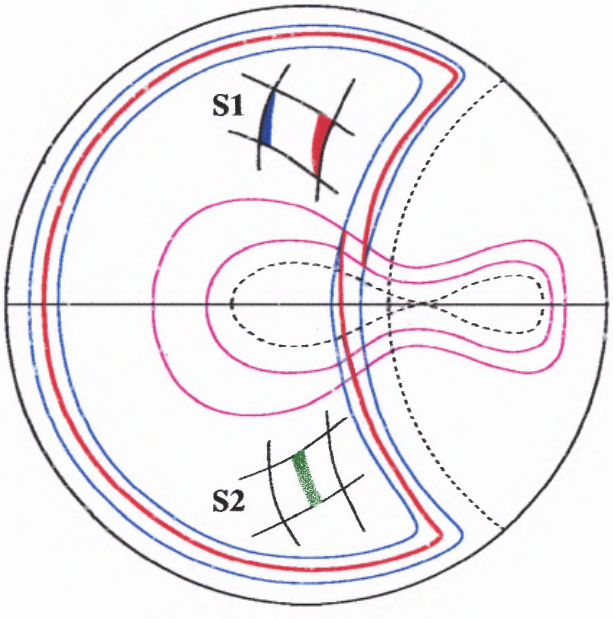

Figure 5.5 $S_1 = f_1(\mathcal{D}_1) \cap \mathcal{D}_1$ and $S_2 = f_1(\mathcal{D}_1) \cap \mathcal{D}_2$

the importance of $\mathcal{D}_2$ in the construction of the invariant set since some of its points return to $\mathcal{D}_1$.

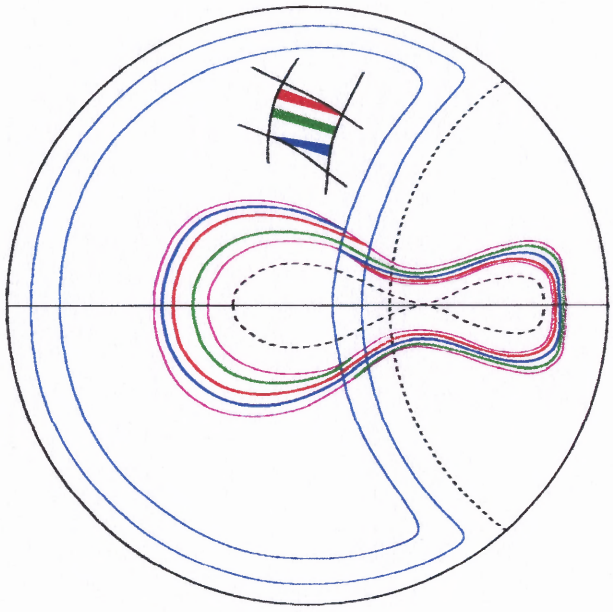

Figure 5.6 $\mathcal{D}_1 \cap f(\mathcal{D}_1)$

The domain $\mathcal{D}_1 \cap f(\mathcal{D}_1)$ consists of three stripes. It is clear that the next iteration $\mathcal{D}_1 \cap f(\mathcal{D}_1) \cap f^2(\mathcal{D}_1)$ of this procedure will lead to seven stripes (see Figure (5.7)).

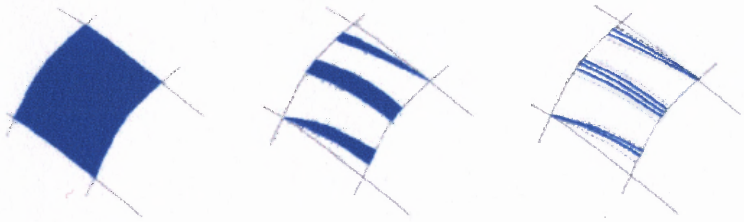

Figure 5.7 2 first steps (forward) of the construction of the horseshoe

Iterations backward in time will lead to stripes transverse to the ones we just described and a repetition of the iterations will generate the Cantor set within $\mathcal{D}_1$.

5.4 Islands Chains and Chaotic Layer

As in other works where mixing is achieved by means of chaotic advection [1], it is also possible to find some dynamics where the marked blob of fluid does not spread

everywhere in the container, thus leaving unreachable islands or invariant regions in the flow [8],[22]. For example, we now consider the dynamics corresponding to the values $\beta_1 = -6, \beta_2 = 2, T_1 = T_2 = 0.3$ and take a snapshot of the location of the marked fluid blob after each period T; this is equivalent to taking a Poincaré section in phase space. We can observe in Figure (5.8) the appearance of islands after 10,000 iterations, which clearly reduces the mixing efficiency. Both the size and the number of these islands depend on the particular parameter values. A systematic numerical parameter study to investigate this dependency would be a tedious exercise and is not included in this paper. In Figure(5.8), we can see the transient chaotic region-regular island. This example has a periodic point of period three inside the island and on the boundary as well. A magnification of the transient region, called the stochastic layer or Arnold's web [26] is given in Figure (5.9).

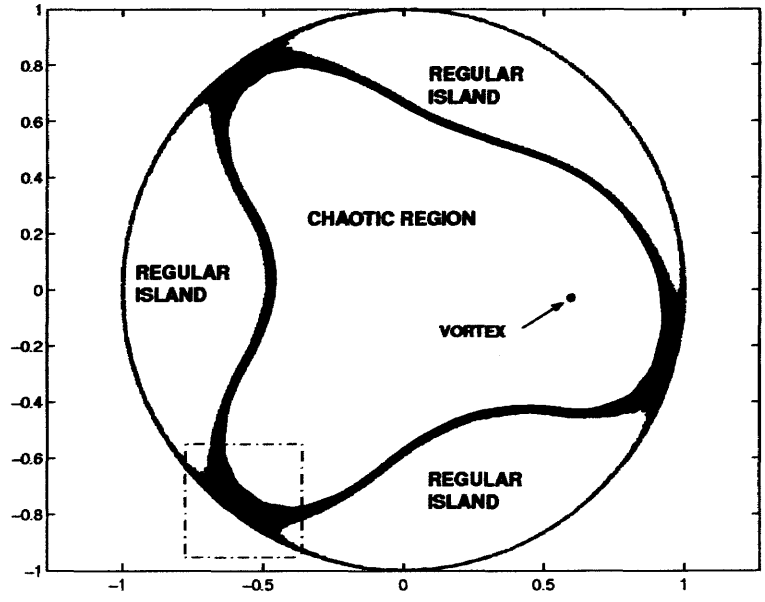

Figure 5.8 Stochastic layer

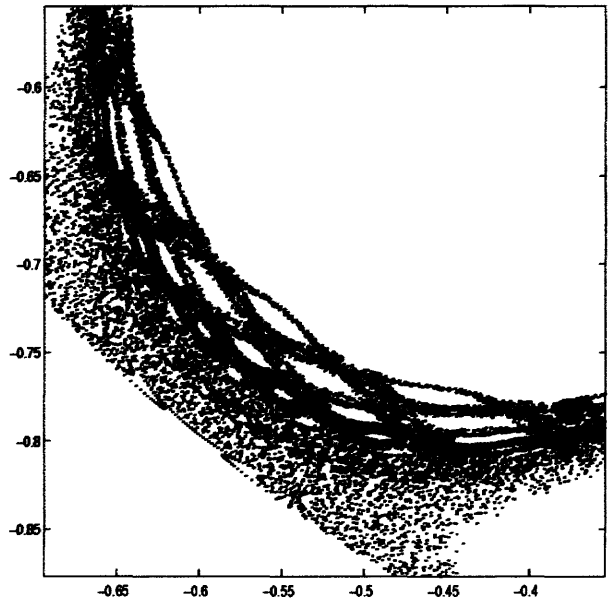

Figure 5.9 Magnification of the stochastic layer

CHAPTER 6

EXPERIMENT

An experiment has been set up at NJIT by John Batton and Ahmed Ould el Moctar, in order to test the theoretical predictions. The different phase space regions with their own dynamics were obtained experimentally. Experimental and theoretical results agree well qualitatively, although differences, particularly in numerical values at which bifurcations take place, will be highlighted as well.

6.1 Description of the Apparatus

For convenience, the experiment was set up at macro-scale in a circular container with a radius of 2 inches and a height of 4 inches. The tank was made out of glass to facilitate the visualization of the flow through a clear boundary (see Figure 6.1). The stirrer is a rod of radius 1.6 mm, capable of spinning with a rotational speed of 2000 rpm. The fluid used is glycerin which has a density of 1173 Kg/m^3 and the high viscosity of 0.76 $Pa.s$ (water 0.001 $Pa.s$).

The passive tracer is a fluorescent dye made up of fluorescent powder (Cole-Palmer, Fluorescent Dye Tablets Model 295-17) dissolved in glycerin prior to performing the experiment. This fluorescent dye is characterized by a very low diffusion coefficient and a sharp contrast with glycerin [25]. The dye is excited by four sets of long-wave 365 nm UV lights (Fisher, model XX-015N) which originate from a square array located directly above the container. In order to avoid the effect of surface tension, the dye is injected about 2 mm underneath the free surface of glycerin with a syringe.

The best view of the flow was obtained by taking pictures from below the container through a mirror, with a digital 5 Mega-pixels camera. Pictures thus captured will be used later for comparison with the theoretical streamline patterns as well as for mixing measurements.

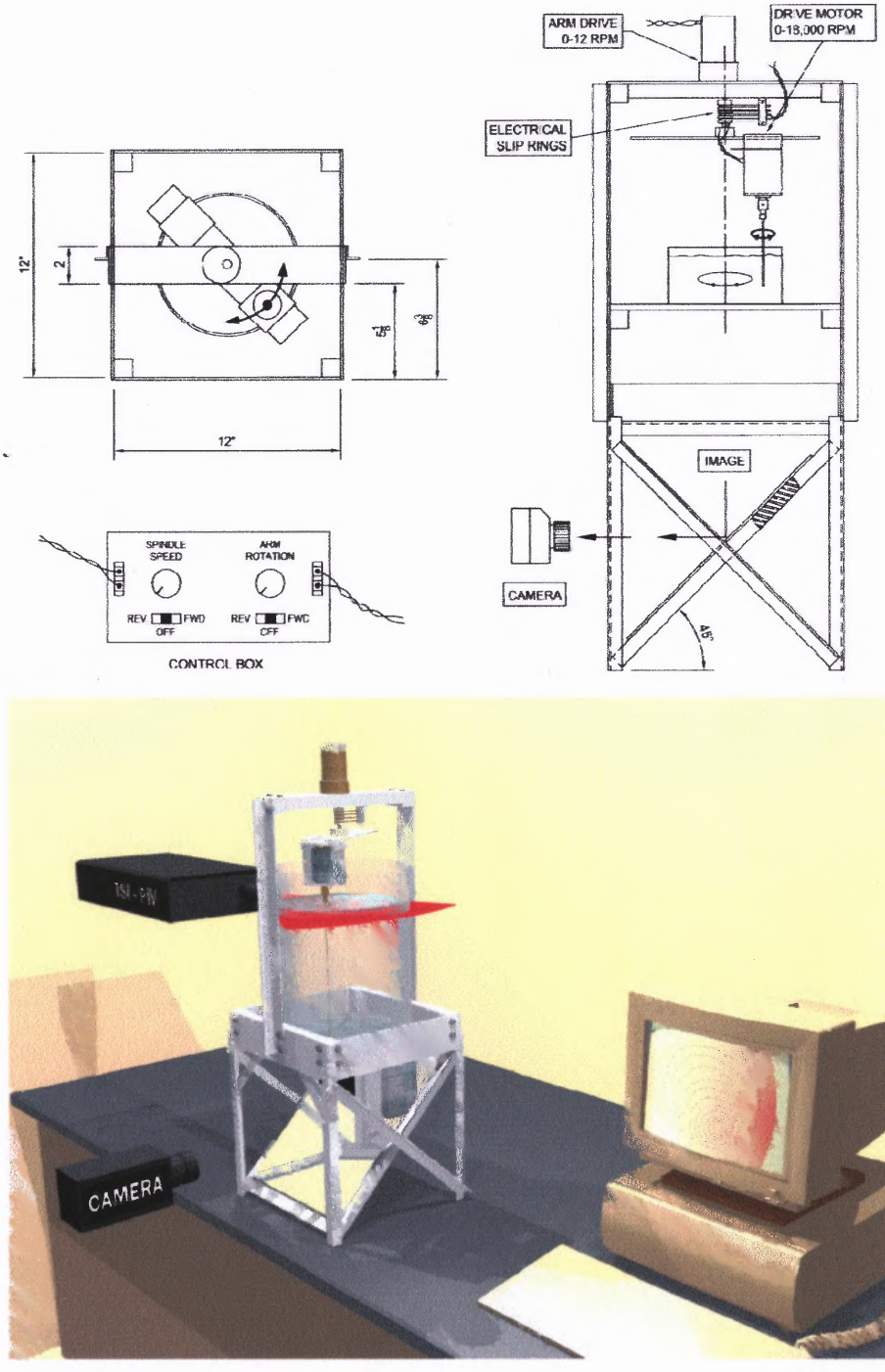

Figure 6.1 Apparatus

We define a Reynolds number for our system based on the parameters of the apparatus.

$$R_e = \frac{(\Omega\, r_0 + \omega\, r)(r - r_0)}{\nu} \tag{6.1}$$

where

- r_0 is the radius of the rod,
- r is the radius of the container,
- ω is the angular velocity of the arm,
- Ω is the angular velocity of the rod
- and ν is the kinematic viscosity of the glycerin.

Ω ranges from 0 to 18000 RPM (Spindle motor - Buehler Model 13.65 Permanent Magnet with AC Tachometer Output). A regulation device using a feedback action enables the precise control of this rotating speed.

The range of ω values, from 0.5 to 12 RPM, has been determined so that turbulence does not occur behind the 2D-cylinder rod (Motor to move swing Arm - McMaster-Carr 6331K34 Permanent Magnet DC Gearmotor). The Reynolds number (6.1) indeed remains between 114 and 116 in the conditions of our experiments.

The computation of the value of β experimentally is carried out by using the formula

$$\beta = \omega \pi a^2 / \Gamma \tag{6.2}$$

where a is the radius of the container. Throughout the previous chapters, the radius was taken as $a = 1$, but for comparison with the experiment we need to consider the relation (6.2). The strength of the vortex, Γ, is determined by the circulation of the fluid around the rod, i.e. $\Gamma = \oint_{rod} v.dl = 2\pi\Omega r_0^2$. It follows that our experimental β is

$$\beta = \frac{a^2}{2r_0^2}\frac{\omega}{\Omega}. \tag{6.3}$$

With the dimensions of our apparatus being $a = 5cm, r_0 = 1.6mm$, we have $\beta = 485.7\frac{\omega}{\Omega}$.

6.2 Experimental Results

In order to capture the various features of the dynamics in the different regions of the phase space, three droplets of fluorescent glycerin were injected into the container as initial conditions. The evolution of the droplets was then followed as time increased.

6.2.1 Flow with a Uniform Rotating Vortex

The first set of experiments were conducted for the purpose of checking the existence of the four different phase space dynamics predicted by the theory, referred to as Region I, II, III, IV on the bifurcation diagram Figure 6.2 displays the dynamics in the four regions.

The reversibility of the dynamics was also corroborated experimentally with one droplet as the initial condiiton. The inverse dynamics was produced by changing the direction of the angular rotation ($\omega \rightarrow -\omega$) as well as the vortex circulation ($\Omega \rightarrow -\Omega$), while keeping β unchanged (corresponding to the same flow structure but with a reversed flow direction).

A set of experiments and the corresponding numerical simulations were run for the purpose of comparison. The presence of viscous effects in the experiments led to a disagreement between the values of bifurcation parameters in the theory and the experiments. A direct comparison thus needed additional care. For this purpose, the initial angular position of the vortex and that of the initial blob of dye were directly measured from the experimental photos. The value of the dimensionless parameter β was then deduced by measuring the position of the saddle point from the experimental visualizations. That is, the matching of parameters was performed by matching the position of the saddle point only.

The initial condition was composed of three different blobs along the diameter in order to capture the various flow structures.

One can clearly observe from the experimental photographs that the flow patterns obtained experimentally are very similar to those derived from the theory. Differences, however, are noticeable in the bifurcation diagram, particularly in the transition values of β between the different regions. We give below a table comparing the values of β at which the transition between the various regimes occurs.

Transition	Experiment	Theory
Region I-Region II	$\sim$ 0.2	2
Region III-Region IV	$\sim$ -0.3	-4

It is conjectured that the viscous effects neglected in the theory are responsible for this discrepancy (of a factor of 10).

While the velocity profile of a point vortex is $\sim 1/r$ in potential flow theory, the high viscosity of the glycerin used in the experiments leads to a greater damping in the velocity field. Consequently, for the same configuration, for instance in Region I, for a given speed ω, the saddle point is closer to the vortex in the experiment than it is according to the theoretical predictions of the previous chapters.

For example, the transition between Region I and Region II occurs when the saddle point approaches the boundary of the container. Since the position of the saddle point is closer to the vortex experimentally, we have to decrease the parameter β, or equivalently ω in the experiment, for the saddle point to reach the boundary of the container.

Another discrepency between theory and experiment occurs in the neighborhood of the edge of the container. In the potential flow model, the boundary is identified with a specific streamline. However, in a viscous flow, the no-slip boundary condition manifests itself by a zero velocity of the fluid on the edge of the container. Consequently,

the heteroclinic orbit joining two saddle points on the boundary in Region II of the theoretical model is shifted toward the inside of the container in the experiment.

Finally, the experimental identification of Region III is a challenge since this regime requires a very low speed of the arm, at the limit of the range of speeds generated by the motor used. Although the dynamics of this region was identified, the motion of the arm was not very smooth and the experimental streamlines somewhat disturbed.

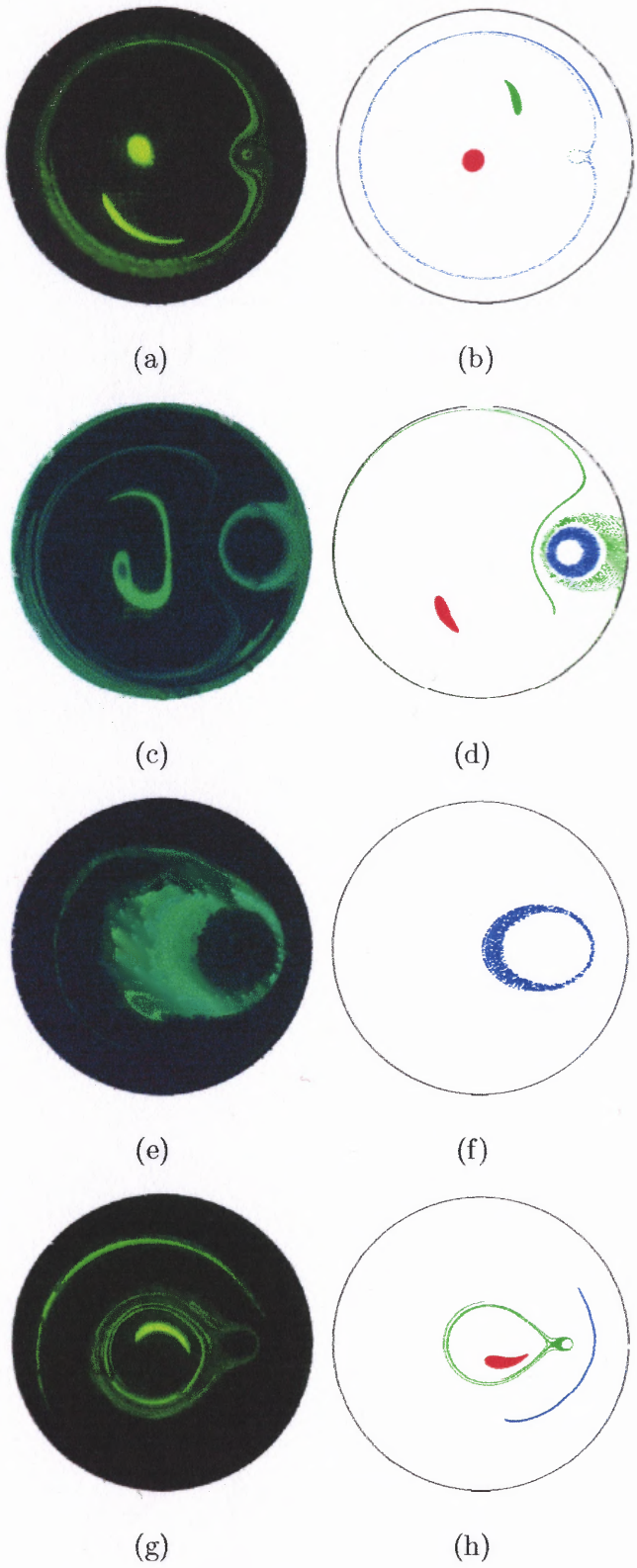

Figure 6.2 Comparison between experiment and theory for the four different flow patterns.

6.2.2 The Dual Speed Vortex

Experiments were conducted for a dual speed vortex by considering a certain value of β_1 and choosing $\beta_2 = -\beta_1$. This corresponds to fixing an angular speed of the stirring rod and switching periodically from a clockwise to counterclockwise motion while keeping the same absolute angular velocity. Instead of considering the time periods $T1$ and $T2$, we consider the angle α_1 or α_2 traveled by the vortex during the time T_1 or T_2, where $\alpha_1 = \omega_1 T_1$ and $\alpha_2 = \omega_2 T_2$. Later on, a comparison of mixing properties between a set of experiments will be made varying α_1 and α_2.

6.3 Comparison of the Measure of the Mixing between Experiment and Numerical Simulation

In order to compare the different cases, the degree (or index) of mixing was measured by considering the relative covering of the dye with respect to the container. A low index, where the dye remains in a relatively concentrated area is referred to as poor mixing while an index close to 1 corresponds to very good mixing, i.e the dye spreads almost everywhere.

The measure is obtained by a digital treatment of the experimental photographs (see Figure (6.3))with the software *ImageJ* [19].

We first convert the color picture into grey scales, the different levels of grey corresponding to the local concentration of the fluorescent dye. We then filter the dye from the background by setting a threshold on the grey level. The value of this threshold is selected to capture as much as possible of the real spreading of the dye throughout the picture when mixing occurs. The same threshold is kept for all pictures of one experiment. By doing so, some of the regions showing a poor contrast with the background are left out.

The measurement of the dye covering is carried out by counting the number of pixels of the filtered dye, a function available in the software *ImageJ*.

The number of pixels in the container is counted initially in order to be able to compute the percentage of the dye covering within the container as a function of time.

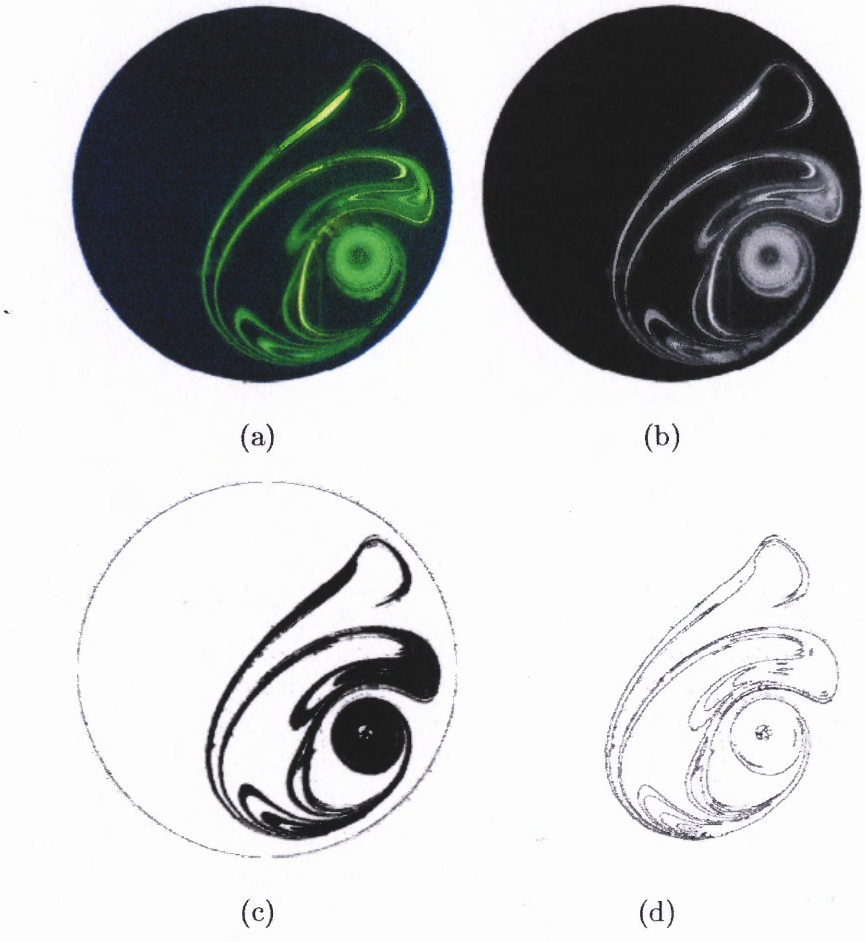

Figure 6.3 Digital treatment of the experimental picture: (a): original picture, (b) : conversion 8 bits shaded gray, (c) : filtering on threshold binary picture, (d) : outline of the covering of the dye

We give below the covering of the dye versus time for different mixing protocols corresponding to various values of α_1, α_2. In this case, the dimensionless parameter takes the value $\beta = 0.24$, and we denote by $\pi - \pi/2$ the experiment in which the vortex (rod) travels in the counterclockwise direction over the angle π and in the clockwise direction over the angle $\pi/2$. This motion is then repeated in a periodic fashion.

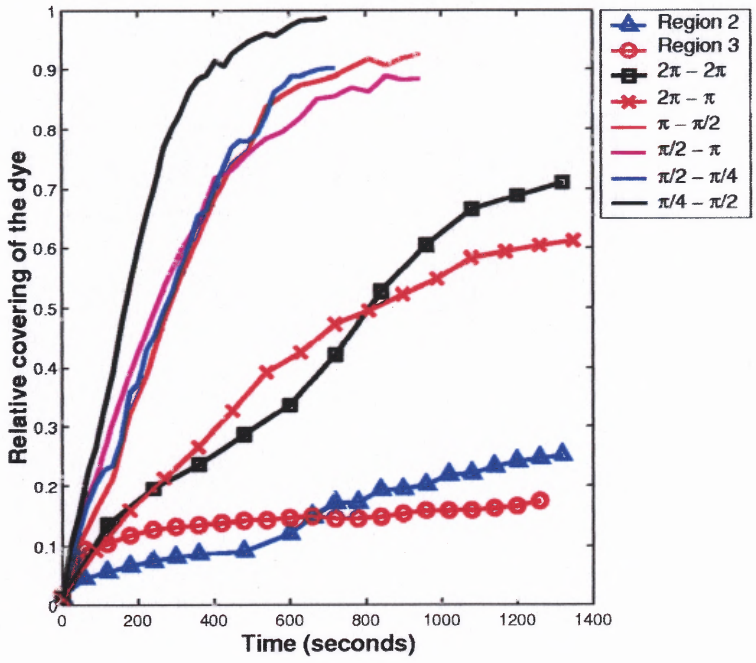

Figure 6.4 Relative covering of the dye for different protocols of mixing with $\beta = 0.24$

Figure (6.4) shows a significant enhancement of mixing with a dual speed rotating vortex. With only one angular speed, the covering of the dye is about 15-20 percent of the container. However, with the dual speed protocol $\pi/4 - \pi/2$, almost 100 percent is reached in a short period of time. In Figure (6.4), the importance of the two angles α_1, α_2 is clearly shown. A detailed study of how these angles influence the dye covering is not considered here. However, we can point out that more frequent changes in direction, i.e. decreases in α_1, α_2, facilitate the mixing (see Figure (6.4)).

In Figure (6.5)-(6.6), we give several snapshots of Both the numerical simulation and experiment in order to compare the time evolution of the initial blobs. Particularly, we consider the case $\pi/4 - \pi/2$ and $\pi/2 - \pi/4$ for an experimental value of the dimensionless parameter $\beta = 0.24$. Qualitatively, the numerical simulations exhibit the same flow patterns or shape of blobs as the experimental visualizations. The numerical accuracy required to obtain the folding and stretching of the material lines clearly visible in this figure consisted of about 10^5 points in each initial blob.

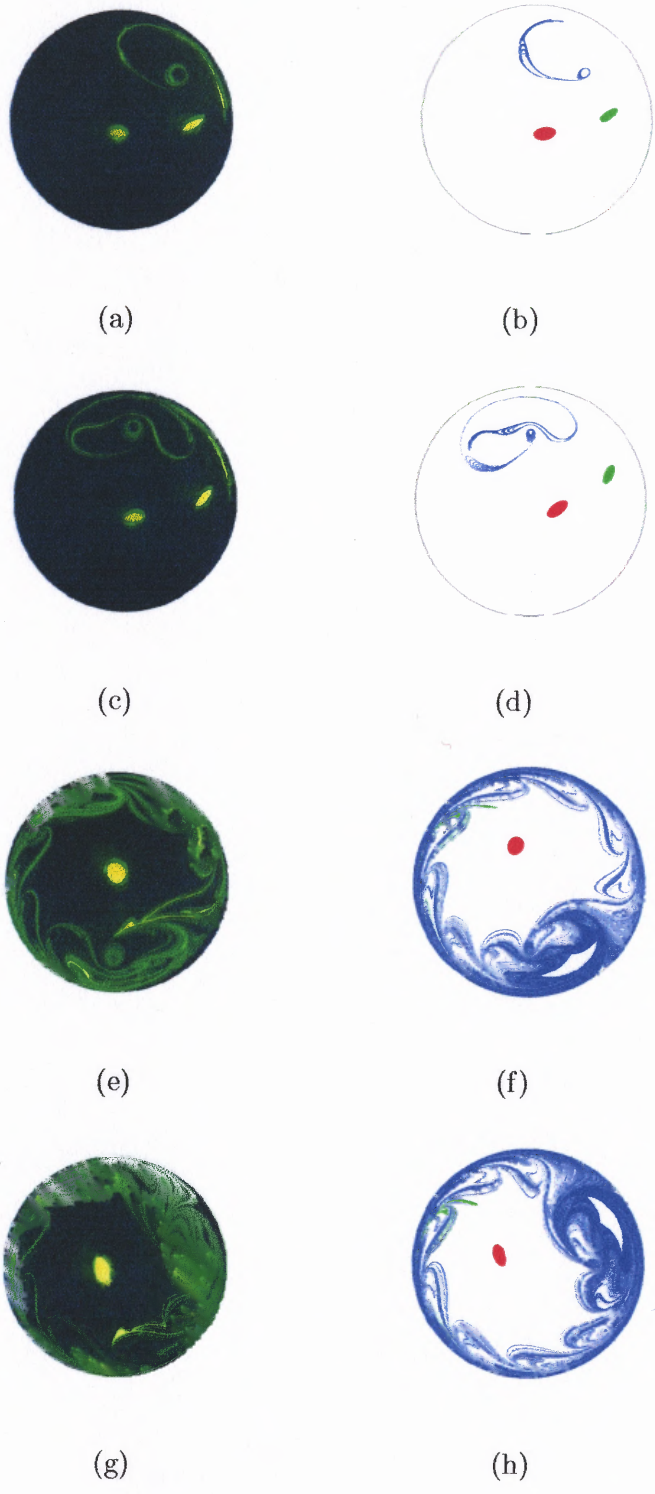

Figure 6.5 Comparison numerical simulation and experiment for the case of an experimental $\beta = 0.24$ and $\pi/2$ counterclockwise and $\pi/4$ clockwise

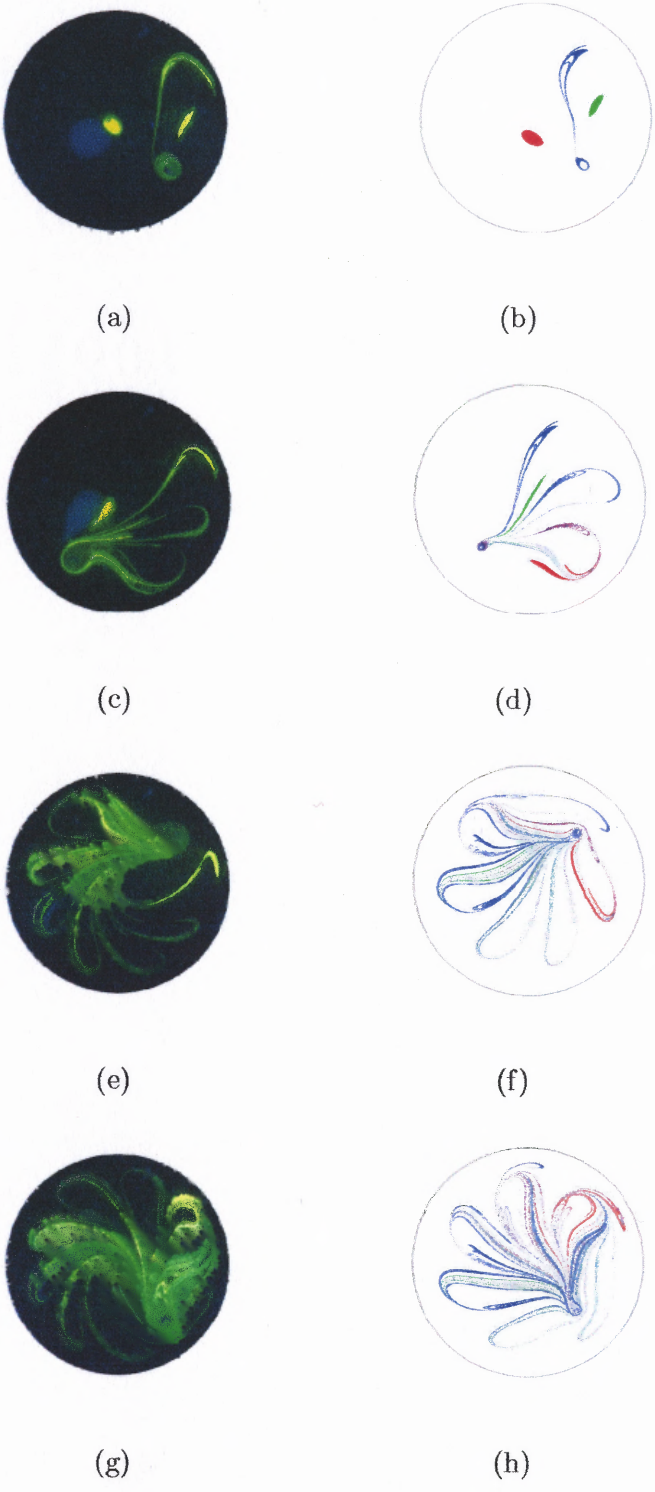

Figure 6.6 Comparison numerical simulation and experiment for the case of an experimental $\beta = 0.24$ and $\pi/4$ counterclockwise and $\pi/2$ clockwise

CHAPTER 7

CHAOTIC ADVECTION USING PERTURBATION

We consider in this section only Region IV of Chapter 3, which has two homoclinic orbits with an "eight shape" and study the influence of a perturbation in the Hamiltonian corresponding to the case of a constant angular speed. The perturbation is introduced in the angular velocity of the vortex, so that $\alpha(t) = \omega\, t + A\ \sin(\Omega t)$. The numerical procedure used in this section is a symplectic Runge-Kutta scheme.

7.1 Symplectic Runge-Kutta Scheme

The numerical simulations performed in the next sections involve integrations which need to be carried out over a very long time or possessing specific structures. It is known that a regular Runge-Kutta scheme which is not symplectic is inappropriate for Hamiltonian problems especially for long times of integration. In particular, some quantities like constants of motion may not be preserved, and there may be a drift in the energy or some canonical features may not be satisfied.

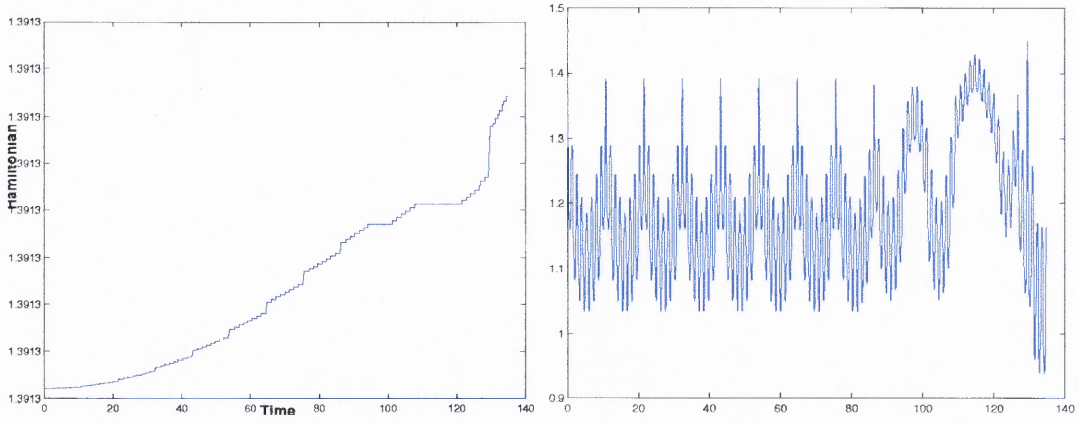

Figure 7.1 Drift in the energy with a Runge-Kutta scheme of 8th order

Figure (7.1) shows a drift in the energy of the order of 10^{-8}. Although this drift is quite small, it has a significant effect on the trajectory as we can see on the plot in the right. Indeed, in this case, we have a closed, periodic orbit in phase space, but the

error due to the numerical scheme produces a non-periodic, complicated trajectory. We will return to this example in Section 7.3.

One way to fix this problem is to perform a convergence study by decreasing the time step in the Runge-Kutta scheme. However, as we will see in Section 7.3, the time of integration required for convergence can be quite long, which makes the study too cpu consuming. Consequently, we decided to implement a symplectic scheme based on the Runge-Kutta approach. We give here some details about the scheme which can be found in references [33],[34],[35]. More information about integrating Hamiltonian problems can be found in [40], or on the Synode project [39].

The goal is to solve a set of ODE's, more precisely the Hamiltonian equations (2.34). We rewrite these equations in the generic form

$$\frac{d\mathbf{y}}{dt} = \mathbf{f}(t, \mathbf{y}), \qquad \mathbf{y}(t_0) = \mathbf{y}_0 \tag{7.1}$$

where

$$\mathbf{y} = \begin{pmatrix} X \\ Y \\ \tau \\ F \end{pmatrix} \qquad \mathbf{f}(t, \mathbf{y}) = \begin{pmatrix} \frac{\partial H}{\partial Y} \\ -\frac{\partial H}{\partial X} \\ \frac{\partial H}{\partial F} \\ -\frac{\partial H}{\partial \tau} \end{pmatrix}. \tag{7.2}$$

In order to integrate System (7.1), we use a time discretization, with time step h, based on a Runge-Kutta scheme with s stages. The time discretization can be written as

$$\mathbf{y}_{n+1} = \mathbf{y}_n + h \sum_{j=1}^{s} b_j \mathbf{f}(t_n + c_j h, \mathbf{y}^{(j)}) \tag{7.3}$$

where "the internal stages" $\mathbf{y}^{(j)}$ are solutions of the following non-linear system of algebraic equations

$$\mathbf{y}^{(i)} = \mathbf{y}_n + h \sum_{j=1}^{s} a_{ij} \mathbf{f}(t_n + c_j h, \mathbf{y}^{(j)}), \quad i = 1, \ldots, s. \tag{7.4}$$

Here the coefficients c_i are defined by

$$c_i = \sum_{j=1}^{s} a_{ij}. \tag{7.5}$$

The parameters c_j, b_j, a_{ij} are chosen so that $\mathbf{y}_n$ represents an approximation of the Taylor expansion of the solution. In the literature, these coefficients are given in a table referred to as a "Butcher Tableau" [11].

$$\begin{array}{c|ccc} c_1 & a_{11} & \dots & a_{1s} \\ \vdots & \vdots & \ddots & \vdots \\ c_s & a_{s1} & \dots & a_{ss} \\ \hline & b_1 & \dots & b_s \end{array} \tag{7.6}$$

We denote by Φ_h a map with time step h, $\Phi_h : \mathbf{y}_n \rightarrow \mathbf{y}_{n+1}$, for the evolution of the solution.

Definition 1 *A method Φ_h is symplectic for any h and any Hamiltonian system for which it is applicable if its Jacobian $\frac{\partial \Phi_h}{\partial z}$ satisfies*

$$(\frac{\partial}{\partial z}\Phi_h)^T J(\frac{\partial}{\partial z}\Phi_h) = J \quad ,with\ J = \begin{pmatrix} 0 & I \\ -I & 0 \end{pmatrix}. \tag{7.7}$$

A condition to ensure that the Runge-Kutta scheme (7.3) is symplectic (see [24], [40]) is

$$b_i a_{ij} + b_j a_{ij} - b_i b_j = 0, \quad i, j = 1, \dots, s. \tag{7.8}$$

The internal stages require the solution of an implicit system (7.4) at each time step. For instance, a three stage scheme will produce a system of 12 equations for our Hamiltonian equations with the canonical variables $(X, Y; \tau, F)$. Newton's method is used to solve this system.

For a nonlinear system $\mathbf{g}(\mathbf{x}) = 0$ with several variables, we recall Newton's method. After solving the following linear system at the n-th time step:

$$J\delta = -\mathbf{g} \quad \text{where } J \text{ is the Jacobian matrix of } \mathbf{g} \tag{7.9}$$

we update the value of $\mathbf{x}$

$$\mathbf{x^{(n+1)}} = \mathbf{x^{(n)}} + \delta^{(n)}. \tag{7.10}$$

Newton's method is repeated until $\|\delta^n\| < 10^{-14}$. This involves a 12 by 12 Jacobian matrix which is generated by the mathematical software, Mathematica [28], and exported to a C-code automatically.

The algorithm is as follows :

Algorithm 1 Symplectic Scheme :

Initialization of the canonical variables : $V = (X, Y; \tau, F)$

for $t = 0 : h : T_{max}$ **do**

  while $error > 10^{-14}$ **do**

    Compute Jacobian Matrix J (12x12)

    Compute $\mathbf{g}$

    Solve $J\delta = -\mathbf{g}$ {by LU Decomposition}

    $\mathbf{x} \Leftarrow \mathbf{x} + \delta$ {Update solution}

    $error = \|\delta\|_\infty$

  end while

  $\mathbf{V} \Leftarrow \mathbf{V} + \mathbf{x}$ {Update canonical variables}

end for

We implemented three different schemes in order to compare them and check their respective convergence.

The first scheme has one stage and it is of order 2; its Butcher Tableau is

$$\begin{array}{c|c} \frac{1}{2} & \frac{1}{2} \\ \hline & 1 \end{array} \tag{7.11}$$

This scheme is equivalent to the midpoint rule.

$$\mathbf{y}_{n+1} = \mathbf{y}_n + h\mathbf{f}\left(t_n + \frac{h}{2}, \frac{1}{2}(\mathbf{y}_n + \mathbf{y}_{n+1})\right). \tag{7.12}$$

The next scheme is 4^{th} order with two stages, with the following coefficients

$$\begin{array}{c|cc} \frac{1}{2} \pm \frac{1}{2\sqrt{3}} & \frac{1}{4} & \frac{1}{4} \pm \frac{1}{2\sqrt{3}} \\ \frac{1}{2} \mp \frac{1}{2\sqrt{3}} & \frac{1}{4} \mp \frac{1}{2\sqrt{3}} & \frac{1}{4} \\ \hline & \frac{1}{2} & \frac{1}{2} \end{array} \tag{7.13}$$

The last scheme of 6^{th} order with three stages has the coefficients

$$\begin{array}{c|ccc} \frac{1}{2} + \tilde{c}_1 & \frac{5}{36} & \frac{2}{9} + \frac{2\tilde{c}_1}{3} & \frac{5}{36} + \frac{\tilde{c}_1}{3} \\ \frac{1}{2} & \frac{5}{36} - \frac{5\tilde{c}_1}{12} & \frac{2}{9} & \frac{5}{36} + \frac{5\tilde{c}_1}{12} \\ \frac{1}{2} - \tilde{c}_1 & \frac{5}{36} - \frac{\tilde{c}_1}{3} & \frac{2}{9} - \frac{2\tilde{c}_1}{3} & \frac{5}{36} \\ \hline & \frac{5}{18} & \frac{4}{9} & \frac{5}{18} \end{array} \tag{7.14}$$

where $\tilde{c}_1 = \pm\frac{1}{2}\sqrt{\frac{3}{5}}$. This scheme should be the most accurate, and is referred to as the Gauss-Legendre method of order 6.

A convergence study for one set of parameters is given in Figure (7.2). The following plot shows the drift in energy as a function of time step h. For smaller time steps, the drift should be reduced since the energy or Hamiltonian is a constant of motion.

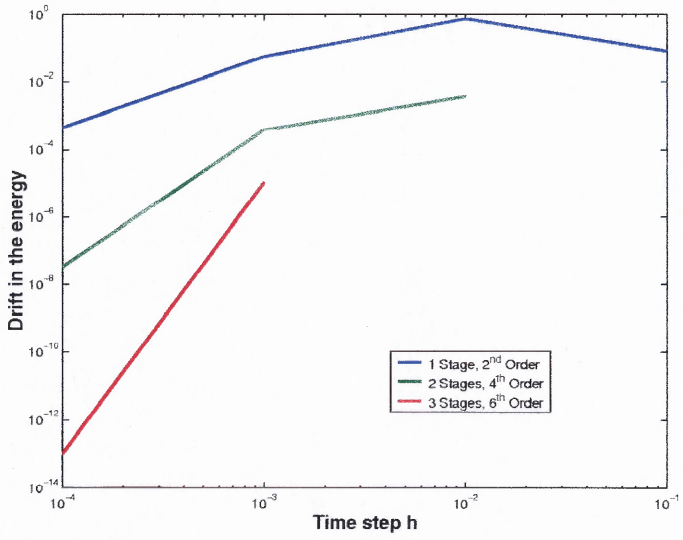

Figure 7.2 Drift in the Hamiltonian versus the time h for three different symplectic schemes.

In the next sections, we will use the Gauss-Legendre method of order 6, with time step 10^{-6} to ensure sufficient accuracy for the broad range of situations we will encounter.

7.2 Formation of Lobes, Homoclinic Tangles and Chaotic Transport

First, we study the stability of the homoclinic orbit under perturbation. The perturbation is introduced in the angular position of the vortex, i.e. $\alpha(t) = \omega t + A \sin(\Omega t)$. Consequently, our Hamiltonian becomes

$$H(X,Y;\tau,F) = -\frac{\Gamma}{2\pi}\log\left(\frac{(X-e^{-b})^2+Y^2}{(X-e^{b})^2+Y^2}\right)+\frac{\omega}{2}(X^2+Y^2)+F+\frac{\Omega A}{2}\cos(\Omega\tau)(X^2+Y^2). \tag{7.15}$$

For $A = 0$, we know from Section 3.2 that we have a saddle point with two homoclinic orbits. Numerically, we choose to investigate only the homoclinic orbit around the vortex. One of the interesting scenarios occurs in the case of small A, i.e $A \ll \omega$, where the homoclinic connection breaks and leads to a transverse homoclinic orbit, where the unstable and stable manifold intersect transversally.

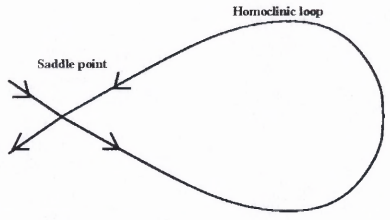

Figure 7.3 Unperturbed homoclinic orbit

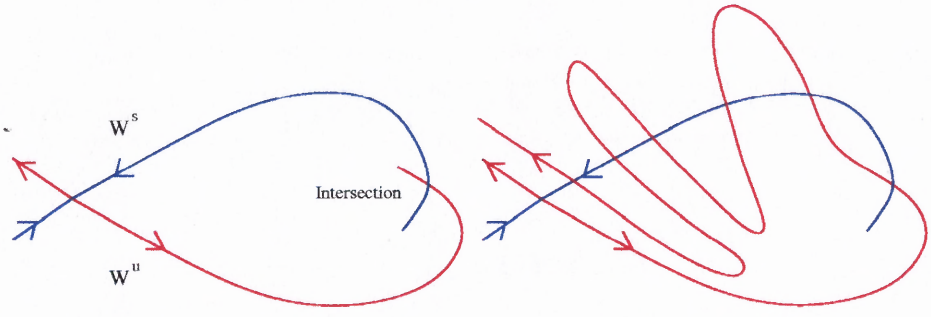

Figure 7.4 Transverse intersection unstable/stable manifold

In this situation, it is known that the two manifolds intersect an infinite number of times, leading to a complicated pattern (see Figure (7.4)), and that there is a hyperbolic invariant set in the neighborhood of the saddle point (Smale's Theorem), i.e an horseshoe [15], [47].

Such a configuration for the stable and unstable manifold leading to chaotic transport have been studied in detail [7], [48].

The Melnikov method can be used to check the existence of the transverse intersection, as well as a direct numerical simulation with the unperturbed homoclinic orbit as the initial condition.

We now consider a direct simulation with the following parameter values $T_1 = 0.2, b = 0.5108, \beta = -6, \omega = -\pi/T_1, \Gamma = \omega\pi/\beta, \Omega = 11\omega; A = 10^{-3}$. The initial condition is the unperturbed homoclinic orbit defined with about 4000 discrete points. The discretization of the homoclinic orbit is carried out with Matlab ([29]) by plotting the level curve corresponding to the homoclinic orbit with a small mesh size, $\triangle x = 10^{-2}$.

Figure 7.2 displays the trajectory going twice around the homoclinic orbit showing the presence of lobes and tangles. In this situation, the chaotic transport was described theoretically by studying the evolution of the lobes and tangles [7].

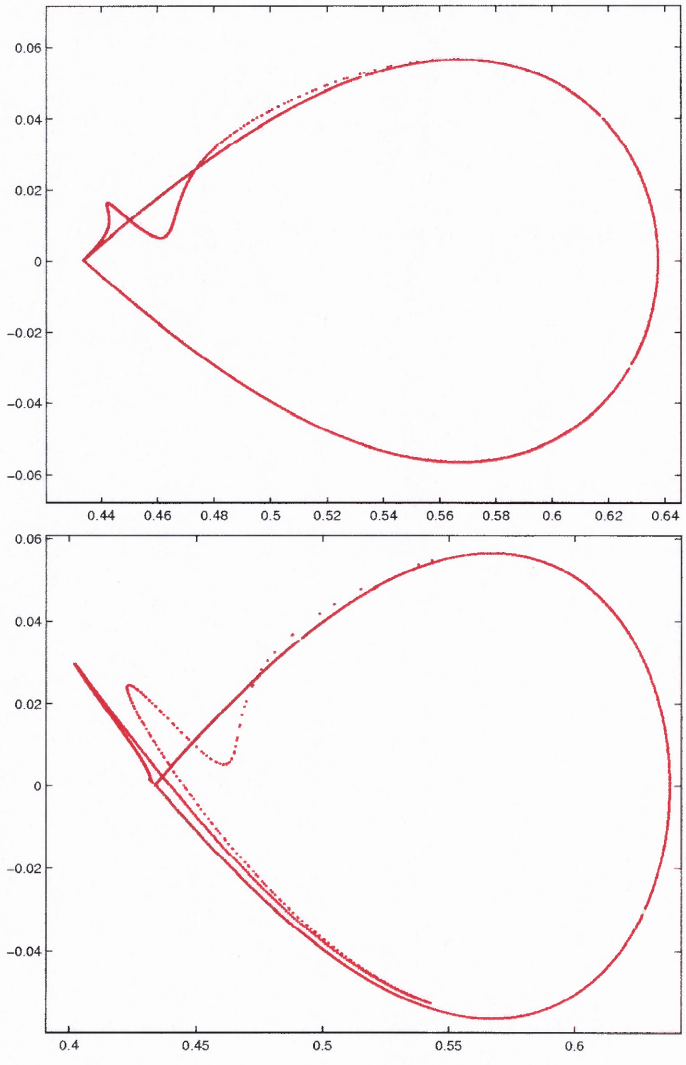

Figure 7.5 Numerical simulation of the transverse homoclinic orbit

7.3 Resonances and bifurcation cascade

We now consider a perturbation of the angular velocity of the vortex so that ω now becomes $\omega + A\cos(\Omega t)$; the amplitude A is now a function of Ω, such that $A = 1/\Omega$. The corresponding dimensionless rotation parameter becomes $\beta(t) = \frac{\omega\pi}{\Gamma} + \frac{A\Omega\pi}{\Gamma}\cos(\Omega t)$.

From the phase space analysis of Chapter 3, we know that the value of this parameter determines the topology of the flow, i.e. its fixed points and separatrices. The time dependent β above will result in a separatrix oscillating about the unperturbed separatrix, which is also its average position.

In the limit case where $\Omega << 1$, corresponding to a slow separatrix motion, well-known techniques are available to study the dynamics such as the method of averaging [26]. However, in order to have a significant change in the dynamics, we consider the rotation parameter value : $\beta_0 = \omega\pi/\Gamma = -6$. At this value, the flow has two homoclinic orbits with an eight shape (REGION IV) and $\frac{A\Omega\pi}{\Gamma} = 1$. This constraint implies that $-7 < \beta(t) < -5$, which means that the trajectory remains in the REGION IV for all β values. The initial condition is the unperturbed saddle point, located at $z_0^* = (x^*(\beta_0, b), 0)$. The trajectory fills a region delimited by the extremal positions of "the oscillating separatrix" and is referred to as the stochastic region.

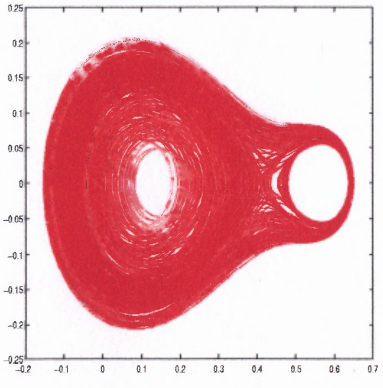

Figure 7.6 Stochastic region

However, for specific values of Ω, the trajectory becomes more localized in space and does not spread everywhere in the stochastic region. These values will be referred to as resonances and the trajectory is periodic with period T. This period is a multiple of the period of the forcing term, $T_f = 2\pi/\Omega$. Hereafter, we denote a resonance $n:1$, if the period of the trajectory is n times that of the forcing term, i.e. $T = nT_f$.

We rewrite $\Omega = \mu\omega$ and use μ as our parameter for the numerical simulations below.

The values of μ at which resonances occur are found by minimizing the distance of the returning point in the neighborhood of the initial condition z_0^* after a time of integration which is a multiple of the forcing period T_f. We stop the minimization when the distance is less than 10^{-13}. We consider the corresponding trajectory as periodic, and the value of μ is referred to as resonance $n:1$.

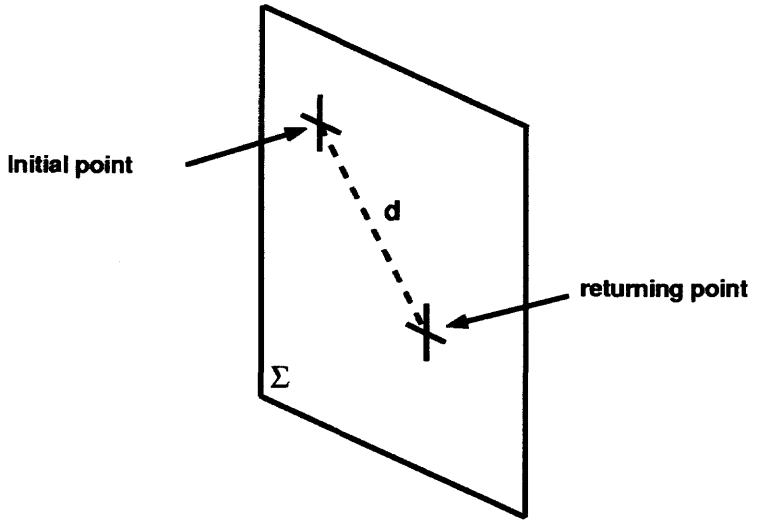

Figure 7.7 Poincaré section.

The tuning of the parameter μ is performed automatically by a "search program", given an initial guess.

Example for 1:1 resonance.

Initial Guess : 0.6. Best value (tuned value) : $\mu = 0.63256760329605$ as we tune the parameter μ (or go down the digit), the distance decreases (see Figure (7.8)).

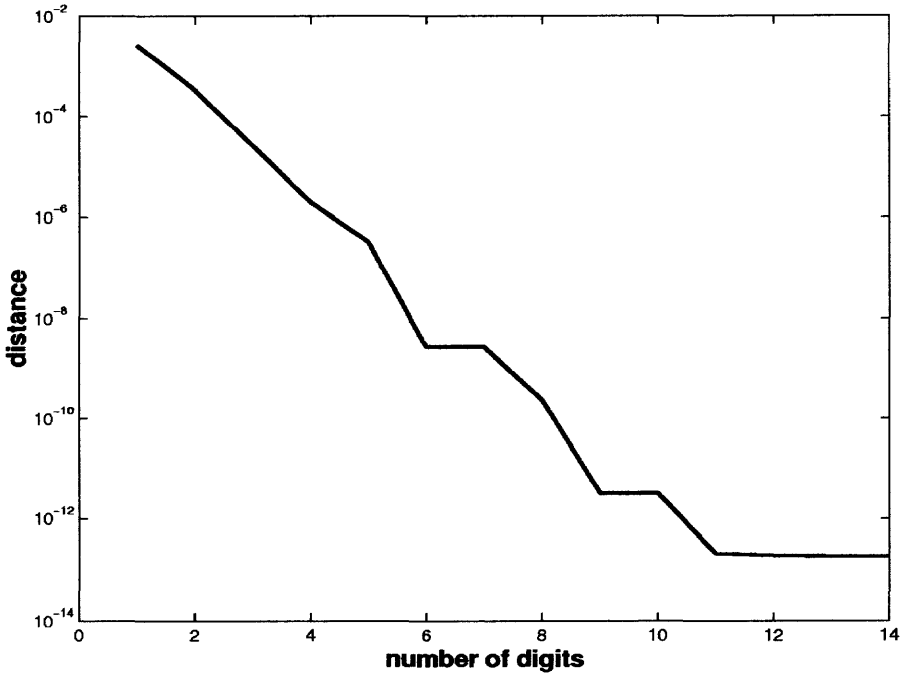

Figure 7.8 Distance of the returning point versus the number of digits.

Since we expect the trajectory to be periodic for these specific values, we compute the trajectory over 400 periods with our numerical scheme.

In Figure (7.9), we display the plot of μ versus the resonance $n:1$, showing the existence of five different families. For a given family, the values of μ accumulate, and seem to converge to some limit value as the resonance $n:1$ increases. However, the convergence is not exponential; a semilog plot of μ versus the resonance $n:1$ does not give a straight line even for high values of n. Consequently, we cannot characterize each family with an exponent or constant of convergence.

In order to observe the cascade of bifurcations and the period of the trajectory, we plot the canonical variable F versus time and give below the five different families. This list is not exhaustive, and more families can be found.

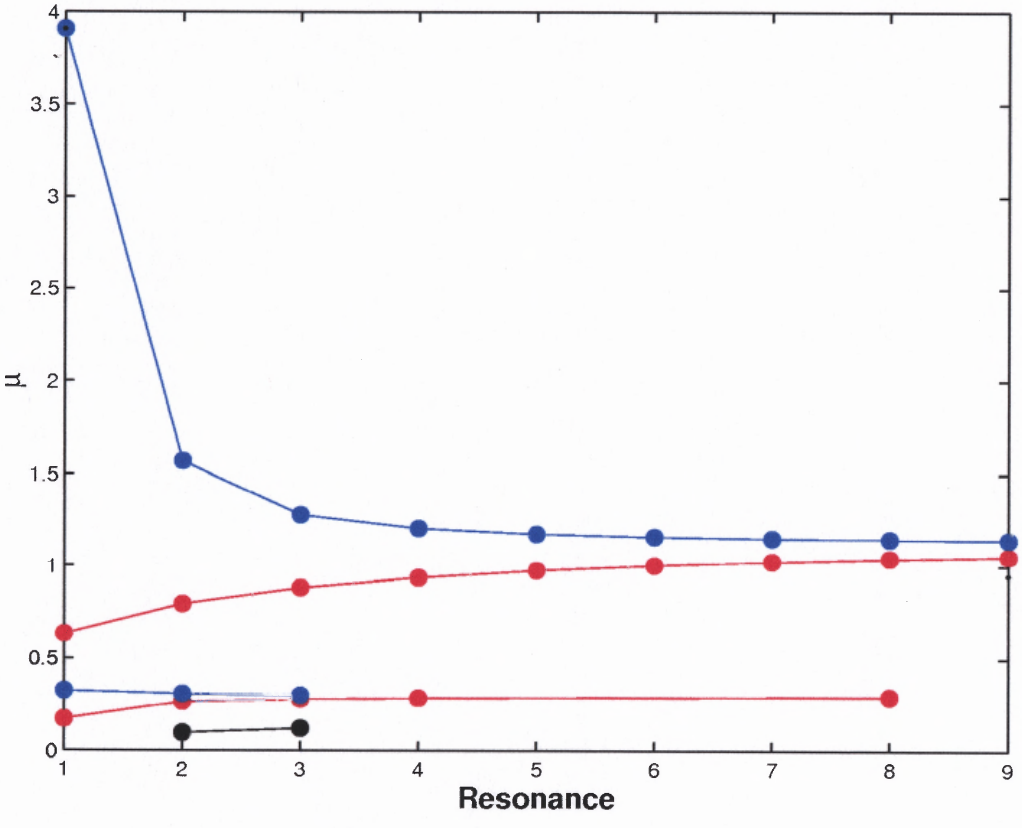

Figure 7.9 μ versus resonance $n:1$.

7.3.1 First family

The values of the parameter μ for the first family of resonances are

μ	Resonance
3.90673568801192	1
1.57137527669902	2
1.28014094538324	3
1.20779946875261	4
1.17752798401375	5
1.16223140190624	6
1.15361704275102	7
1.14840625354251	8
1.14508966293113	9

We give below the plot of the canonical variable F and the trajectory for each value of μ.

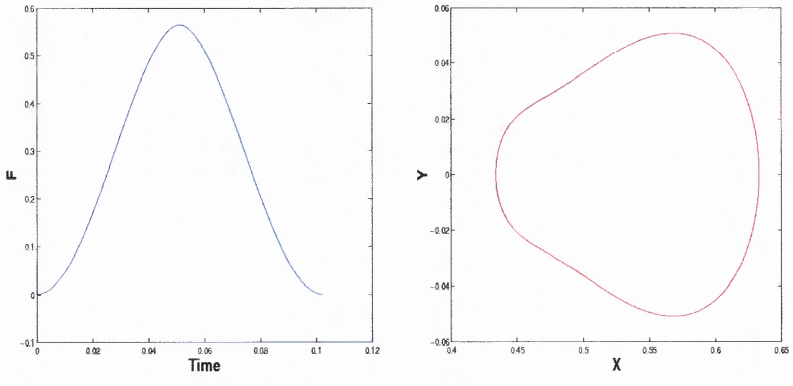

(a) (b)

Figure 7.10 (a)-(b) : Resonance 1:1.

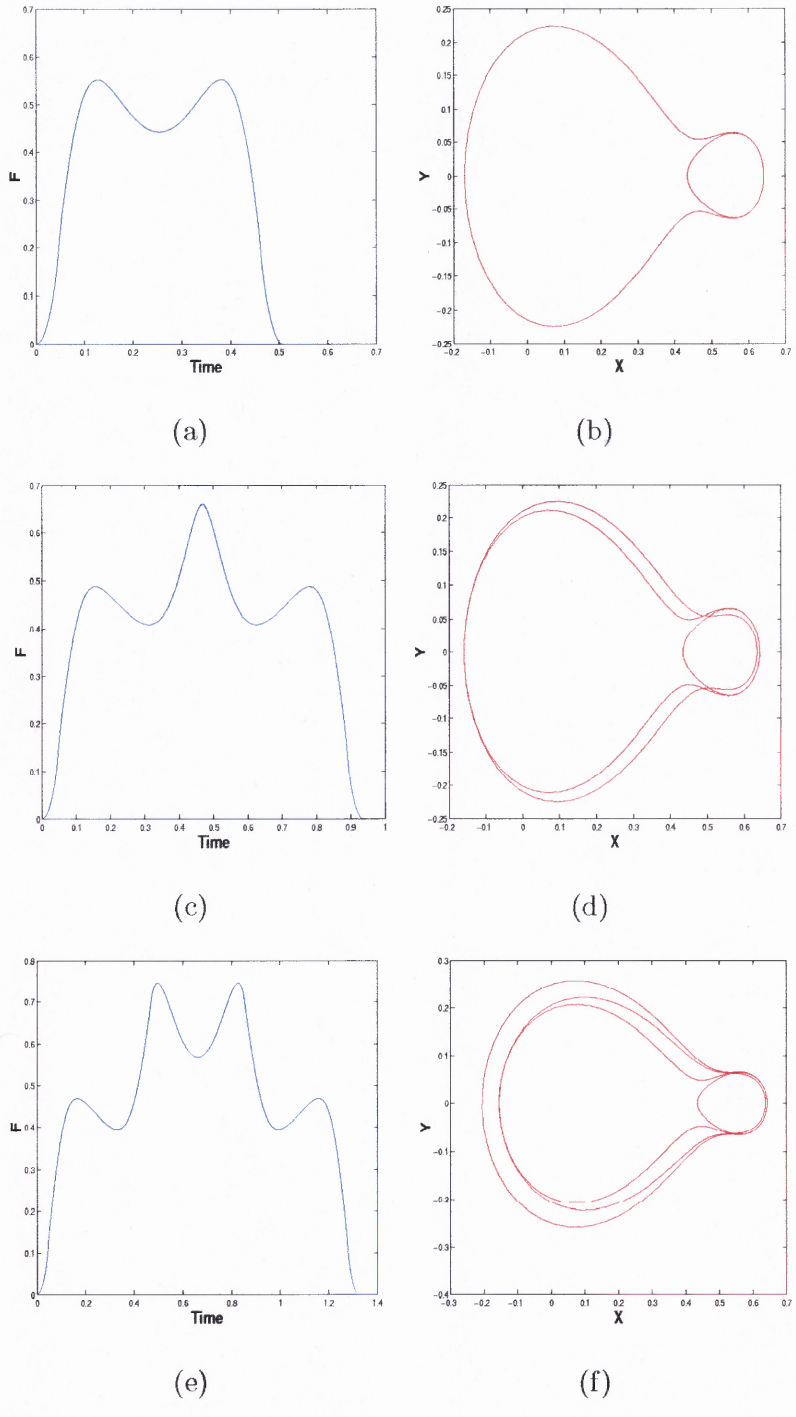

Figure 7.11 (a)-(b) : Resonance 2:1; (c)-(d) : Resonance 3:1; (e)-(f) : Resonance 4:1.

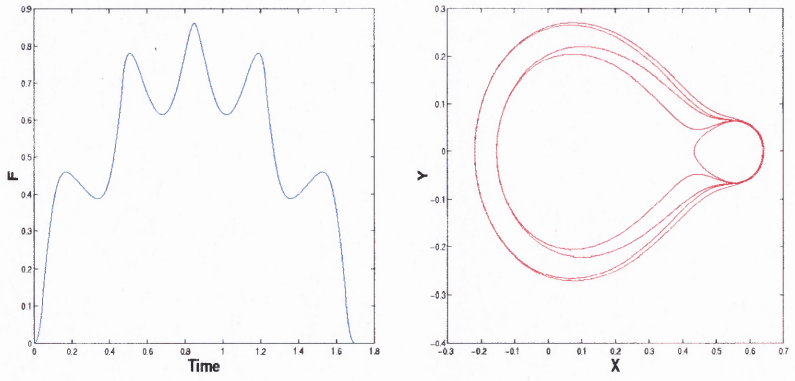

(a) (b)

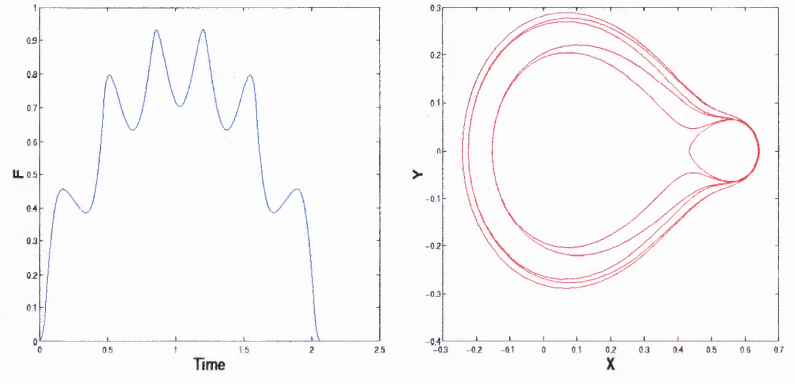

(c) (d)

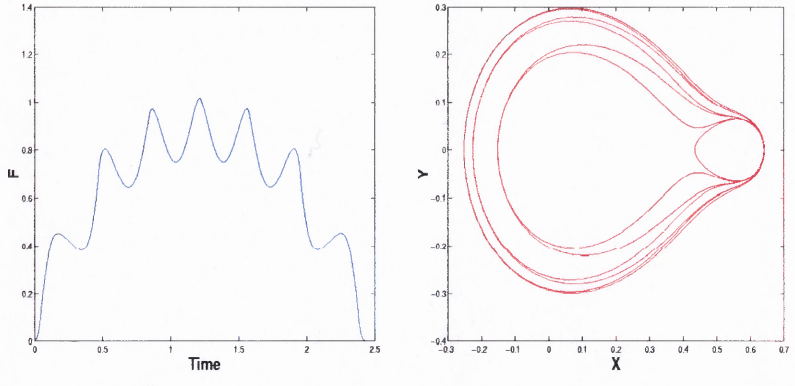

(e) (f)

Figure 7.12 (a)-(b) : Resonance 5:1; (c)-(d) : Resonance 6:1; (e)-(f) : Resonance 7:1.

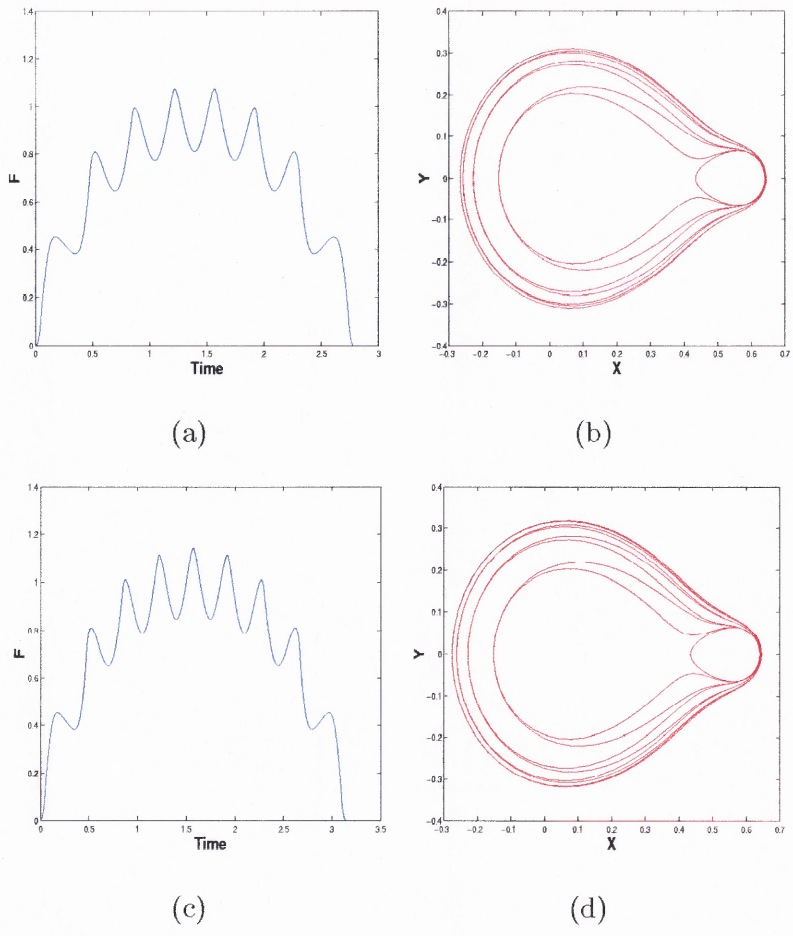

Figure 7.13 (a)-(b) : Resonance 8:1; (c)-(d) : Resonance 9:1.

7.3.2 Second family

The values of the parameter μ for the second family of resonances are

μ	Resonance
0.63256760329605	1
0.79566943874706	2
0.88313744550900	3
0.93886212443024	4
0.97735188487736	5
1.00506218046792	6
1.02570926461182	7
1.04153564457468	8
1.05395972205294	9

We give below the plot of the canonical variable F and the trajectory for each value of μ.

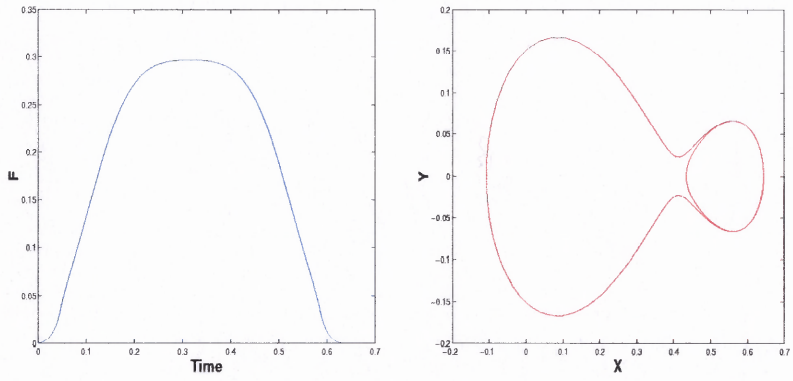

(a) (b)

Figure 7.14 (a)-(b) : Resonance 1:1

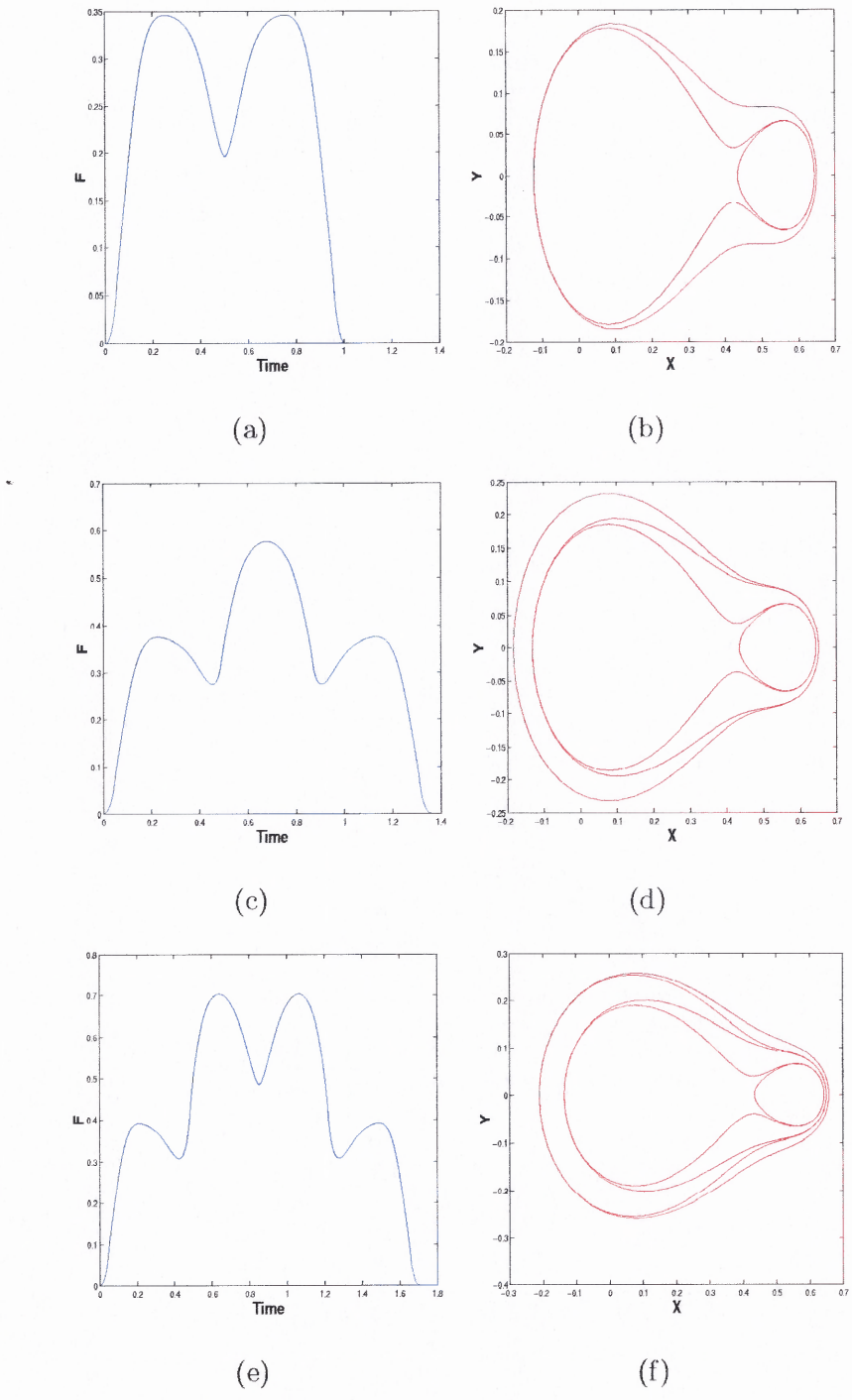

Figure 7.15 (a)-(b) : Resonance 2:1; (c)-(d) : Resonance 3:1; (e)-(f) : Resonance 4:1

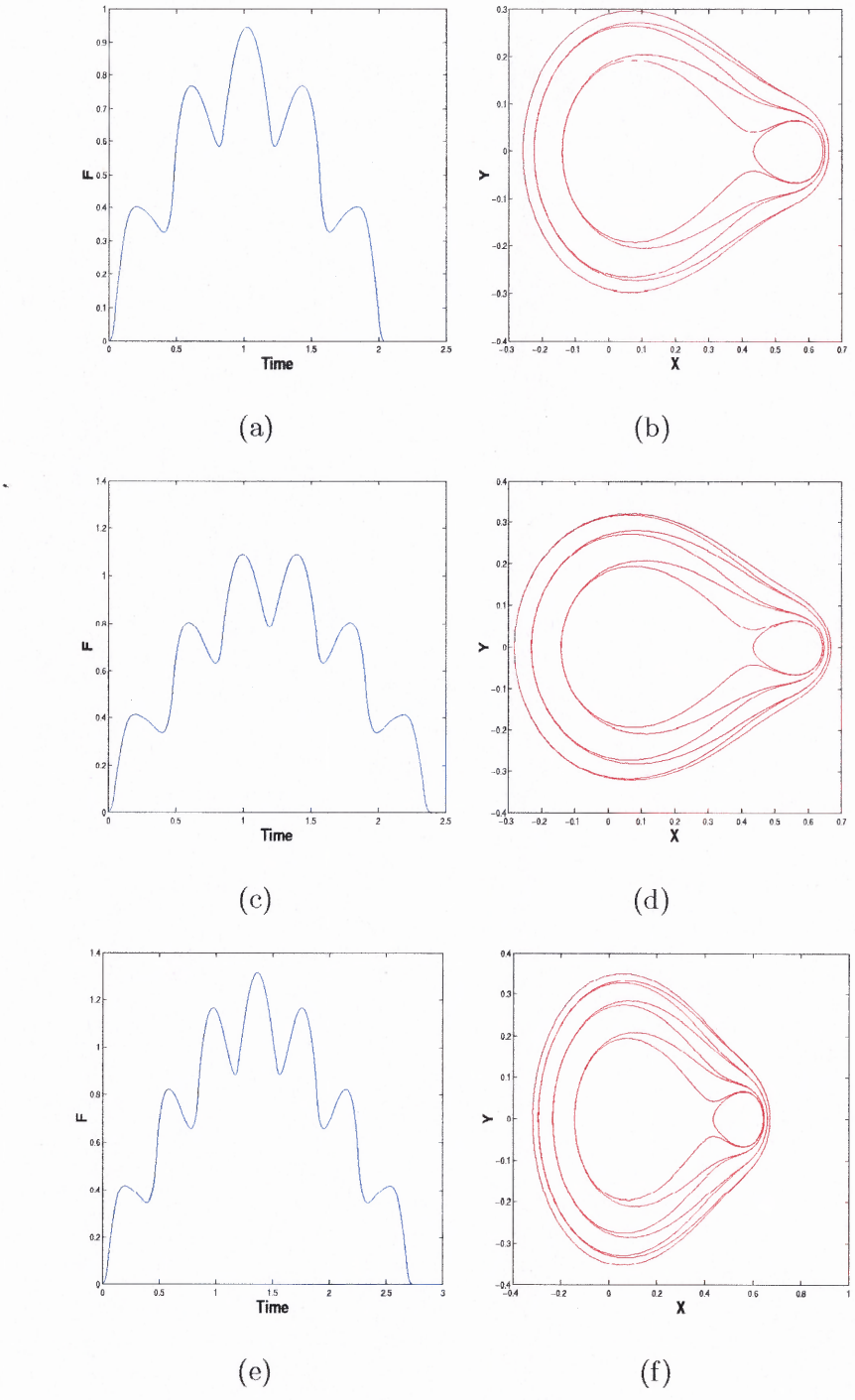

Figure 7.16 (a)-(b) : Resonance 5:1; (c)-(d) : Resonance 6:1; (e)-(f) : Resonance 7:1.

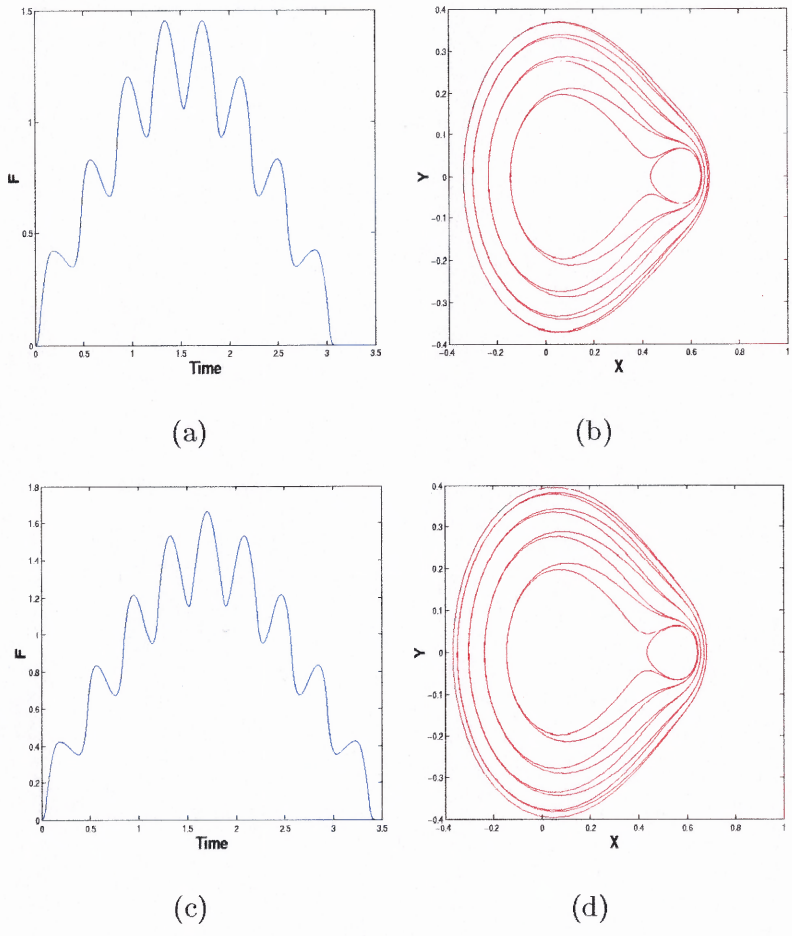

(a) (b)

(c) (d)

Figure 7.17 (a)-(b) : Resonance 8:1; (c)-(d) : Resonance 9:1.

7.3.3 Third family

The values of the parameter μ for the third family of resonances are

μ	Resonance
0.32635261526383	1
0.30961905502768	2
0.30293458498146	3

We display below the plot of the canonical variable F and the trajectory for each value of μ.

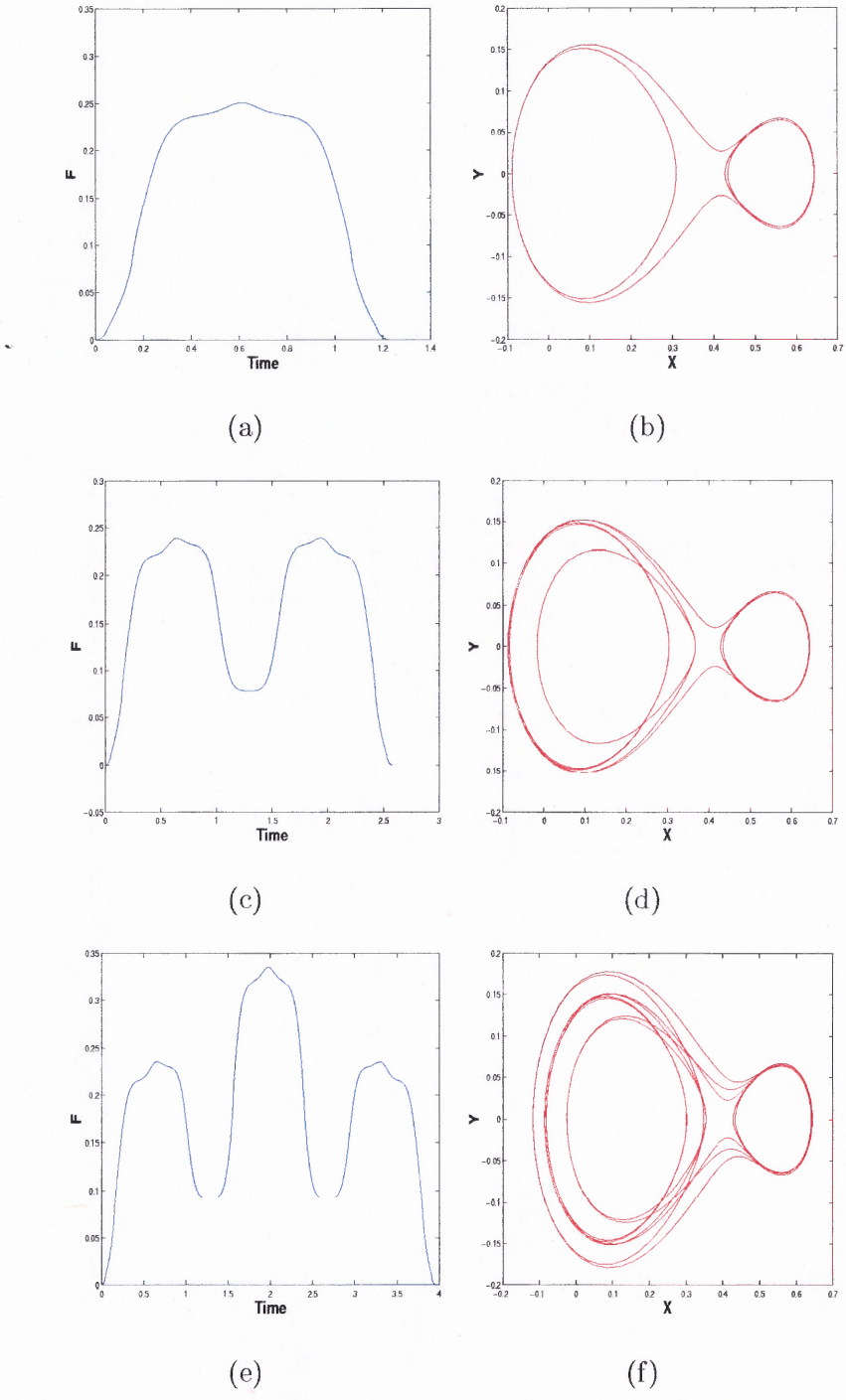

Figure 7.18 (a)-(b) : Resonance 1:1; (c)-(d) : Resonance 2:1; (e)-(f) : Resonance 3:1.

7.3.4 Fourth family

The values of the parameter μ for the fourth family of resonances are

μ	Resonance
0.17242603058919	1
0.26721660376498	2
0.28121392017407	3
0.28817233818785	4
0.29651837373647	8

The plot of the canonical variable F and the trajectory for each value of μ are given below.

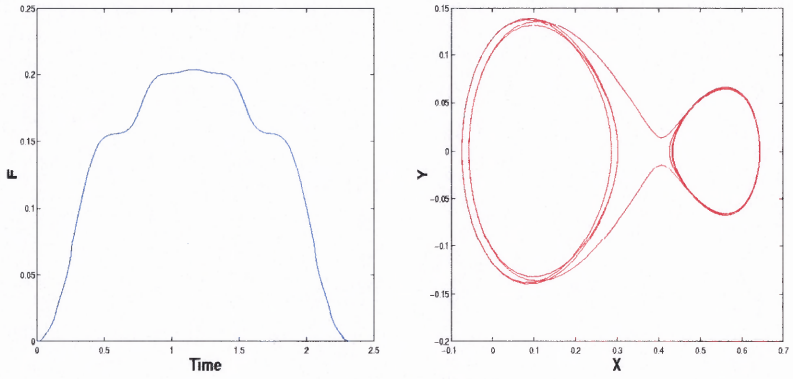

(a) (b)

Figure 7.19 (a)-(b) : Resonance 1:1

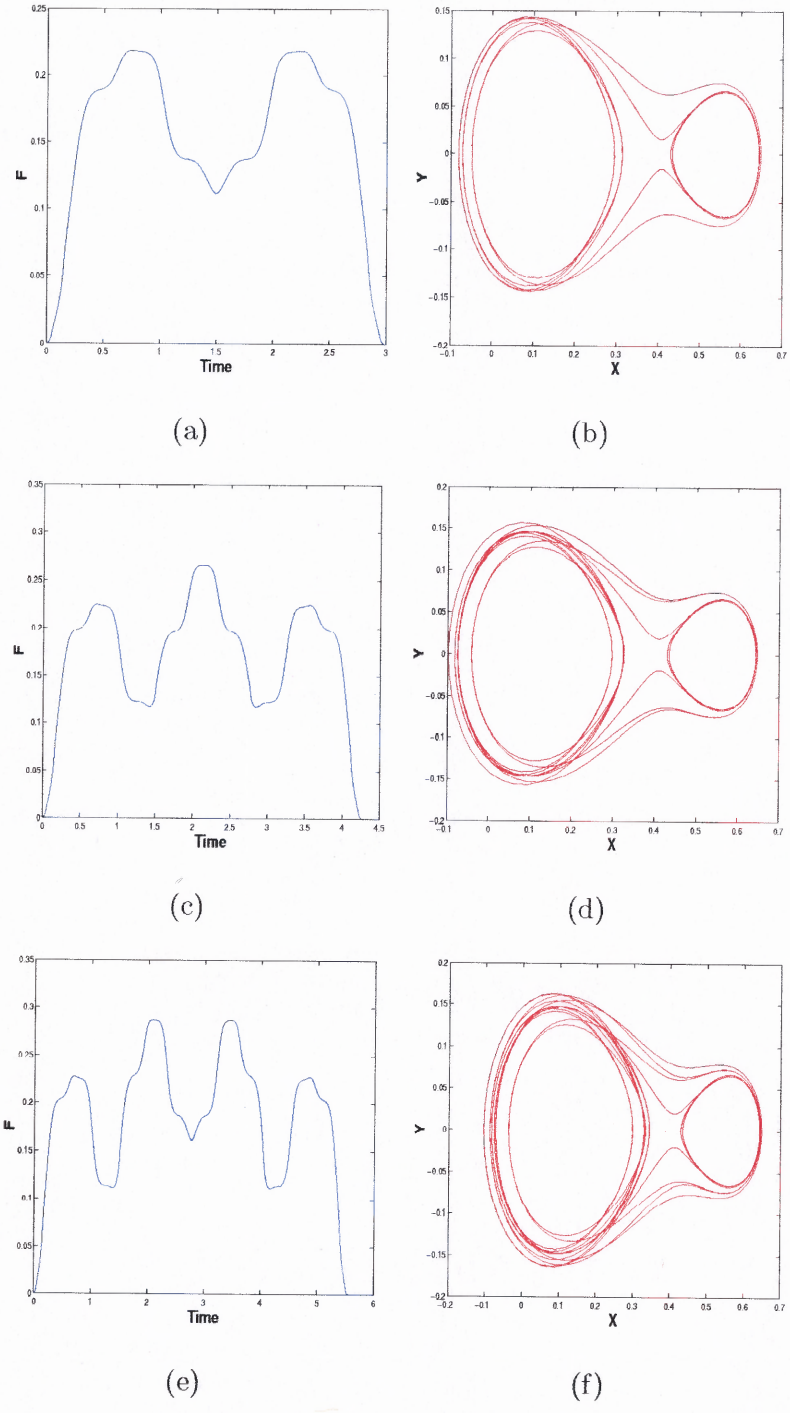

Figure 7.20 (a)-(b) : Resonance 2:1; (c)-(d) : Resonance 3:1; (e)-(f) : Resonance 4:1.

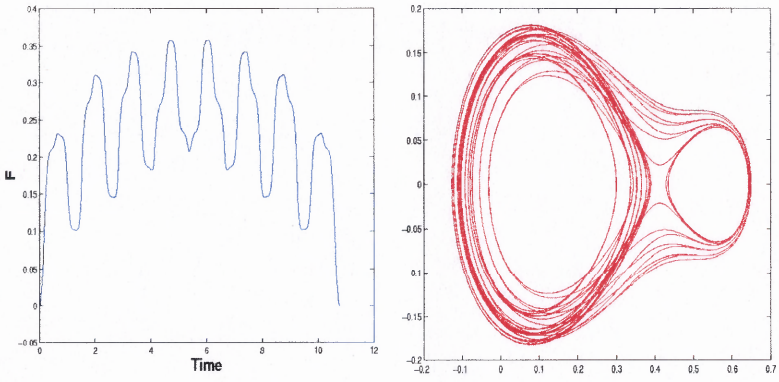

(a) (b)

Figure 7.21 (c)-(d) : Resonance 8:1.

7.3.5 Fifth family

The values of the parameter μ for the fifth family of resonances are

μ	Resonance
0.17242603058919	2
0.26721660376498	3

We give below the plot of the canonical variable F and the trajectory for each value of μ.

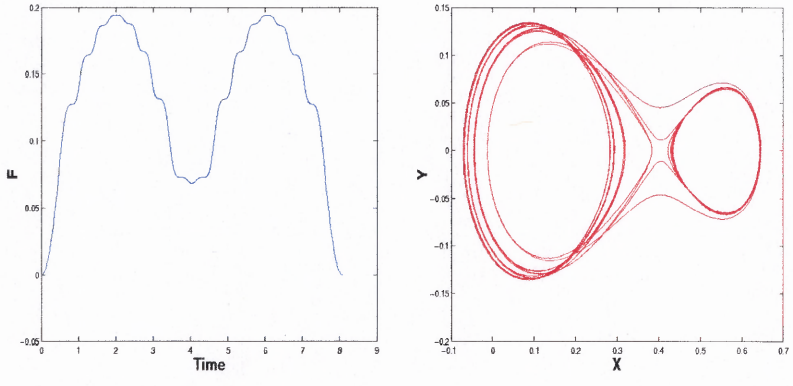

(a) (b)

Figure 7.22 (a)-(b) : Resonance 2:1.

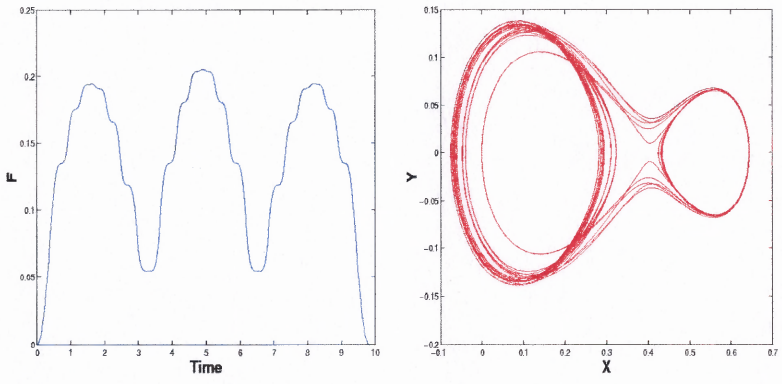

(a) (b)

Figure 7.23 (c)-(d) : Resonance 3:1.

From Figure (7.9), the different families seem to form pairs, first with second family and third with fourth family. For each pair, the parameter μ for each family converges, as the resonance $n:1$ increases to two close limit values. As the resonance $n:1$ increases, we can see from the previous figures that the trajectory, or cycle, becomes more and more complicated and challenging to integrate. Even though we are using a symplectic scheme to integrate the Hamiltonian equations, it is limited by its finite accuracy and running time to compute the trajectories. In a limit of resonance $n:1$ going to infinity, the trajectory will have an infinite number of loops and will be dense in some finite region of the phase space.

CHAPTER 8

CONCLUSION

From a simple protocol consisting of stirring with only one rotating vortex, we were able to obtain good mixing within a circular container. For this, we first derived the Hamiltonian in the frame of reference of the vortex. By studying the Hamiltonian equations and the corresponding phase space dynamics, we produced the bifurcation diagram in a two parameter space, the two dimensionless parameters being the relative position of the vortex with respect to the radius of the container and the ratio of strength to angular velocity of the vortex. Four different streamline patterns of the flow were found, consisting of fixed points (or stagnation points) connected through homoclinic/heteroclinic orbits. These specific trajectories correspond to separatrices dividing the container into two or three independent regions.

The different patterns of the flow obtained numerically were compared to experimental results. While a good qualitative agreement was obtained, some differences could be discerned due to the high viscosity of the fluid used in the experiments. A theoretical model considering viscosity could be derived and studied to identify the effect of viscous diffusion by changing the singularity introduced by the point vortex into a stokeslet [3], [37].

The difference between the case of a single speed vortex and that of a dual speed rotating vortex was shown by means of numerical simulations. In particular, in the latter case, we performed the explicit construction of a Smale's Horseshoe, thus demonstrating the presence of chaos. Furthermore, an example of a stochastic layer, between a chaotic island and a regular one, was obtained numerically with the chaotic island clearly displaying a fractal structure.

Finally, a numerical study of the situation where the angular position of the vortex is perturbed in a sinusoidal fashion in time was carried out by using a symplectic

scheme, allowing us to show the existence of a transverse homoclinic orbit, and therefore the presence of chaotic transport in this situation as well [7]. By considering a perturbation with a particular constraint, we found five families of resonances for which periodic orbits or limit cycles exist, whose periods are equal to multiples of the period of the perturbation.

We would like to close this work by referring to an interesting prior experiment in which the idea of a dual speed was capable of enhancing mixing [10]. The experiment

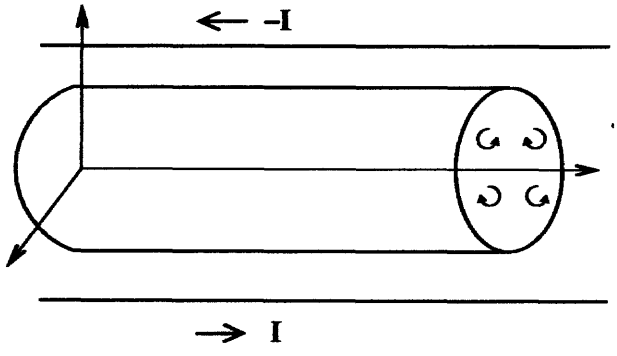

Figure 8.1 Schematic of a quadripolar flow

consisted of a straight channel filled with a conducting fluid. A magnetic field, created by a current going through two wires along the channel located outside of the flow domain, was applied to the flow in order to induce vortices. Two pairs of vortices were induced through the generated Laplace forces and rotated through the rotation of the two wires capable of rotating about the axis of the channel at different (clockwise or counterclockwise) speeds. The difference between a uniform angular speed and a dual speed was highlighted in terms of the mixing index of a dye, but no mathematical explanation was given.

The work displayed in this thesis gave a rational explanation for the mixing enhancement generated by a dual speed vortex. With four vortices, the different patterns of the flow are undoubtedly more complicated but the main ingredients of the observed chaotic advection can be explained by our work, the basic phenomenon being a periodic switch between two sets of transverse streamlines.

APPENDIX A

Canonical Transformation

Let T be a transformation from the old canonical variables $(p,q) \in \mathbb{R}^n \times \mathbb{R}^n$ into the new set of variables $(P,Q) \in \mathbb{R}^n \times \mathbb{R}^n$.

$$T: \quad \mathbb{R}^n \times \mathbb{R}^n \to \mathbb{R}^n \times \mathbb{R}^n \tag{A.1}$$

$$(p,q) \mapsto (P(p,q), Q(p,q)) \tag{A.2}$$

T is said to be a canonical transformation if and only if the Poisson bracket of two functions F and H is preserved, i.e.

$$\{F,H\}_{(p,q)} = \sum_{i=1}^{n} \frac{\partial H}{\partial p_i}\frac{\partial F}{\partial q_i} - \frac{\partial H}{\partial q_i}\frac{\partial F}{\partial p_i} \tag{A.3}$$

$$= \sum_{i=1}^{n} \frac{\partial H}{\partial P_i}\frac{\partial F}{\partial Q_i} - \frac{\partial H}{\partial Q_i}\frac{\partial F}{\partial P_i} = \{F,H\}_{(P,Q)}. \tag{A.4}$$

By expanding the functions P and Q with respect to p and q, we obtain

$$\begin{aligned}
\{F,H\}_{(p,q)} &= \sum_{i=1}^{n} \frac{\partial H}{\partial p_i}\frac{\partial F}{\partial q_i} - \frac{\partial H}{\partial q_i}\frac{\partial F}{\partial p_i} \\
&= \sum_{i=1}^{n}\sum_{k=1}^{n} \left(\frac{\partial H}{\partial P_k}\frac{\partial P_k}{\partial p_i} + \frac{\partial H}{\partial Q_k}\frac{\partial Q_k}{\partial p_i}\right)\left(\frac{\partial F}{\partial P_k}\frac{\partial P_k}{\partial q_i} + \frac{\partial F}{\partial Q_k}\frac{\partial Q_k}{\partial q_i}\right) \\
&\quad - \left(\frac{\partial H}{\partial P_k}\frac{\partial P_k}{\partial q_i} + \frac{\partial H}{\partial Q_k}\frac{\partial Q_k}{\partial q_i}\right)\left(\frac{\partial F}{\partial P_k}\frac{\partial P_k}{\partial p_i} + \frac{\partial F}{\partial Q_k}\frac{\partial Q_k}{\partial p_i}\right) \\
&= \sum_{k=1}^{n} \frac{\partial H}{\partial P_k}\frac{\partial F}{\partial Q_k} - \frac{\partial H}{\partial Q_k}\frac{\partial F}{\partial P_k}\left(\sum_{i=1}^{n} \frac{\partial P_k}{\partial p_i}\frac{\partial Q_k}{\partial q_i} - \frac{\partial P_k}{\partial q_i}\frac{\partial Q_k}{\partial p_i}\right) = \{F,H\}_{(P,Q)}
\end{aligned}$$

It follows that

$$\sum_{i=1}^{n} \frac{\partial P_k}{\partial p_i}\frac{\partial Q_k}{\partial q_i} - \frac{\partial P_k}{\partial q_i}\frac{\partial Q_k}{\partial p_i} = \delta_{ik} \tag{A.5}$$

$$\{P_k, Q_k\} = dP_k \wedge dQ_k$$

in the set of coordinates $(P(p,q), Q(p,q))$, the 2-form $dP \wedge dQ$ can be written as :

$$dP \wedge dQ = \sum_{i=1}^{n} dP_i \wedge dQ_i. \tag{A.6}$$

The equation (A.5) implies that

$$\sum_{k=1}^{n} \frac{\partial P_k}{\partial p_k}\frac{\partial Q_k}{\partial q_k} - \frac{\partial P_k}{\partial q_k}\frac{\partial Q_k}{\partial p_k} = 1 \tag{A.7}$$

or

$$\sum_{k=1}^{n} \frac{\partial p_k}{\partial P_k}\frac{\partial q_k}{\partial Q_k} - \frac{\partial p_k}{\partial Q_k}\frac{\partial q_k}{\partial P_k} = 1 \tag{A.8}$$

We have $\{p_k, q_k\} = dq_k \wedge dq_k$ and $dp \wedge dq = \sum_{i=1}^{n} dp_i \wedge dq_i$, it follows from (A.7) and (A.8)

$$dp \wedge dq = dP \wedge dQ \tag{A.9}$$

APPENDIX B

NORMAL FORM

B.1 Generalities

We give here some generalities about normal forms with double zero eigenvalues [5], [9], [15], [32], [44].

Let us consider $\mathbf{x} \in \mathbb{R}^n$ and a vector field $f(\mathbf{x})$. We assume that the derivative of f with respect to time, $\dot{\mathbf{x}}$, satisfies a system of differential equations $\dot{\mathbf{x}} = f(\mathbf{x})$ with an equilibrium at $\mathbf{x} = 0$, which is non-hyperbolic. We then apply the Center Manifold Theorem and seek information regarding the directions of the flow through higher order terms of f around $\dot{\mathbf{x}} = 0$.

We then look for a change of variable $\xi = h(\mathbf{x})$, with h being a near identity diffeomorphism $h(\mathbf{x}) = \mathbf{x} + h_2(\mathbf{x})$. The new dynamical system for the perturbation takes the form $\dot{\xi} = g(\xi)$.

We now write the function $f(\mathbf{x})$ in the form

$$f(\mathbf{x}) = \sum_{k=1}^{N} f_k(\mathbf{x}) + O(|\mathbf{x}|^{N+1}) \tag{B.1}$$

which is formally a Taylor expansion of f about $\mathbf{x} = \mathbf{0}$ and denote by $\mathbb{H}_k$ the set of homogeneous polynomials of degree k in $\mathbf{x}$. A basis for $\mathbb{H}_k$ is the set of monomials

$$x^m = x_1^{m_1} x_2^{m_2} \dots x_n^{m_n} \tag{B.2}$$

where m is a vector of natural numbers such that $m \in \mathbb{N}^n$ and

$$|m| \equiv \sum_{i=1}^{n} m_i = k \text{ is the degree of the space.} \tag{B.3}$$

We denote by $\mathbb{H}_k^n = \mathbb{H}_k \otimes \dots \otimes \mathbb{H}_k$ the space of vectors of homogeneous polynomials on $\mathbb{R}^n$ and by $\{e_i\}_{i=1}^n$ the unit vectors in $\mathbb{R}^n$.

$$f_k = \sum_{i=1}^{n} \sum_{|m|=k} e_i f_{im} x^m. \tag{B.4}$$

Here, $f_{im} = f_{i,m_1,m_2,\ldots,m_n}$, with $|m| = k$,, denotes the k^{th} partial derivative. Let us write the transformation h as

$$\xi = h(x) = x + h_2(x) + \ldots. \tag{B.5}$$

Since $\dot{\xi} = g(\xi)$, we can write

$$\dot{\xi} = Dh(x)\dot{x} \Rightarrow g(h(x)) = Dh(x)f(x). \tag{B.6}$$

The purpose of the transformation h is to simplify the system of equations that we have to solve. We expect to find $g(x)$ in the form $g(x) = Ax + O(x^3)$, that is a linear set of equations up to the third order.
If $h(x) = x + h_2(x)$, then

$$g(h(x)) = Dh(x)f(x) \tag{B.7}$$

$$Ax + Ah_2(x) = f(x) + Dh_2(x)f(x) \tag{B.8}$$

$$= Ax + f_2(x) + Dh_2(x)Ax + O(x^3). \tag{B.9}$$

By collecting the quadratic terms, we can write

$$Ah_2(x) - Dh_2(x)Ax = f_2(x). \tag{B.10}$$

Homological equation

We now define the homological operator :

$$L_A(h_2) = [h_2, A] = adA(h_2) \equiv Ah_2(x) - Dh_2(x)Ax = f_2(x), \tag{B.11}$$

where [. , .] denotes the Lie bracket, homological operator.

$$\mathbb{H}_k^n = \text{Range}(L_A(\mathbb{H}_k^n)) \oplus \mathbb{G}_k^n \tag{B.12}$$

The solvability condition is

$$0 = \nu_i^T Lh = \nu_i^T f \;\; i = 1, 2, \ldots, k \tag{B.13}$$

where $\{\nu_i\}$ is the left eigenvector with eigenvalue zero. $\mathbb{G}_k^n$ is spanned by $\{\nu_i\}$.

The components of f along these vectors cannot be removed by the diffeomorphism h. We define the projection of f on these left eigenvectors

$$f^R = \sum_{i=1}^{k} \nu_i^T f, \tag{B.14}$$

and will refer to f^R as the resonant part of f.

It follows that

$$\dot{\xi} = g(\xi) = A\xi + f_2^R(\xi) \tag{B.15}$$

where $f_2^R \in \mathbb{G}_2^n$.

We now state the Poincaré-Dulac Theorem.

Theorem 1

$$\frac{d\mathbf{X}}{dt} = \mathbf{F}(\mathbf{X}) \tag{B.16}$$

can be simplified to

$$\frac{d\mathbf{Y}}{dt} = J\mathbf{Y} + \sum_r \mathbf{G}_r(\mathbf{Y}) + O(Y^{N+1}) \tag{B.17}$$

where J is the Jordan form of $A = D_{\mathbf{X}}F(0)$ and $\mathbf{G}_r$ are all the resonant monomials.

B.2 Double Zero Eigenvalues Case (2-jets)

We consider the following Jacobian

$$J = \begin{pmatrix} 0 & 1 \\ 0 & 0 \end{pmatrix} \tag{B.18}$$

and consider the basis for $\mathbb{H}_2$:

$$p_1 = \begin{pmatrix} x^2 \\ 0 \end{pmatrix} \; p_2 = \begin{pmatrix} xy \\ 0 \end{pmatrix} \; p_3 = \begin{pmatrix} y^2 \\ 0 \end{pmatrix} \; p_4 = \begin{pmatrix} 0 \\ x^2 \end{pmatrix} \; p_5 = \begin{pmatrix} 0 \\ xy \end{pmatrix} \; p_6 = \begin{pmatrix} 0 \\ y^2 \end{pmatrix}$$

The action of L_A on this basis is

$$L_A(p_1) = \begin{pmatrix} -2xy \\ 0 \end{pmatrix} \; L_A(p_2) = \begin{pmatrix} -y^2 \\ 0 \end{pmatrix} \; L_A(p_3) = \begin{pmatrix} 0 \\ 0 \end{pmatrix} \tag{B.19}$$

$$L_A(p_4) = \begin{pmatrix} x^2 \\ -2xy \end{pmatrix} \; L_A(p_5) = \begin{pmatrix} xy \\ -y^2 \end{pmatrix} \; L_A(p_6) = \begin{pmatrix} y^2 \\ 0 \end{pmatrix} \tag{B.20}$$

which leads to the matrix representation of L_A in $\mathbb{H}_2$ as follows.

$$L_{A_2} = \begin{pmatrix} 0 & 0 & 0 & 1 & 0 & 0 \\ -2 & 0 & 0 & 0 & 1 & 0 \\ 0 & -1 & 0 & 0 & 0 & 1 \\ 0 & 0 & 0 & 0 & 0 & 0 \\ 0 & 0 & 0 & -2 & 0 & 0 \\ 0 & 0 & 0 & 0 & -1 & 0 \end{pmatrix}, \tag{B.21}$$

with dim Range$(L_{A_2}) = 4$ and dim $\mathbb{G}_2^2 = 2$. There are several choices for the basis of $\mathbb{G}_2^2$.

An example of a left null-eigenvector of L_{A_2} [15] is given by

$$\nu_1 = \begin{pmatrix} 0 \\ 0 \\ 0 \\ 0 \\ 1 \\ 0 \end{pmatrix} \quad \nu_2 = \begin{pmatrix} 0 \\ 0 \\ 0 \\ 1 \\ 0 \\ 0 \end{pmatrix} \tag{B.22}$$

The Reduced System (Normal Form) with Guckenheimer-Holmes' choice [15] is

$$\dot{x} = y \tag{B.23}$$

$$\dot{y} = dx^2 + exy \tag{B.24}$$

where

$$d = \frac{\partial^2 f_2(x,y)}{\partial x^2} \tag{B.25}$$

$$e = 2\frac{\partial^2 f_2(x,y)}{\partial x \partial y} \tag{B.26}$$

In order to know what kind of bifurcation can happen for this degenerate fixed point, we have to "unfold" the system. This can be done by adding suitable terms in the equations. We have to introduce two terms with two new parameters μ_1 and μ_2, thus justifying the name of this bifurcation of codimension-2 or 2-jets.

$$\dot{x} = y \tag{B.27}$$

$$\dot{y} = \mu_1 + \mu_2 y + dx^2 + exy \tag{B.28}$$

APPENDIX C

The Smale Horseshoe

C.1 Introduction

We consider a dynamical system $\dot{\mathbf{x}} = \mathbf{f}(\mathbf{x})$ and suppose that the dynamics has a saddle point with an homoclinic orbit. Under small perturbations, the homoclinic orbit can break, i.e. the stable (W^s) and unstable (W^u) manifolds are not connected in a tangential manner. In the case of a transverse homoclinic orbit, there is a hyperbolic invariant set in the neighborhood of the saddle point (Smale's theorem). The following description of the Smale Horseshoe is generic, that is it is the linearization of the dynamics in the neighborhood of the saddle point.

The first part is a description of the construction of the mapping and its invariant set. The second part describes the mathematical tool we use to derive all the properties of the invariant set.

C.2 Definition

Let f be a map from $\mathcal{D}$ to $\mathbb{R}^2$ where $\mathcal{D}$ is the unit square $[0,1] \times [0,1]$.

$$f : \mathcal{D} \mapsto \mathbb{R}^2$$

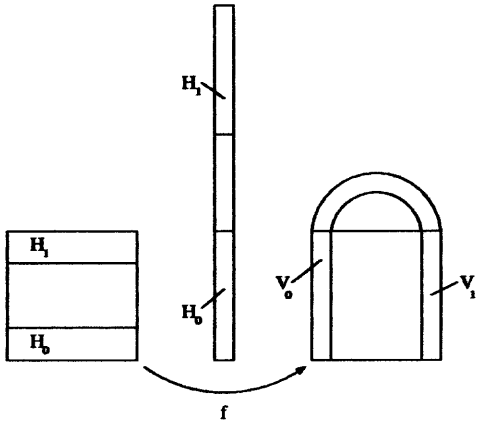

Figure C.1 The action of f on $\mathcal{D}$

f can be decomposed into two steps.

In the first step, f expands the unit square by a factor μ in the y-direction, and contracts by a factor λ in the x-direction, with $0 < \lambda < \frac{1}{2}$ and $\mu > 2$. If the dynamics preserves the volume, which is the case for a Hamiltonian system, then we have $\lambda\mu = 1$. The second step consists in folding the thin rectangle in order to obtain a "horseshoe shape" for $f(\mathcal{D})$.

The intersection $f(\mathcal{D}) \cap \mathcal{D}$ corresponds to two rectangles denoted V_0 and V_1, respectively. We denote by H_0 and H_1 two horizontal rectangles in $\mathcal{D}$ such that $f(H_0) = V_0$ and $f(H_1) = V_1$.

Figure C.2 defines the inverse map f^{-1}

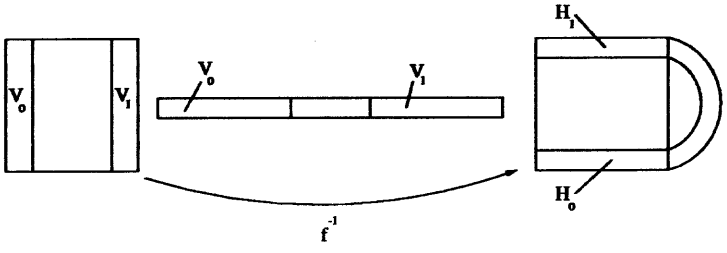

Figure C.2 The action of f^{-1} on $\mathcal{D}$

where f^{-1} contracts by a factor μ^{-1} in the y-direction, expands by a factor λ^{-1} in the x-direction, and folds. We have $H_0 \cup H_1 = \mathcal{D} \cap f^{-1}(\mathcal{D})$.

C.3 Invariant Set : Λ

The invariant set, Λ, of the mapping f is such that $f(\Lambda) = \Lambda$. Since at each iteration by f or f^{-1} we cut, or remove, a part of the horseshoe, we have to consider all the possible iterations by f and f^{-1} of the unit square $\mathcal{D}$.

In other words, the invariant set Λ is given by

$$\Lambda = \bigcap_{n=-\infty}^{+\infty} f^n(\mathcal{D})$$

where Λ is the set of points which remain in $\mathcal{D}$ under all possible iterations of f.

Iterations of f

Figure C.3 displays $f(\mathcal{D})$, $f^2(\mathcal{D})$ and $\cdot\ \mathcal{D} \cap f(\mathcal{D}) \cap f^2(\mathcal{D})$.

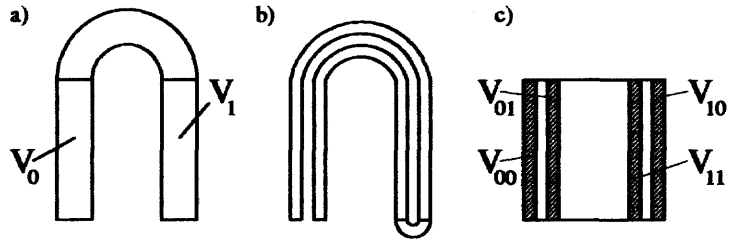

Figure C.3 a) $f(\mathcal{D})$, b) $f^2(\mathcal{D})$, c) $\mathcal{D} \cap f(\mathcal{D}) \cap f^2(\mathcal{D})$

It is clear that $\mathcal{D} \cap f(\mathcal{D}) \cap f^2(\mathcal{D}) \subset \mathcal{D} \cap f(\mathcal{D})$.

Remark :

In order to describe the dynamics, we will introduce the symbolic dynamics. Prior to doing this, we need to label the rectangle in a proper manner with some rules.

After each iteration, we add a new symbol to the left of the index. For example, V_{01} means that the rectangle is in V_0 but that it was previously in V_1. In this manner, one can see right away the history of the rectangle by reading the sequence of symbols representing the index.

The image of a vertical rectangle V_0 (resp. V_1) by f consists of two thinner vertical rectangles $V_{00} \cup V_{10}$ (resp. $V_{01} \cup V_{11}$).

These thinner rectangles are included in previous vertical rectangles, i.e. $V_{ij} \subset V_i$.

We assign to $x \in V_0$ the index 0, and to $x \in V_1$ the index 1 and denote by S the set of indices so that $S = \{0, 1\}$.

Let $V_{s_{-1}s_{-2}}$, with $s_{-1}, s_{-2} \in S$, be a vertical rectangle in $\mathcal{D} \cap f(\mathcal{D}) \cap f^2(\mathcal{D})$; the first index, s_{-1}, indicates that the vertical rectangle is in $V_{s_{-1}}$. The second index, s_{-2}, indicates that the pre-image of $V_{s_{-1}s_{-2}}$ is $V_{s_{-2}}$.

For example, V_{01} is in V_0 and also in $f(V_1)$, that is $V_{01} = V_0 \cap f(V_1) = \{p \in \mathcal{D}, p \in V_0, f^{-1}(p) \in V_1\}$.

We can thus write

$$\begin{aligned}
\mathcal{D} \cap f(\mathcal{D}) \cap f^2(\mathcal{D}) &= V_{00} \cup V_{01} \cup V_{10} \cup V_{11} \\
&= (V_0 \cap f(V_0)) \cup (V_0 \cap f(V_1)) \cup (V_1 \cap f(V_0)) \cup (V_1 \cap f(V_1)) \\
&= \cup_{s_{-i} \in S}^{i=1,2} \left(f(V_{s_{-2}}) \cap V_{s_{-1}} \right) \\
&= \{p \in \mathcal{D}, p \in V_{s_{-1}}, f^{-1}(p) \in V_{s_{-2}}, s_{-i} \in S, i = 1,2\} \\
&\equiv \cup_{s_{-i} \in S}^{i=1,2} V_{s_{-1}s_{-2}}
\end{aligned}$$

Figure C.4 represents the set $\cdot\ \mathcal{D} \cap f(\mathcal{D}) \cap f^2(\mathcal{D}) \cap f^3(\mathcal{D})$.

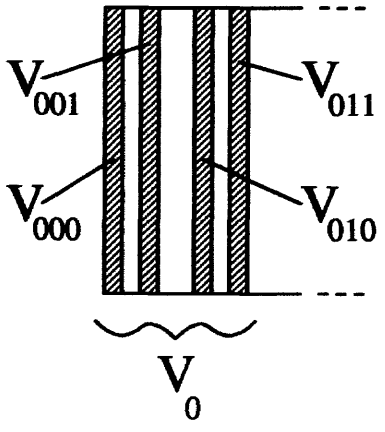

Figure C.4 $V_0 \cap f(\mathcal{D}) \cap f^2(\mathcal{D}) \cap f^3(\mathcal{D})$

This set is composed of 2^3 vertical rectangles, 4 rectangles in V_0 and 4 rectangles in V_1.

For example, V_{010} is in V_0, and also in $f(V_1)$ and $f^2(V_0)$,

that is $V_{010} = V_0 \cap f(V_1) \cap f^2(V_0) = \{p \in \mathcal{D}, p \in V_0, f^{-1}(p) \in V_1, f^{-2}(p) \in V_0\}$.

From this example, one can clearly see that $\bigcap_{n=0}^{n=k} f^n(\mathcal{D})$ corresponds to 2^k vertical rectangles of width λ^k.

$$\bigcap_{n=0}^{n=k} f^n(\mathcal{D}) = \bigcup_{s_{-i}\in S}^{i=1,\ldots,k} V_{s_{-1}\ldots s_{-k}}$$

If $k \to \infty$, we obtain an infinite number of vertical lines,$\lambda^k \to 0$, and each line can be labeled by a unique sequence $\{s_{-1}\ldots s_{-n}\ldots\}$.

$$\bigcap_{n=0}^{n=\infty} f^n(\mathcal{D}) = \bigcup_{s_{-i}\in S}^{i=1,\ldots,k,\ldots} V_{s_{-1}\ldots s_{-k}\ldots} \tag{C.1}$$

$$= \{p \in \mathcal{D}, f^{-(i-1)}(p) \in V_{s_{-i}}, s_{-i} \in S, i = 1,\ldots\} \tag{C.2}$$

$$= \{p \in \mathcal{D}, f^{-i}(p) \in H_{s_{-i}}, i = 1,\ldots\} \text{ since } f(H_{S_i}) = V_{s_i} \tag{C.3}$$

For $n \leq 0$, the same construction holds, substituting $H \leftrightarrow V$ and $f \leftrightarrow f^{-1}$.

We now consider $\mathcal{D} \cap f^{-1}(\mathcal{D}) \cap f^{-2}(\mathcal{D})$, as shown in Figure C.5.

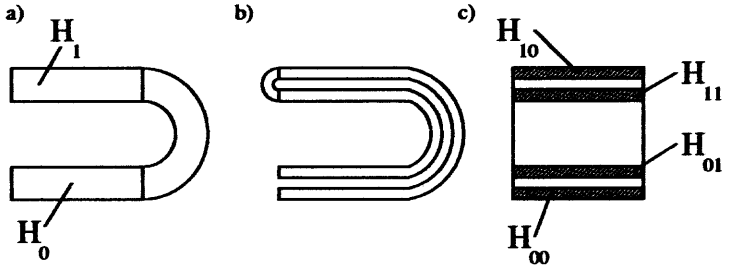

Figure C.5 a) $f^{-1}(\mathcal{D})$, b) $f^{-2}(\mathcal{D})$, c) $\mathcal{D} \cap f^{-1}(\mathcal{D}) \cap f^{-2}(\mathcal{D})$

Remark:

The image of a horizontal rectangle by f^{-1} is the union of two thinner horizontal rectangles.

$$\begin{aligned}\mathcal{D} \cap f^{-1}(\mathcal{D}) \cap f^{-2}(\mathcal{D}) =& H_{00} \cup H_{01} \cup H_{10} \cup H_{11} \\ =& \Big(H_0 \cap f^{-1}(H_0)\Big) \cup \Big(H_0 \cap f^{-1}(H_1)\Big) \cup \\ & \Big(H_1 \cap f^{-1}(H_0)\Big) \cup \Big(H_1 \cap f^{-1}(H_1)\Big) \\ =& \bigcup_{s_{-i} \in S}^{i=1,2} \Big(f^{-1}(H_{s_1}) \cap H_{s_0}\Big) \\ =& \{p \in \mathcal{D}, p \in H_{s_0}, f(p) \in H_{s_1}, s_i \in S, i = 1,2\} \\ \equiv& \bigcup_{s_{-i} \in S}^{i=1,2} H_{s_0 s_1}\end{aligned}$$

Like in the case of the vertical rectangles, $\bigcap_{n=-k}^{n=0} f^n(\mathcal{D})$ is composed of 2^k horizontal rectangles with width equal to μ^{-k}.

$$\bigcap_{n=-k}^{n=0} f^n(\mathcal{D}) = \bigcup_{s_{-i} \in S}^{i=1,\ldots,k-1} H_{s_0 \ldots s_{k-1}}$$

If $k \to \infty$, we obtain an infinite number of horizontal lines, $\mu^{-k} \to 0$, and each line can be labeled by a unique sequence $\{s_0 \ldots s_n \ldots\}$.

$$\bigcap_{n=-\infty}^{n=0} f^n(\mathcal{D}) = \bigcup_{s_i \in S}^{i=1,\ldots,k,\ldots} H_{s_0 \ldots s_k \ldots} \tag{C.4}$$

$$= \{p \in \mathcal{D}, f^i(p) \in H_{s_i}, s_i \in S, i = 0, \ldots\} \tag{C.5}$$

It follows that

$$\Lambda = \left(\bigcap_{n=-\infty}^{0} f^n(\mathcal{D})\right) \bigcap \left(\bigcap_{n=0}^{\infty} f^n(\mathcal{D})\right) \tag{C.6}$$

$$= \{p \in \mathcal{D}, f^i(p) \in H_{s_i}, i = 0, \pm 1, \pm 2, \ldots\} \tag{C.7}$$

Each vertical line intersects each horizontal line at a unique point, so Λ is an infinite set of points. More precisely, it is a Cantor set, closed, compact and perfect. Let $p \in \Lambda$, $p = V_{s_{-1}\ldots s_{-k}\ldots} \cap H_{s_0\ldots s_k\ldots}$. We label the point p by a bi-infinite sequence of 0's and 1's:

$$s = \{\ldots s_{-k} \ldots s_{-1}.s_0 s_1 \ldots s_k \ldots\}$$

Let Φ be a map defined from the set of points $p \in \Lambda$ to bi-infinite sequences in $S^{\mathbf{Z}}$:

$$\Phi : \; p \mapsto \{\ldots s_{-k} \ldots s_{-1}.s_0 s_1 \ldots s_k \ldots\}.$$

From the above construction, the map Φ is one-to-one from Λ to $S^{\mathbf{Z}}$ (see also a proof in Section C.5.2).

C.4 Symbolic Dynamics

C.4.1 Generalities

Let $S = \{0, 1\}$ be the set of symbols, called also the alphabet, and Σ the collection of all bi-infinite sequences of elements of S, $\Sigma = S^{\mathbf{Z}}$.

$$s \in \Sigma \; : \; s = \{\ldots s_{-n} \ldots s_{-1}.s_0 s_1 \ldots s_n \ldots\}$$

Notice that we marked the sequence with a "." on the left of s_0 which means that the first symbol on its right corresponds to the zero coordinate of the sequence.

We define the distance between two elements of Σ, d(s,s') by

$$d(s, s') = \sum_{i=-\infty}^{+\infty} \frac{\delta_i}{2^{|i|}} \text{ where } \delta_i = \begin{cases} 0 & if \; s_i = s'_i \\ 1 & if \; s_i \neq s'_i \end{cases}$$

The shift map σ from Σ into itself is defined by

$$(\sigma(s))_i = s_{i+1} \tag{C.8}$$

for an element s in Σ, that is the map σ shifts each element of the sequence by one place to the left, as indicated by the changed location of the ".".

$$s = \{\ldots s_{-n} \ldots s_{-1}.s_0 s_1 \ldots s_n \ldots\} \rightarrow \sigma(s) = \{\ldots s_{-n} \ldots s_{-1} s_0.s_1 \ldots s_n \ldots\}$$

Lemma:

Let $s, s' \in \Sigma$ and $\epsilon > 0$, if $d(s, s') < \epsilon$, $\exists N = N(\epsilon)$ such that $s_i = s'_i$ for $|i| \leq N$. s and s' agree on a 2N+1 central block.

C.4.2 Properties of the shift map σ

Fixed Points We denote by $\{\overline{s_{i_1} \ldots s_{i_n}}\}$ a sequence having a periodically repeating block $s_{i_1} \ldots s_{i_n}$. For instance, $\{\overline{01}\} = \{\ldots 0101.0101 \ldots\}$.
It is clear that σ has only two fixed points which are the sequences whose elements are all zeros or ones ($\{\overline{0}\}$ or $\{\overline{1}\}$).

Periodic orbits The periodic orbits with a period k correspond to the sequences having a periodically repeating block of length k.
Examples are as follows.

Period 1 : $\{\overline{0.0}\}$, $\{\overline{1.1}\} \sim$ fixed points

Period 2 : $\{\overline{01.01}\}$, $\{\overline{10.10}\}$

Period 3 : $\{\overline{001.001}\}$, $\{\overline{010.010}\}$, $\{\overline{100.100}\}$

$\{\overline{011.011}\}$, $\{\overline{101.101}\}$, $\{\overline{110.110}\}$

$\vdots$

For any fixed k, the number of sequences having a periodically repeating block of length k is finite, i.e σ has 2^k periodic orbits of period k.

It follows that σ has a countable infinity of periodic orbits.

Non periodic orbits We consider a non-periodic infinite sequence $s = \{.s_0 \dots s_n \dots\}$. s being non-periodic, it is equivalent to an irrational number, in the unit interval, expressed in base 2. This irrational number in the closed unit interval constitutes an uncountable set.

Moreover, we can construct an infinite number of bi-infinite sequences s' such that $s'_i = s_i \; \forall i \geq 0$. We thus have a correspondence between an uncountable set of points and non-repeating sequences.

The orbits of these sequences are non-periodic orbits of σ, and there is an uncountable number of such orbits.

A dense orbit We must find an element $s \in \Sigma$, whose orbit is dense in Σ, i.e for any given $s' \in \Sigma$, $\epsilon > 0$, $\exists n \in \mathcal{N}$ such that $d(\sigma(s)^n, s') < \epsilon$.

We consider all possible sequences of 0's and 1's having length 1, 2, 3,...

length 1 : 0 , 1

length 2 : 00 , 01 , 01 , 11

$\vdots$

We now introduce a rule to order the collection of sequences of length k. Let $\tilde{s}, \overline{s}$ be two finite sequences

$$\tilde{s} = \{\tilde{s_1} \dots \tilde{s_k}\} \; ; \; \overline{s} = \{\overline{s_1} \dots \overline{s_{k'}}\}$$

- for $k < k'$, $\tilde{s} < \overline{s}$ for
- $k = k'$, $\tilde{s} < \overline{s}$ if $\tilde{s_i} < \overline{s_i}$ where "i" is the first integer such that $\tilde{s_i} \neq \overline{s_i}$

This rule is equivalent to considering $\tilde{s}$ and $\overline{s}$ integer numbers expressed in base 2, and ordering these integer numbers in increasing order.

If we consider the finite sequence $\tilde{s}$ of length k, we have

$$\tilde{s}_1^k < \tilde{s}_2^k < \ldots < \tilde{s}_{2^k}^k$$

where the superscript k refers to the length of the sequence and the subscript denotes the position of a particular sequence in the collection of sequences of length k.
We now construct a bi-infinite sequence s as follows

$$s^\infty = \{\ldots s_8^3 s_6^3 s_4^3 s_2^3 s_4^2 s_2^2 . s_1^1 s_1^2 s_3^2 s_1^3 s_3^3 s_5^3 s_7^3 \ldots\}$$

where s is built by concatenation of all finite sequences $\tilde{s}_j^k$, $k = 1, 2, \ldots$ and $j = 1, 2, \ldots, 2^k$ taken in the order defined above, alternatively to the right and to the left of the central position. Notice that each finite possible block appears at least once in s^∞.

For any given $s' \in \Sigma$, we suppose an element $s'' \in \Sigma$ in the ϵ-neighborhood of s', i.e $d(s', s'') < \epsilon$. Therefore, $\exists N = N(\epsilon)$ such that $s'_i = s''_i$, $|i| \leq N$.
The finite sequence $\{s'_{-N} \ldots s'_{-1} . s'_0 s'_1 \ldots s'_N\}$, however, is contained somewhere in s.
It follows that $\exists n \in \mathcal{N}$ such that $d(\sigma(s)^n, s') < \epsilon$, that is the orbit of s is dense in Σ.

C.5 f and σ are topologically conjugate

C.5.1 Definition

Let f (resp. g) be a C^r-diffeomorphism of a topological space A (resp. B). f and g are said to be C^k-conjugate ($k \leq r$) if there exists a C^k-diffeomorphism $h : A \to B$ such that $g \circ h = h \circ f$.
If $k = 0$, f and g are said to be topologically conjugate and h is a homeomorphism.

$$\begin{array}{ccc} A & \xrightarrow{f} & A \\ {\scriptstyle h}\downarrow & & \downarrow{\scriptstyle h} \\ B & \xrightarrow{g} & B \end{array}$$

C.5.2 Properties of the map Φ

Theorem 1 *$\Phi : \Lambda \rightarrow \Sigma$ is a homeomorphism*

Proof:

* Φ is one-to-one:

$p, p' \in \Lambda$ if $p \neq p'$, then $\Phi(p) \neq \Phi(p')$. Proof by contradiction:

We suppose $\Phi(p) = \Phi(p') = \{\ldots s_{-n} \ldots s_{-1}.s_0 s_1 \ldots s_n \ldots\}$. By construction, p and p' lie in the intersection of the vertical line $V_{s_{-1}\ldots s_{-n}\ldots}$ and the horizontal line $H_{s_0\ldots s_n\ldots}$. The intersection is a unique point, therefore $p = p'$.

* Φ is onto:

Let $s \in \Sigma$, $s = \{\ldots s_{-n} \ldots s_{-1}.s_0 s_1 \ldots s_n \ldots\}$.

The sequences $\{.s_0 s_1 \ldots s_n \ldots\}$ and $\{\ldots s_{-n} \ldots s_{-1}\}$ correspond respectively to a unique horizontal line and vertical line. These lines intersect in a unique point $p \in \Lambda$. It follows that every bi-infinite sequence corresponds to a point in Λ, and that this point is unique.

* Φ is continuous, that is $\forall p \in \Lambda, \forall \epsilon > 0, \exists \delta > 0; |p - p'| < \delta \Rightarrow |\Phi(p) - \Phi(p')| < \epsilon$

Let ϵ be given, and $p, p' \in \Lambda$:

$$\Phi(p) = \{\ldots s_{-n} \ldots s_{-1}.s_0 s_1 \ldots s_n \ldots\}.$$
$$\Phi(p') = \{\ldots s'_{-n} \ldots s'_{-1}.s'_0 s'_1 \ldots s'_n \ldots\}.$$

Therefore $d(\Phi(s), \Phi(s')) < \epsilon$ so $\exists N = N(\epsilon) \in \mathcal{N}$ with $s_i = s'_i$, $i = 0; \pm 1; \pm 2; \ldots; \pm N$. Consequently, p, p' are in a rectangle defined by $H_{s_0\ldots s_N} \cap V_{s_{-1}\ldots s_{-N}}$ and $|p - p'| < (\lambda^N + \mu^{-N}) = \delta$, with $|p - p'|$ being the euclidian distance in $\mathcal{R}^2$.

We have therefore a one-to-one, onto, and continuous map between compact sets in Hausdorff spaces, and therefore the inverse is continuous.

We thus deduce that Φ is a homeomorphism.

C.6 Conclusion

We have a relation between f and g which are topologically conjugate. The shift map has the following properties.

- There is a countable infinite number of periodic orbits of arbitrarily high period.
- There is an uncountable infinite number of non-periodic orbits.
- There is a dense orbit.

It is then possible to transport these properties to f.

The Smale horseshoe, f, has :

- A countable infinite number of periodic orbits of arbitrarily high period. These periodic orbits are all of saddle type.
- An uncountable infinite number of non-periodic orbits.
- A dense orbit.

Furthermore, the $s_{k^{th}}$ element of the sequence $\Phi(p)$, with $p \in \Lambda$, corresponds to $f^k(p)$. It follows that the shift map σ from Σ into itself is "equivalent" to the horseshoe map f.

$$\begin{array}{ccc} \Lambda & \xrightarrow{f} & \Lambda \\ {\scriptstyle\Phi}\downarrow & & \downarrow{\scriptstyle\Phi} \\ \Sigma & \xrightarrow{\sigma} & \Sigma \end{array}$$

REFERENCES

[1] AREF, H. Stirring by chaotic advection. *Journal of Fluid Mechanics 143* (1984), 1–21.

[2] AREF, H. The development of chaotic advection. *Physics of fluids 14, No 4* (2002).

[3] AREF, H., AND BALACHANDAR, S. Chaotic advection in stokes flow. *Physics of Fluids 29, No 11* (1986), 3515–3521.

[4] ARNOLD, V. *Mathematical methods of classical mechanics*, graduate texts in mathematics 60 ed. Springer Verlag, 1980.

[5] ARNOLD, V., GUSEIN-ZADE, S., AND VARCHENKO, A. *Singularities of Differentiable Maps Volume I*, vol. 82. Monographs in Mathematics, 1985.

[6] BATCHELOR, G. *An Introduction to Fluid Dynamics.* Cambridge University Press, 1967.

[7] BEIGIE, D., LEONARD, A., AND WIGGINS, S. Chaotic transport in the homoclinic and heteroclinic tangle regions of quasiperiodically forced two-dimensional dynamical systems. *Nonlinearity 4* (1991), 775–819.

[8] BOFFETTA, G., CELANI, A., AND FRANZESE, P. Trapping of passive tracers in a point vortex. *Journal of Physics 29* (1996), 3749–3759.

[9] BOGDANOV, R. Bifurcations of a limit cycle for a family of vector fields on the plane. *Selecta Math. Soviet 1* (1981), 373–388.

[10] BRANCHER, J., LEPRÉVOST, J., AND ANGILELLA, J. Mélange laminaire chaotique dans un ecoulement quadripolaire en deux et trois dimensions. *Congrès Français de Mécanique,Nancy* (5-7 September 2001).

[11] BUTCHER, J. *The Numerical Analysis of Ordinary Differential Equations.* John Wiley and Sons, 1987.

[12] CHAIKEN, J., CHEVRAY, R., TABOR, M., AND TAN, Q. Experimental study of lagrangian turbulence in a stokes flow. *Proc. Royal Soc. of London A408* (1986), 165–174.

[13] ECKART, C. An analysis of the stirring and mixing processes in incompressible fluids. *J. Mar. Res. 7* (1948), 265.

[14] F. BOYLAND, H. AREF, M. S. Topological fluid mechanics of stirring. *Journal of Fluid Mechanics 403* (2000), 277–304.

[15] GUCKENHEIMER, J., AND HOLMES, P. *Nonlinear Oscillations, Dynamical Systems, and Bifurcations of Vector Fields*, second edition ed. Springer Verlag, New York, 1991.

[16] HAIM H. BAU, J. ZHONG, M. Y. A minute magneto hydro dynamic (mhd) mixer. *Sensors and Actuators B 79* (2001), 207–215.

[17] HORNER, M., METCALFE, G., WIGGINS, S., AND OTTINO, J. Transport enhancement mechanisms in open cavities. *Journal of Fluid Mechanics 452* (2002), 199–229.

[18] HORNER, M., MILLER, W., OTTINO, J., AND PAPOUTSAKIS, E. Transport in a grooved perfusion flat-bed bioreactor for cell therapy applications. *Biotechnol. Prog. 14* (1998), 689–698.

[19] IMAGEJ 1.29. http://rsb.info.nih.gov/ij/, (2002).

[20] JONES, S., AND AREF, H. Chaotic advection in pulsed source-sink systems. *Physics of fluids 31, No 3* (1988), 469–485.

[21] KHAKHAR, D., RISING, H., AND OTTINO, J. An analysis of chaotic mixing in two model systems. *Journal of fluid mechanics 172* (1986), 419–451.

[22] KUZNETSOV, L., AND ZASLAVSKY, G. Regular and chaotic advection in the flow field of a three-vortex system. *Physical Review E 58* (1998), 7330.

[23] LAMB, H. *Hydrodynamics.* Dover, 1932.

[24] LASAGNI, F. Canonical Runge-Kutta methods. *ZAMP 39* (1988).

[25] LEONG, C. *Chaotic mixing of viscous fluids in time-periodic cavity flows.* Phd thesis, Dept. of Chem. Eng. University of Massachusetts, 1990.

[26] LICHTENBERG, A., AND LIEBERMAN, M. *Regular and chaotic dynamics*, second edition, applied mathematical sciences 38 ed. Springer Verlag, 1992.

[27] LIU, R., STREMLER, M., KENDRA, K., OLSEN, M., SANTIAGO, J., ADRIAN, R., AREF, H., AND BEEBE, D. Passive mixing in a three-dimensional serpentine microchannel. *Journal of microelectromechanical systems 9, No 2* (2000), 190–196.

[28] MATHEMATICA 5. *Wolfram Research.* http://www.wolfram.com, 2003.

[29] MATLAB 6.3. *Mathworks.* http://www.mathworks.com, 2003.

[30] MEZIĆ, I. Chaotic advection in bounded navier-stokes flows. *Journal of Fluid Mechanics 431* (2001).

[31] MEZIĆ, I., AND SOTIROPOULOS, F. Ergodic theory and experimental visualization of invariant sets in chaotically advected flows. *physics of fluids 14*, 7 (2002).

[32] MURDOCK, J. *Normal Forms and Unfoldings for Local Dynamical Systems.* Springer Monographs in Mathematics, 2002.

[33] OEVEL, W., AND SOFRONIOU, M. Symplectic Runge-Kutta schemes II : Classification of symmetric methods.

[34] OEVEL, W., AND SOFRONIOU, M. Symplectic Runge-Kutta schemes III : Canonical elementary differentials.

[35] OEVEL, W., AND SOFRONIOU, M. Symplectic Runge-Kutta schemes I : Order conditions. *SIAM Journal of Numerical Analysis 34(5)* (1997).

[36] OTTINO, J. *The Kinematics of Mixing: Chaos and Transport.* Cambridge univ. Press, Cambridge, 1990.

[37] OTTO, S., YANNACOPOULOS, A., AND BLAKE, J. Transport and mixing in Stokes flow: the effect of chaotic dynamics on the blinking stokeslet. *Journal of Fluid Mechanics 430* (2001).

[38] PERKO, L. *Differential equations and dynamical systems*, third edition ed. Springer, 2000.

[39] PROJECT. *Synode.* http://www.math.ntnu.no/num/synode/.

[40] SANZ-SERNA, J. Runge-Kutta schemes for Hamiltonian systems. *BIT 28* (1988).

[41] STROOCK, A., DERTINGER, S., AJDARI, A., MEZIĆ, I., STONE, H., AND WHITESIDES, G. Chaotic mixer for microchannels. *Science 295* (2002), 647–650.

[42] STRUCKMEIER, J., AND RIEDEL, C. Canonical transformations and exact invariants for time-dependent Hamiltonian systems. *Annals of Physics (Leipzig) 11* (2002), 15–38.

[43] SUSUKI, H., AND HO, C.-M. A magnetic force driven chaotic micro-mixer. *Proc. 15th Int. Conf. on MEMS* (2002).

[44] TAKENS, F. Normal forms for certain singularities of vector fields. *Annales de l'institut Fourier 23* (1972), 163–195.

[45] WATSON, G. *A treatise on the theory of Bessel functions.* Cambridge Univeristy Press, 1944.

[46] WELANDER, P. Studies of the general development of motion in a two dimensional ideal fluid. *Tellus 7* (1955), 141.

[47] WIGGINS, S. *Introduction to Applied Nonlinear Dynamical Systems and Chaos.* Springer-Verlag, 1990.

[48] WIGGINS, S. *Chaotic Transport in Dynamical Systems.* Springer-Verlag, 1992.

[49] WILSON, H., AND SINGH, D. Runge-kutta scheme 7th order with local interpolation. *ftp.hacettepe.edu.tr/pub/mirrors/MathLab/contrib/v4/diffeq/ode78.m.*

[50] ZUMBRUNNEN, D., AND INAMDAR, S. Novel sub-micron highly multi-layered polymer films formed by continuous flow chaotic mixing. *Chemical Engineering Science 56* (2001), 3893–3897.